Development of Kinetic-Theory-Based High-Resolution Schemes for the Euler and Navier-Stokes Equations of Gas Dynamics

A
Thesis Submitted
in Partial Fulfillment of the Requirements
for the Degree of
DOCTOR OF PHILOSOPHY
By

RAUSHAN KUMAR
Roll No : 11610301

Department of Mechanical Engineering
Indian Institute of Technology Guwahati
Guwahati - 781039, Assam, India
December, 2019

Declaration

This is to certify that the thesis entitled "**Development of Kinetic-Theory-Based High-Resolution Schemes for the Euler and Navier-Stokes Equations of Gas Dynamics**", submitted by me to the *Indian Institute of Technology Guwahati*, for the award of the degree of Doctor of Philosophy, is a bonafide work carried out by me under the supervision of Prof. Anoop K. Dass. The content of this thesis, in full or in parts, have not been submitted to any other University or Institute for the award of any degree or diploma. I also wish to state that to the best of my knowledge and understanding nothing in this report amounts to plagiarism.

Signed: _____

Raushan Kumar
Mechanical Engineering,
Indian Institute of Technology Guwahati,
Guwahati-781039, Assam, India.

Date: _____

To my Guruji and Govind

Certificate

This is to certify that the thesis entitled "**Development of Kinetic-Theory-Based High-Resolution Schemes for the Euler and Navier-Stokes Equations of Gas Dynamics**", submitted by Raushan Kumar (11610301), a research scholar in the *Mechanical Engineering* department, *Indian Institute of Technology Guwahati*, for the award of the degree of Doctor of Philosophy, is a record of an original research work carried out by him under my supervision. The thesis has fulfilled all requirements as per the regulations of the institute and in my opinion has reached the standard needed for submission. The results embodied in this thesis have not been submitted to any other University or Institute for the award of any degree or diploma.

Signed: _____

Supervisor: Prof. Anoop K. Dass
Mechanical Engineering,
Indian Institute of Technology Guwahati,
Guwahati-781039, Assam, India.

Date: _____

Acknowledgements

The Ocean of Bliss which manifests the world was alone and divided itself into two, Shyama and Shyam, I cry for their one glimpse. It is a great wonder that some beings of this ocean, which probably are infinitely many in number, suffer. This seemingly continuous suffering makes them search for the bliss continuously at all instants, and being an integral part of the ocean, this hankering is an inherent nature. It seems that I am one of these beings and there are many others all around. The PHD work has been a failed attempt in the search of the ocean while swimming inside and living in it all the time.

In this particular course of swim, I met others like me involved in the same search. The swim was made easier by my PHD thesis supervisor Prof. Anoop K Dass. I cannot thank enough for the helpful discussions and guidance without which the work was looking like a never ending project. The fascinating area of kinetic theory based schemes was introduced to me by him. This research area was entirely new to me and it has reshaped and broadened my perspective of looking at physical phenomena in many alternative different ways. I would like to thank Dr. Ganesh Natarajan for his immensely valuable suggestions and kind help. The fluid mechanics and CFD classes of Dr. Arnab De were a great value addition to my understanding of the subjects, I shall always be obliged. Prof. Muthukumar and Prof. Senthilvelan helped me financially by giving me a departmental project at the time when I was going through a distressful time just before the starting of the PHD work, I will always be indebted for the support. I thank all the other faculty members who helped me in some way or the other. My close fellow swimmers of the ocean, my friends, Vijay Mishra, Jai Manik, Dhrubajyoti, Kalpajyoti, Subhra, Peter sir, Paragmoni sir, Biplob, Sandip, Gyan, Jitendra, Mukesh, Mantulal, and all the others whose names I have not mentioned made my long stay at IIT Guwahati pleasing.

Thanking is meaningless when it comes to the ocean and the family, particularly, my parents and sisters. Their patience and support gave me the energy to walk through this long journey. Finally, glories to Ladali-Lal.

Raushan Kumar

Abstract

This thesis proposes new kinetic-theory-based high-resolution schemes for the Euler and Navier-Stokes equations of gas dynamics. The schemes exploit the well-known connection that the Euler and Navier-Stokes equations are suitable moments of the Boltzmann equation of kinetic theory. In order to develop a high-resolution scheme for the Euler equations the collisionless Boltzmann equation is discretized using Sweby's flux limited method and the moment of this Boltzmann level formulation gives the Euler level scheme. It is demonstrated how conventional limiters and an extremum-preserving limiter can be adapted for use in the scheme to achieve a desired effect. A one-dimensional (1D) scheme is formulated first and an extension to 2D on Cartesian meshes is carried out next through dimensional splitting. Accuracy analysis suggests that the scheme achieves between first and second order accuracy as is expected for any second order flux-limited method. The scheme is carefully validated by computing various test cases ranging from moderate to high complexity. As far as the computation of viscous flow is concerned, one common strategy followed by researchers is that the scheme for the Euler equations is still used for the inviscid fluxes whereas "central differencing" is used for the viscous fluxes. When the present flux-limited scheme is used in this fashion to solve the Navier-Stokes equations it is observed that the time-step has to be prohibitively small for obtaining accurate results. In order to overcome this problem, instead of the collisionless Boltzmann equation, collision term is approximated by Bhatnagar-Gross-Krook (BGK) collision model in the full Boltzmann equation. The Chapman-Enskog expansion of the velocity distribution function is used to split the viscous fluxes. These new split fluxes result in a modification of the expression of the conservative numerical flux of the scheme for the Euler equations to become a Navier-Stokes solver. Various viscous flows are computed to validate the scheme. In addition, to obtain better time-wise efficiency a new flux-corrected methodology based kinetic scheme for the Euler equations is developed. The scheme does not require any flux splitting or calculation of error functions like that in the flux-limited kinetic scheme, and hence reduces computational cost significantly. A somewhat approximate yet effective method of implementing the schemes on triangular unstructured grids is also developed. The strategy is validated through some 2D computations of reasonable accuracy. The results presented in the thesis are checked for grid independence.

Contents

List of Figures

List of Tables

Nomenclature

Symbols

$\mathbf{FX}$	x-direction flux vector
$\mathbf{FX}^{\pm}$, $\mathbf{FY}^{\pm}$	Split fluxes in FLKS
$\mathbf{FX}_v$	x-direction viscous flux vector
$\mathbf{FY}$	y-direction flux vector
$\mathbf{FY}_v$	y-direction viscous flux vector
$\mathbf{GX}$, $\mathbf{GY}$	Part of numerical fluxes appearing in KFC scheme
$\mathbf{GX}^{\pm}$, $\mathbf{GY}^{\pm}$	Split fluxes in FLKS
$\mathbf{U}$	Conservative variable vector
Ec	Eckert number
Pr	Prandtl number
R	Gas constant per unit mass
a	Sonic speed, wave speed in linear advection equation
C_p	Specific heat at constant pressure
e	Total energy per unit mass
F	Maxwellian distribution function
f	Velocity distribution function
I	Internal energy variable corresponding to non-translational degrees of freedom
I_0	Internal energy due to non-translational degrees of freedom
k	Thermal conductivity coefficient
M	Mach number
p	Pressure
T	Temperature
u	Fluid velocity component in x-direction, conserved variable in linear advection equation

v	Fluid velocity component in y-direction
v_1	Molecular velocity component in x-direction
v_2	Molecular velocity component in y-direction
$\boldsymbol{\Psi}$	Moment function vector
γ	Specific heat ratio
μ	Coefficient of viscosity in N-S equations, coefficient of artificial viscosity
Φ, ϕ	Limiter functions
ρ	Fluid density
$\sigma_{xx}, \sigma_{xy}, \sigma_{yx}, \sigma_{yy}$	Viscous stress tensor components
τ	Particle collision time

Abbreviations

ADER	Arbitrary derivative
AUSM	Advection upstream splitting method
BGK	Bhatnagar-Gross-Krook
CFL	CFL number
CIR	Courant-Isaacson-Rees
EFM	Equilibrium flux method
ENO	Essentially non-oscillatory
FLKS	Flux limited kinetic solver
FLKSext-pre	FLKS scheme with extremum-preserving limiter
FLKSmm	FLKS scheme with minmod limiter
FLKSsb	FLKS scheme with superbee limiter
FLKSvl	FLKS scheme with Van Leer limiter
FLKSvl2	FLKS scheme with second type Van Leer limiter
HRKFVS	High resolution kinetic flux vector splitting
KFC	Kinetic flux correction
KFVS	Kinetic flux-vector splitting
KFVS-NS	Kinetic flux-vector splitting for the Navier-Stokes equations
KNM	Kinetic numerical method
m-KFVS	Modified kinetic flux vector splitting

MUSCL	Monotonic upstream-centered scheme for conservation laws
PPM	Piecewise parabolic method
PVU	Peculiar velocity upwind
TVB	Total variation bounded
TVD	Total variation diminishing

Chapter 1

Introduction

Gas dynamics deals with the study of compressible flow of gases. In order to analyze such a flow, laws of nature stated in terms of conservation of some physical quantities, like mass, momentum, energy, etc., popularly known as "conservation laws" are used. The flow can be analyzed by looking at it from two points of view, namely, microscopic and macroscopic. The microscopic point of view looks at the gas flow situation as a flow or stream of molecules, and the conservation of the number of these molecules serves as the "conservation law" at this level. The Boltzmann equation of kinetic theory is a result of this particle conservation approach at a molecular level. In a continuum regime, the same gas flow can be described in terms of the macroscopic concepts, namely, pressure, temperature, etc. These macroscopic quantities at a particular location and time can be related to the molecular mass, momentum, and energy distributions at a microscopic level. To establish such a relationship is one of the major objectives of kinetic theory of gases.

At a macroscopic level the conservation laws give the Euler equations and the Navier-Stokes equations which govern inviscid and viscous flow cases, respectively. These equations are sets of partial differential equations which provide a mathematical relationship among the quantities of interest, such as, pressure, density, temperature, etc. There are no general solutions to these equations and this is where the subject of "computational gas dynamics" steps in, which is a part of the larger field of "computational fluid dynamics (CFD)". At a microscopic level, the particle conservation gives the Boltzmann equation which is a single integro-differential equation. This

equation gives time evolution of particle distribution function. The major task of kinetic theory is to figure out an analytic expression of this distribution function. The complexity involved in this task motivates for a numerical solution to this problem. In CFD there are approaches to go for a numerical solution to the Boltzmann equation, and this thesis is concerned with one such approach, which indirectly but finally results in numerical schemes for the Euler and Navier-Stokes equations.

1.1 History and Literature Review

Construction of efficient discretization schemes for the Euler and Navier-Stokes equations of gas dynamics is an important activity in CFD that has received considerable attention in the past four decades. Numerical conservation, upwinding, positivity, entropy condition satisfaction, etc., are some of the well established properties that a numerical scheme needs to satisfy. Upwinding property has become the main guiding principle for simulating hyperbolic nonlinear equations of gas dynamics. Harten et. al. [1] mention that upwinding principle in the computational algorithms for Euler equations is implemented using generally two techniques, namely, Riemann solvers and Boltzmann equation solvers, and all the flux vector splitting techniques can be viewed as some kind of collisionless Boltzmann type equation solvers. The Euler and Navier-Stokes equations of gas dynamics can be obtained by taking moments of the Boltzmann equation of kinetic theory of gases with proper velocity distribution functions [2, 3]. The computational schemes in gas dynamics based on Boltzmann equation can broadly be divided into two categories—schemes using collisionless Boltzmann equation and schemes using Boltzmann equation with collision integral approximated by Bhatnagar-Gross-Krook (BGK) model [4]. The Riemann solver approach solves local Riemann problems (exactly or approximately) for Euler equations directly at a cell interface to evaluate the numerical flux for inviscid flow. For viscous flow case the Navier-Stokes equations are solved by using Riemann solver for the Euler part and central differencing for the viscous part [5]. The gas-kinetic BGK equation based schemes, on the other hand, have the possibility of treating the inviscid, viscous and free molecular flow cases with the same formulation [6–8]. This general feature of the solvers based on Boltzmann equation of kinetic theory therefore has attracted significant attention in the last few years.

The numerical schemes for hyperbolic scalar and vector conservation laws can be traced back to as early as 1950s when Lax [9] gave a first-order-accurate method for the Euler equations in the presence of shocks which gave monotonic but dissipative solution and hence very smeared results at the location of discontinuity. Lax-Wendroff [10] and MacCormack [11] are two of the earliest

second-order-accurate methods which show dispersive nature as evidenced by the presence of oscillations near the discontinuity. This oscillation was not a surprise as Godunov [12] showed that monotone behaviour of a solution cannot be assured for finite difference methods with more than first order accuracy and the above mentioned methods are second order accurate. Thus, a higher order method always seems to give oscillations at the site of discontinuity which must be avoided by some means. Harten and Zwas [13] used a hybrid scheme which was a hybrid of Lax method (1st order dissipative) and Lax-Wendroff method (2nd order dispersive) to reduce dispersion and improve monotone character. One of the ideas which was used to tackle the oscillation problem is the inclusion of *artificial viscosity* term which damps out the oscillations but not completely. Van Leer [14] showed that the Lax-Wendroff scheme can be made monotonic only if the scheme becomes nonconservative. In 1974 Van Leer [15] in the sequel of papers titled *Towards the Ultimate Conservation Difference Scheme* made Fromm's second order scheme [16] for the linear advection equation monotonic through the inclusion of nonlinear feedback terms. The aim of all these attempts of Van Leer was to make the second order schemes monotonic and conservative at the same time. In the same sequence of papers Van Leer [17] formulated finite-difference upstream-centered convective schemes for ideal compressible flow equations but it did not give any considerable improvement in the results. In the next sequence [18] in the same year he proposed a new approach for numerical convection which used a mesh-wise approximation of the initial-value distribution by simple basic functions like Legendre polynomials. The final paper [19] in the series published in 1979, where second order accurate method for ideal compressible flow is described, can be used across shocks. The scheme is a second order version of Godunov's (1959) method where the second order accuracy is achieved by taking the distributions of the state quantities inside a gas control volume to be linear in contrast with the uniform distribution taken in original Godunov scheme. This scheme is known as MUSCL (Monotonic Upstream-centered Scheme for Conservation Laws) scheme. In 1978 Amiram Harten [20] gave a new method to deal with shock and contact discontinuity. He hybridized an already existing finite difference scheme with a first order accurate method which then provided monotonicity and on top of that artificial compression was applied for sharpening the discontinuities. The flux-splitting approach was started by Steger and Warming [21] in 1981. In the conservation form the flux vectors of the Euler equations are homogeneous functions of degree one and this property allows the flux vectors to be split into subvectors by similarity transformations such that each subvector has a corresponding specified eigenvalue spectrum. This eigenvalue based splitting makes it possible to develop appropriate one sided spatial differences for each split flux for getting new explicit and implicit dissipative finite difference schemes without caring about

whether the flow field is subsonic or supersonic. The same year Roe [22] followed a Godunov type scheme [12] to solve Euler equations where he did not solve the exact Riemann problem at the control volume interfaces, rather he constructed an approximate Jacobian matrix of the flux vector and hence solved an approximate Riemann solver which is computationally efficient in comparison to the the original Godunov procedure. The disadvantage with this method is that the scheme cannot distinguish between a compression shock and expansion shock and the existence of expansion shock violates entropy condition and hence produces nonphysical results in such cases. Van Leer [23] proposed a different splitting, defined so that the flux terms were continuously differentiable through sonic and stagnation zones. This way he gave a solution to the problem present in the splitting method given by Steger and Warming [21]. The splitting of Van Leer was basically Mach number based. Harten [24] proposed high resolution schemes for hyperbolic conservation laws. These schemes were obtained by applying non-oscillatory first order accurate scheme to an appropriately modified flux function. He introduced the notion of a total-variation-diminishing (TVD) scheme. Osher and Chakravarthy [25] presented procedures for constructing second-order-accurate TVD approximations to scalar conservation laws which were constructed to also satisfy a single discrete entropy inequality. In 1984 Sweby [26] gave another technique for obtaining TVD and hence oscillation-free second order explicit difference schemes. To obtain such a scheme he used limited antidiffusive flux to a first order scheme and derived bounds for such limiters. He came up to this idea by investigating Roe [27], Van Leer [15], Chakravarthy and Osher [25], etc., schemes which in some way used different kind of limiters to get rid of the oscillations. He actually generalized the limiters methodology. Colella [28] presented another second order accurate method for solving gas dynamics equation similar to that of Van Leer's 1979 MUSCL scheme. The difference between the two second order methods is, that Van Leer scheme is in Lagrangian coordinates but Colella's scheme is in Eulerian, and also the method makes Eulerian calculations in a single step by solving Riemann problems and characteristic equations for the fluxes. In 1990 another approach for solving hyperbolic conservation laws using central differencing was proposed by Haim Nessyahu and Tadmor [29] which was non-oscillatory also. Most of the non-oscillatory schemes at that time were using upwind differencing with approximate Godunov solver, however, in this new approach Lax-Friedrichs scheme was used which is too dissipative, and to counteract that MUSCL type interpolants were used. This way no Riemann problem is needed to be solved but the accuracy obtained is comparable to that of the Godunov type methods. In 1993 Liou and Steffen [30] gave a new flux splitting scheme named *Advection Upstream Splitting Method* (AUSM) which is simple, accurate and converges as fast as the Roe method. They also introduced new pressure splitting which resulted into

much smoother results than the other existing splitting methods. In the year 1995, Venkatakrishnan [31] formulated new limiter for getting steady state solutions of the Euler equations on unstructured grids. Billet and Louedin [32] improved the MUSCL approach by AUSM splitting and a triad of adaptive limiters for unsteady flows. TVD schemes for unstructured grids which are general and accurate and recover the exact TVD formulation in structured grids has been developed by Darwish and Moukalled [33]. Parent [34] gave positivity preserving high-resolution schemes for systems of conservation laws. The most commonly used flux discretization schemes, namely, Roe and AUSM do not preserve the positivity in all situations so this problem associated with positivity preservation has been considered by him. This is important because nonpositivity makes the solution out of the physically admissible boundedness and convergence difficulties may also arise. This scheme [34] was obtained by making the Steger-Warming method second order accurate using component-wise TVD flux limiters, while ensuring that the coefficients of the discretized equation remain positive. The discussion so far in this paragraph gave a short summary of some important schemes which directly discretizes the governing equations at the macroscopic level. The next paragraph discusses some kinetic theory based schemes.

The earliest of the kinetic schemes include equilibrium flux method (EFM) of Pullin [35] and kinetic numerical method (KNM) of Reitz [36]. Both of these approaches use the collisionless Boltzmann equation to simulate the evolution of inviscid ideal gas flow. The inviscid gas flow governed by the Euler equations at the macroscopic level is governed at the microscopic level by the Boltzmann equation of kinetic theory when the velocity distribution function is Maxwellian under local equilibrium. The collision integral vanishes for Maxwellian distribution and hence the name "collisionless Boltzmann equation". EFM and KNM methods treat this collisionless Boltzmann equation as advection equation where the molecules freely move with their local velocities and the distribution function gets advected. EFM calculates the numerical flux at a cell face by taking suitable moments of the advected distribution function from local neighbouring cells assuming constant distribution in a cell initially. KNM does the same but it takes contribution of the advected distribution function from distant cells as well and uses numerical integration while taking moments. The local information exchange in EFM makes it conditionally stable whereas the long range exchange gives unconditional stability to KNM scheme. A very similar to EFM approach is the kinetic flux vector splitting (KFVS) method [37, 38]. KFVS looks at the local advection in EFM procedure more systematically and directly uses CIR splitting method for the collisionless Boltzmann equation and then takes the moment to get an Euler level scheme. The numerical fluxes in KFVS contain error functions and can be written in a closed form. These error functions were at first obtained by Pullin in his EFM [35]. The main drawback of

these schemes is the large amount of numerical dissipation causing heavy smearing of shocks, contacts and other high-gradient regions in a flow. The two identifiable reasons for this problem are, numerical truncation error and the use of collisionless Boltzmann equation that does not correspond to Euler equation evolution at macroscopic level for finite grid size and time steps [6]. To address this dissipation problem higher order versions of KFVS and KNM schemes have been formulated in the literature [6, 38–41] which reduce the dissipation. As explained in [6] the lack of particle collision mechanism in the collisionless equation makes the schemes unable to capture contact discontinuity and slip lines properly. Furthermore, it says that the pseudo collisions introduced in the implementation of KFVS scheme while preparing the equilibrium distribution for the next time step allows the discontinuities to be captured satisfactorily. This pseudo collision and free stream convection is equivalent to solving a modified gas-kinetic BGK equation [6] where the relaxation time of molecular collisions is equal to the numerical time step. The references [6, 7, 42–44] and others have formulated gas-kinetic BGK equation-based Euler and Navier-Stokes solvers where the molecular collisions have been properly taken care of. Although BGK type schemes improve the accuracy over schemes based on collisionless Boltzmann equation, the complexity and reduced computational efficiency is the price to be paid. This is the reason why research is still on for the development of simple, efficient and accurate schemes based on collisionless Boltzmann equation. In this line many improvements have been made. The peculiar velocity upwind (PVU) method of Rao and Deshpande [45] improved the efficiency over KFVS scheme by avoiding the calculation of error functions in flux calculation, but this resulted in a more diffusive scheme [46]. Several higher order versions of KFVS, as already mentioned, reduce the truncation error and probably indirectly improve the pseudo collision effect to tackle the dissipation by obtaining a smaller relaxation time than the CFL time step. Ramesh and Deshpande [41] and Anil et al. [47] have formulated modified KFVS schemes which are less dissipative than KFVS. The modified KFVS (m-KFVS) [47] performs as good as a second order scheme while still using stencil for first order scheme and hence is very efficient. The dissipation control parameter used in m-KFVS has been devised using some physical arguments and the scheme performs well in subsonic, supersonic and hypersonic flow regimes. The KFVS type schemes have also been formulated in meshless framework [48] and on unstructured grids [49, 50].

1.2 Motivation and Objectives

In the paper by Deshpande [39] a high resolution second-order-accurate KNM (a second order version of Reitz [36] type KNM) has been formulated which uses Chapman-Enskog power series expansion method to construct antidiffusive terms for cancelling excessive dissipation in KNM. The complexity in this procedure of obtaining higher order accuracy has motivated other researchers to look for a straightforward way. The works of Mandal and Deshpande [38], Ghosh et. al. [40], Perthame [51], and many others have achieved higher order accuracy without invoking Chapman-Enskog theory; however, a limiter-based formulation giving sufficient room for inclusion of already existing limiters of various kinds designed for specific purposes appears to be absent. This provides the motivation for the new flux-limited kinetic scheme proposed in the thesis. The computational cost for this scheme is comparable to already existing limiter based schemes [52, 53], which therefore, motivated a flux-corrected kinetic scheme for the Euler equations that does not require flux-splitting, and hence reduces computational cost significantly when compared to the FLKS and HRKFVS [38] schemes. Broadly the objectives of the thesis are the following:

1. Development of a 1D flux-limiting approach based kinetic scheme which should allow incorporation of any conventional or sophisticated limiter.
2. Extension of this scheme to 2D on Cartesian and unstructured grids.
3. Extension of the flux-limiting scheme for the 2D Euler equations to Navier-Stokes equations using the Chapman-Enskog methodology.
4. Development of a flux-corrected kinetic scheme with simple numerical flux formula without any split fluxes such that the computations will be significantly less costly when compared to the FLKS and HRKFVS schemes.
5. Validating each proposed scheme and its extension using suitable test problems.

1.3 Outline of the Thesis

The thesis first gives some background information in Chapter 2. The new FLKS scheme for 1D Euler equations is then discussed in Chapter 3. Chapter 4 extends the 1D FLKS scheme to 2D on Cartesian Grids. Chapter 5 demonstrates two different ways to obtain a Navier-Stokes solver based on FLKS. Chapter 6 suggests a procedure to implement the FLKS scheme on

triangular unstructured grids. Chapter 7 proposes a new flux-corrected kinetic scheme for the Euler equations. Finally, Chapter 8 concludes the work presented in the thesis.

Chapter 2

Governing Equations

This chapter reviews the governing equations of gas dynamics, namely, the Euler equations and the Navier-Stokes equations. These equations can be obtained by taking suitable moments of the Boltzmann equations of kinetic theory. The kinetic theory based schemes presented in this thesis use this connection and therefore, the Boltzmann equation and its connection with the gas dynamics equations are discussed. The KFVS scheme [37, 38] for 1D Euler equations, giving relevant background and notations needed for discussions in subsequent chapters, is also included here.

2.1 1D Euler Equations

The unsteady 1D Euler equations in Cartesian coordinates are given by

$$\frac{\partial \mathbf{U}}{\partial t} + \frac{\partial \mathbf{FX}}{\partial x} = 0, \tag{2.1.1}$$

where

$$\mathbf{U} = \begin{bmatrix} U^{(1)} \\ U^{(2)} \\ U^{(3)} \end{bmatrix} = \begin{bmatrix} \rho \\ \rho u \\ \rho e \end{bmatrix} \quad \text{and} \quad \mathbf{FX} = \begin{bmatrix} FX^{(1)} \\ FX^{(2)} \\ FX^{(3)} \end{bmatrix} = \begin{bmatrix} \rho u \\ p + \rho u^2 \\ (p + \rho e)u \end{bmatrix} \tag{2.1.2}$$

are the conservative variable vector and the flux vector, respectively. Here, ρ is density, p is pressure, u is fluid velocity and $e = \frac{p}{\rho(\gamma-1)} + \frac{u^2}{2}$ is total energy per unit mass for a perfect gas with the ratio of specific heats γ.

2.2 Relation between 1D Collisionless Boltzmann Equation and 1D Euler Equations

The collisionless 1D Boltzmann equation is

$$\frac{\partial F}{\partial t} + v_1 \frac{\partial F}{\partial x} = 0, \tag{2.2.1}$$

where v_1 is molecular velocity and F is the Maxwellian distribution function given by

$$F = \frac{\rho}{I_0}\sqrt{\frac{\beta}{\pi}} \exp\left\{-\beta(v_1 - u)^2 - \frac{I}{I_0}\right\}. \tag{2.2.2}$$

Here $I_0 = \frac{3-\gamma}{2(\gamma-1)}RT$, $\beta = \frac{1}{2RT}$, T is temperature, R is gas constant per unit mass and I is internal energy variable corresponding to non-translational degree of freedom. Now taking a "moment function vector $\boldsymbol{\Psi}$" as

$$\boldsymbol{\Psi} = \begin{bmatrix} 1 \\ v_1 \\ I + \frac{v_1^2}{2} \end{bmatrix} \tag{2.2.3}$$

allows one to define the $\boldsymbol{\Psi}$-moment of a distribution function f as

$$\langle \boldsymbol{\Psi}, f \rangle = \int_0^\infty dI \int_{-\infty}^{\infty} dv_1 \boldsymbol{\Psi} f. \tag{2.2.4}$$

The 1D Euler Equations given by equation (2.1.1) is obtained by taking the $\boldsymbol{\Psi}$-moment of equation (2.2.1):

$$\left\langle \boldsymbol{\Psi}, \frac{\partial F}{\partial t} + v_1 \frac{\partial F}{\partial x} \right\rangle = \frac{\partial \mathbf{U}}{\partial t} + \frac{\partial \mathbf{FX}}{\partial x} = 0,$$

where

$$\mathbf{U} = \int_0^\infty dI \int_{-\infty}^{\infty} dv_1 \boldsymbol{\Psi} F \tag{2.2.5a}$$

$$\text{and} \quad \mathbf{FX} = \int_0^\infty dI \int_{-\infty}^{\infty} dv_1 \boldsymbol{\Psi} v_1 F. \tag{2.2.5b}$$

These integrations are carried out in Appendix A.

2.3 KFVS Scheme

Since the $\boldsymbol{\Psi}$-moment of Boltzmann equation (2.2.1) gives Euler equations (2.1.1), the KFVS scheme uses this so called "moment method strategy" [38] to convert a Boltzmann level scheme to Euler level scheme.

A CIR scheme for Boltzmann equation (2.2.1) gives

$$F_i^{n+1} = F_i^n - \frac{v_1 + |v_1|}{2}\frac{\Delta t}{\Delta x}(F_i^n - F_{i-1}^n) - \frac{v_1 - |v_1|}{2}\frac{\Delta t}{\Delta x}(F_{i+1}^n - F_i^n), \tag{2.3.1}$$

where Δt is time step and Δx is grid spacing such that $x = i\Delta x$ and $t = n\Delta t$. Here i and n denote grid point and time level, respectively. This equation is an upwind scheme for equation (2.2.1). Taking the $\boldsymbol{\Psi}$-moment of equation (2.3.1) gives the first-order-accurate explicit KFVS scheme for the Euler equations (2.1.1) as

$$\mathbf{U}_i^{n+1} = \mathbf{U}_i^n - \lambda\left[(\mathbf{FX}_i^{+^n} - \mathbf{FX}_{i-1}^{+^n}) + (\mathbf{FX}_{i+1}^{-^n} - \mathbf{FX}_i^{-^n})\right], \tag{2.3.2}$$

where $\lambda = \frac{\Delta t}{\Delta x}$ and

$$\begin{aligned}\mathbf{FX}^{\pm} = \begin{bmatrix} FX^{(1)^{\pm}} \\ FX^{(2)^{\pm}} \\ FX^{(3)^{\pm}} \end{bmatrix} &= \left\langle \boldsymbol{\Psi}, \frac{v_1 \pm |v_1|}{2} F \right\rangle \\ &= \begin{bmatrix} \rho u X^{\pm} \pm \rho Y \\ (p + \rho u^2)X^{\pm} \pm \rho u Y \\ \left(\frac{\gamma p}{\gamma - 1} + \frac{1}{2}\rho u^2\right) u X^{\pm} \pm \left\{\frac{\gamma+1}{2(\gamma-1)}p + \frac{1}{2}\rho u^2\right\} Y \end{bmatrix},\end{aligned} \tag{2.3.3}$$

and

$$X^{\pm} = \frac{1 \pm \mathrm{erf}(S)}{2}, \quad Y = \frac{e^{-S^2}}{2\sqrt{\pi\beta}}, \quad S = u\sqrt{\beta}. \tag{2.3.4}$$

It follows that

$$\mathbf{FX} = \mathbf{FX}^{+} + \mathbf{FX}^{-}. \tag{2.3.5}$$

Thus the flux vector $\mathbf{FX}$ gets split into two parts $\mathbf{FX}^{+}$ and $\mathbf{FX}^{-}$, and hence the name "kinetic flux vector splitting" for equation (2.3.2). It has also been shown [38] that the eigenvalues corresponding to $\mathbf{FX}^{+}$ and $\mathbf{FX}^{-}$ are non-negative and non-positive, respectively. Thus the KFVS scheme provides upwinding at Euler level as well.

2.4 2D Euler Equations

The unsteady 2D Euler equations in Cartesian coordinates are given by

$$\frac{\partial \mathbf{U}}{\partial t} + \frac{\partial \mathbf{FX}}{\partial x} + \frac{\partial \mathbf{FY}}{\partial y} = 0, \tag{2.4.1}$$

where

$$\mathbf{U} = \begin{bmatrix} U^{(1)} \\ U^{(2)} \\ U^{(3)} \\ U^{(4)} \end{bmatrix} = \begin{bmatrix} \rho \\ \rho u \\ \rho v \\ \rho e \end{bmatrix}, \quad \mathbf{FX} = \begin{bmatrix} FX^{(1)} \\ FX^{(2)} \\ FX^{(3)} \\ FX^{(4)} \end{bmatrix} = \begin{bmatrix} \rho u \\ p + \rho u^2 \\ \rho uv \\ (p + \rho e)u \end{bmatrix} \quad \text{and} \quad \mathbf{FY} = \begin{bmatrix} FY^{(1)} \\ FY^{(2)} \\ FY^{(3)} \\ FY^{(4)} \end{bmatrix} = \begin{bmatrix} \rho v \\ \rho uv \\ p + \rho v^2 \\ (p + \rho e)v \end{bmatrix} \tag{2.4.2}$$

are the conservative variable vector, the flux vector in x-direction and the flux vector in y-direction, respectively. Here, ρ is density, p is pressure, u and v are x- and y-components of fluid velocity, respectively and $e = \frac{p}{\rho(\gamma-1)} + \frac{u^2+v^2}{2}$ is total energy per unit mass for ideal gas.

2.5 Relation between 2D Collisionless Boltzmann Equation and 2D Euler equations

The collisionless Boltzmann equation in 2D is

$$\frac{\partial F}{\partial t} + v_1 \frac{\partial F}{\partial x} + v_2 \frac{\partial F}{\partial y} = 0, \tag{2.5.1}$$

where v_1 and v_2 are x- and y-components of molecular velocity, respectively, and F is the Maxwellian distribution function given by

$$F = \frac{\rho}{I_0} \left(\frac{\beta}{\pi}\right) \exp\left[-\beta \left\{(v_1 - u)^2 + (v_2 - v)^2\right\} - \frac{I}{I_0}\right]. \tag{2.5.2}$$

Here $I_0 = \frac{2-\gamma}{\gamma-1} RT$, $\beta = \frac{1}{2RT}$, T is temperature, R is gas constant per unit mass and I is internal energy variable corresponding to non-translational degree of freedom. Now taking the "moment function vector $\boldsymbol{\Psi}$" as

$$\boldsymbol{\Psi} = \begin{bmatrix} 1 \\ v_1 \\ v_2 \\ I + \frac{v_1^2+v_2^2}{2} \end{bmatrix} \tag{2.5.3}$$

the $\boldsymbol{\Psi}$-moment of a distribution function f is defined as

$$\langle \boldsymbol{\Psi}, f \rangle = \int_0^\infty dI \int_{-\infty}^\infty dv_1 \int_{-\infty}^\infty dv_2 \boldsymbol{\Psi} f. \tag{2.5.4}$$

The 2D Euler equations given by equation (2.4.1) is obtained by taking the $\boldsymbol{\Psi}$-moment of equation (2.5.1), i.e.,

$$\left\langle \boldsymbol{\Psi}, \frac{\partial F}{\partial t} + v_1 \frac{\partial F}{\partial x} + v_2 \frac{\partial F}{\partial y} \right\rangle = \frac{\partial \mathbf{U}}{\partial t} + \frac{\partial \mathbf{FX}}{\partial x} + \frac{\partial \mathbf{FY}}{\partial y} = 0,$$

where

$$\mathbf{U} = \int_0^\infty dI \int_{-\infty}^\infty dv_1 \int_{-\infty}^\infty dv_2 \boldsymbol{\Psi} F, \tag{2.5.5a}$$

$$\mathbf{FX} = \int_0^\infty dI \int_{-\infty}^\infty dv_1 \int_{-\infty}^\infty dv_2 \boldsymbol{\Psi} v_1 F \tag{2.5.5b}$$

$$\text{and} \quad \mathbf{FY} = \int_0^\infty dI \int_{-\infty}^\infty dv_1 \int_{-\infty}^\infty dv_2 \boldsymbol{\Psi} v_2 F \tag{2.5.5c}$$

2.6 The Navier-Stokes Equations

The unsteady 2D Navier-Stokes equations in Cartesian coordinates are given by

$$\frac{\partial \mathbf{U}}{\partial t} + \frac{\partial \mathbf{FX}}{\partial x} + \frac{\partial \mathbf{FY}}{\partial y} = \frac{\partial \mathbf{FX}_v}{\partial x} + \frac{\partial \mathbf{FY}_v}{\partial y}, \tag{2.6.1}$$

where the left hand side is the same as that in the 2D Euler equations (2.4.1) and the right hand side are the viscous terms. Here $\mathbf{FX}_v$ and $\mathbf{FY}_v$ are the viscous fluxes in x- and y-directions, respectively, as given by equations (2.6.2).

$$\mathbf{FX}_v = \begin{bmatrix} FX_v^{(1)} \\ FX_v^{(2)} \\ FX_v^{(3)} \\ FX_v^{(4)} \end{bmatrix} = \begin{bmatrix} 0 \\ \sigma_{xx} \\ \sigma_{xy} \\ \sigma_{xx}u + \sigma_{xy}v + k\frac{\partial T}{\partial x} \end{bmatrix} \quad \text{and} \quad \mathbf{FY}_v = \begin{bmatrix} FY_v^{(1)} \\ FY_v^{(2)} \\ FY_v^{(3)} \\ FY_v^{(4)} \end{bmatrix} = \begin{bmatrix} 0 \\ \sigma_{yx} \\ \sigma_{yy} \\ \sigma_{yx}u + \sigma_{yy}v + k\frac{\partial T}{\partial y} \end{bmatrix}, \tag{2.6.2}$$

where

$$\sigma_{xx} = 2\mu \frac{\partial u}{\partial x} - \frac{2\mu}{3}\left(\frac{\partial u}{\partial x} + \frac{\partial v}{\partial y}\right), \tag{2.6.3a}$$

$$\sigma_{yy} = 2\mu \frac{\partial v}{\partial y} - \frac{2\mu}{3}\left(\frac{\partial u}{\partial x} + \frac{\partial v}{\partial y}\right), \tag{2.6.3b}$$

$$\sigma_{xy} = \sigma_{yx} = \mu\left(\frac{\partial u}{\partial y} + \frac{\partial v}{\partial x}\right) \tag{2.6.3c}$$

are the components of viscous stress tensor, and μ and k are coefficients of viscosity and thermal conductivity, respectively.

2.7 Relation between 2D Collisional Boltzmann Equation and 2D Navier-Stokes equations

The 2D Boltzmann equation is

$$\frac{\partial f}{\partial t} + v_1 \frac{\partial f}{\partial x} + v_2 \frac{\partial f}{\partial y} = \left(\frac{\partial f}{\partial t}\right)_{coll}, \tag{2.7.1}$$

where $\left(\frac{\partial f}{\partial t}\right)_{coll}$ is the collision term. Replacing the collision term by the BGK collision model [4] gives the BGK equation

$$\frac{\partial f}{\partial t} + v_1 \frac{\partial f}{\partial x} + v_2 \frac{\partial f}{\partial y} = -\frac{f - F}{\tau}, \tag{2.7.2}$$

where F is the local Maxwellian given by (2.5.2), and τ is the particle collision time. It is well-known [2, 39] that the 2D Navier-Stokes equations can be obtained by taking the $\boldsymbol{\Psi}$-moment of equation (2.7.2) with $\boldsymbol{\Psi}$ given by equation (2.5.3) keeping the first two terms of the Chapman-Enskog expansion of the velocity distribution function f, i.e.,

$$\begin{aligned} f &= F - \tau \left(\frac{\partial F}{\partial t} + v_1 \frac{\partial F}{\partial x} + v_2 \frac{\partial F}{\partial y} \right) \\ &= F - \tau (DF). \end{aligned} \tag{2.7.3}$$

This Chapman-Enskog procedure gives $\mu = \tau p$ as the coefficient of dynamic viscosity and Prandtl number $\mathrm{Pr} = 1$.

2.8 Conclusions

The Euler and the Navier-Stokes equations of gas dynamics, and their connection to the Boltzmann equation of kinetic theory is discussed in this chapter. This clearly demonstrates that $\boldsymbol{\Psi}$-moment of the Boltzmann equation with suitable distribution function gives the gas dynamics equations. This transition methodology to go from the Boltzmann level to the macroscopic level is the key to the development of many kinetic theory based schemes including the new schemes that the thesis discusses. The next several chapters elaborate on how the moment methodology can produce new schemes.

Chapter 3

A New Flux-Limiting Approach Based Kinetic Scheme for 1D Euler Equations

This chapter uses the Sweby's flux-limited method [26] to discretize the collisionless Boltzmann equation and then moment is taken to get an Euler level scheme which is referred to as "Flux Limited Kinetic Solver (FLKS)". The basic motivation behind using flux-limiting at the Boltzmann level is to explore the possibility of achieving high resolution and close to second order convergence at Euler level by moment method, and hence assessing the correspondence between Boltzmann and Euler level in transferring the resolution and order of accuracy property from one level to another. The works of Mandal and Deshpande [38], Ghosh et al. [40], Perthame [51], and many others have achieved higher order accuracy, however, a limiter-based formulation giving sufficient room for inclusion of already existing limiters of various kinds designed for specific purposes appears to be absent. This provides the motivation for the present scheme.

3.1 Derivation of FLKS Scheme for 1D Euler Equations

The "moment method strategy" used in the derivation of KFVS scheme is the key for the development of many schemes [39, 40, 45, 47, 48, 54], some of which are higher order versions of KFVS. In the present work a new high resolution scheme based on flux-limiting [26] is formulated. The simple idea is that if the CIR scheme at the Boltzmann level gives an upwind scheme at the

Euler level, then a flux-limited scheme for Boltzmann equation (2.2.1) is expected to produce a flux-limited Euler level scheme.

Referring to Sweby [26], the 1D collisionless Boltzmann equation (2.2.1) considered as a linear advection equation can be discretized as

$$\begin{aligned} F_i^{n+1} = F_i^n - \lambda \big[& v_1 (F_i^n - F_{i-1}^n) + \frac{v_1}{2}(1 - \lambda v_1)\{\Phi(r_i^+)(F_{i+1}^n - F_i^n) \\ & - \Phi(r_{i-1}^+)(F_i^n - F_{i-1}^n)\}\big] \quad \text{for} \quad v_1 > 0 \end{aligned} \tag{3.1.1a}$$

and

$$\begin{aligned} F_i^{n+1} = F_i^n - \lambda \big[& v_1 (F_{i+1}^n - F_i^n) - \frac{v_1}{2}(1 + \lambda v_1)\{\Phi(r_{i+1}^-)(F_{i+1}^n - F_i^n) \\ & - \Phi(r_i^-)(F_i^n - F_{i-1}^n)\}\big] \quad \text{for} \quad v_1 < 0 \end{aligned} \tag{3.1.1b}$$

where $\Phi(r_i^+)$, $\Phi(r_i^-)$, etc., terms are flux-limiters and satisfy the following conditions for equation (3.1.1) to be a TVD scheme for equation (2.2.1),

$$\begin{cases} 0 \le \Phi(r_i^+) \le \min(2, 2r_i^+), & r_i^+ \ge 0 \\ \Phi(r_i^+) = 0, & r_i^+ < 0 \end{cases} \tag{3.1.2a}$$

$$\text{and} \quad \begin{cases} 0 \le \Phi(r_i^-) \le \min(2, 2r_i^-), & r_i^- \ge 0 \\ \Phi(r_i^-) = 0, & r_i^- < 0 \end{cases} \tag{3.1.2b}$$

where

$$r_i^+ = \frac{F_i^n - F_{i-1}^n}{F_{i+1}^n - F_i^n} \tag{3.1.3a}$$

$$\text{and} \quad r_i^- = \frac{F_{i+1}^n - F_i^n}{F_i^n - F_{i-1}^n}. \tag{3.1.3b}$$

The nonlinear stability bound on $\Phi(r_i^+)$ in terms of r_i^+ is same as that on $\Phi(r_i^-)$ in terms of r_i^-. Thus the common bound can be written as

$$\begin{cases} 0 \le \Phi(r) \le \min(2, 2r), & r \ge 0 \\ \Phi(r) = 0, & r < 0 \end{cases} \tag{3.1.4}$$

without subscript and superscript on r. This bound on $\Phi(r)$ is shown in Figure 3.1(a) where the shaded region plus the negative r-axis is the TVD region. Figure 3.1(b) shows some conventional limiters. Line CG is for Lax-Wendroff, BKE for Warming-Beam, LKM for Fromm, ABKG for

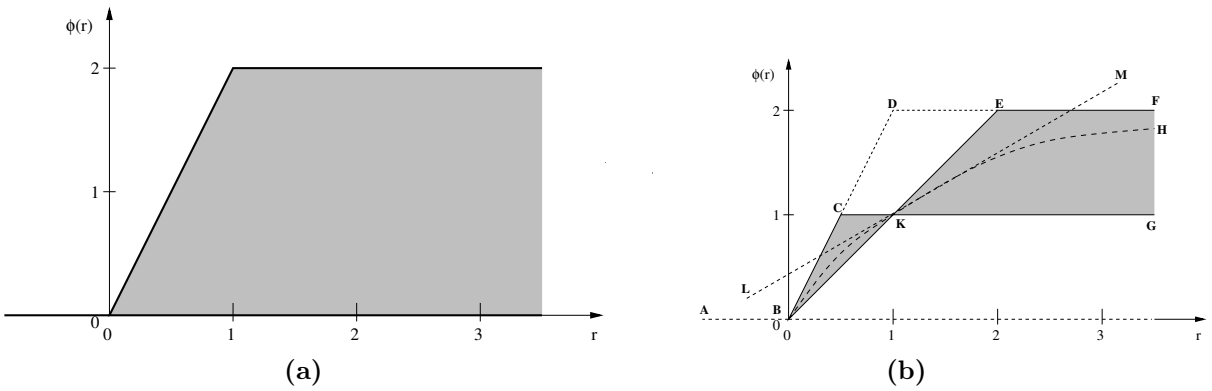

Figure 3.1. (a) Sweby TVD region and (b) some conventional limiters.

minmod, ABKH for Van Leer and ABCKEF is for superbee limiter. Out of these limiters only the minmod, Van Leer and superbee limiters satisfy the TVD condition given by (3.1.4) and these limiters are confined in the shaded region of Figure 3.1(b) which is the second order zone, i.e., for $\Phi(r)$ in this region the scheme (3.1.1) will be second order accurate.

In CIR scheme (2.3.1) the upwinding is taken care of for both the cases, $v_1 > 0$ and $v_1 < 0$. Similarly for combining equations (3.1.1a) and (3.1.1b), we can write

$$F_i^{n+1} = \frac{1}{v_1}\left[\frac{v_1+|v_1|}{2}\,(\text{RHS of equation (3.1.1a)}) + \frac{v_1-|v_1|}{2}\,(\text{RHS of equation (3.1.1b)})\right]$$

which gives,

$$\begin{aligned} F_i^{n+1} = F_i^n &- \lambda\left\{\frac{v_1+|v_1|}{2}\left(F_i^n - F_{i-1}^n\right) + \frac{v_1-|v_1|}{2}\left(F_{i+1}^n - F_i^n\right)\right\} \\ &- \frac{\lambda}{2}\frac{v_1+|v_1|}{2}\left\{\Phi(r_i^+)\left(F_{i+1}^n - F_i^n\right) - \Phi(r_{i-1}^+)\left(F_i^n - F_{i-1}^n\right)\right\} \\ &+ \frac{\lambda}{2}\frac{v_1-|v_1|}{2}\left\{\Phi(r_{i+1}^-)\left(F_{i+1}^n - F_i^n\right) - \Phi(r_i^-)\left(F_i^n - F_{i-1}^n\right)\right\} \\ &+ \frac{\lambda^2}{2}v_1\frac{v_1+|v_1|}{2}\left\{\Phi(r_i^+)\left(F_{i+1}^n - F_i^n\right) - \Phi(r_{i-1}^+)\left(F_i^n - F_{i-1}^n\right)\right\} \\ &+ \frac{\lambda^2}{2}v_1\frac{v_1-|v_1|}{2}\left\{\Phi(r_{i+1}^-)\left(F_{i+1}^n - F_i^n\right) - \Phi(r_i^-)\left(F_i^n - F_{i-1}^n\right)\right\}. \end{aligned} \tag{3.1.5}$$

This is a Boltzmann level flux-limited scheme.

Now, for an Euler level flux-limited scheme corresponding to equation (3.1.5), the "moment method strategy" can be applied. Here we describe three slightly different methods for taking the $\boldsymbol{\Psi}$-moment of scheme (3.1.5).

3.1.1 Method 1

The $\Phi(r)$ terms in scheme (3.1.5) is first replaced by an averaging function $\text{avg}(1, r)$ which satisfies TVD condition (3.1.2). Following the work of Jameson [55], an averaging function $\text{avg}(u, v)$ with any two parameters u and v should satisfy the following properties

$$\text{avg}(u, v) = \text{avg}(v, u) \tag{3.1.6a}$$

$$\alpha.\text{avg}(u, v) = \text{avg}(\alpha u, \alpha v) \tag{3.1.6b}$$

$$\text{avg}(u, u) = u \tag{3.1.6c}$$

$\text{avg}(u, v) = 0$ if u and v have opposite signs, otherwise $\text{avg}(u, v)$ has the same sign as u and v. (3.1.6d)

The first three properties (3.1.6a), (3.1.6b) and (3.1.6c) are natural properties of a reasonable average and the last one (3.1.6d) is required for construction of a TVD scheme.

It comes out that the well known flux limiters namely, minmod, Van Leer and superbee can be put in the averaging function form $\text{avg}(1, r)$ and all satisfy property (3.1.6). Jameson [55] mentions the following expressions

1. minmod:

$$\text{avg}(u, v) = \frac{1}{2}\{\text{sign}(u) + \text{sign}(v)\}\min(|u|, |v|) \tag{3.1.7a}$$

2. Van Leer:

$$\text{avg}(u, v) = \frac{1}{2}\{\text{sign}(u) + \text{sign}(v)\}\frac{2|u||v|}{|u| + |v|} \tag{3.1.7b}$$

3. superbee:

$$\text{avg}(u, v) = \frac{1}{2}\{\text{sign}(u) + \text{sign}(v)\}\max\{\min(2|u|, |v|), \min(|u|, 2|v|)\} \tag{3.1.7c}$$

where

$$\text{sign}(u) = \begin{cases} 1, & \text{if} \quad u > 0 \\ -1, & \text{if} \quad u < 0 \\ 0, & \text{if} \quad u = 0. \end{cases} \tag{3.1.8}$$

By putting $u = 1$ and $v = r$ in the above expressions the usual expressions for limiters mentioned in the work of Sweby [26] can be recovered with $\Phi(r) = \text{avg}(1, r)$.

The whole purpose of writing $\Phi(r)$ as $\text{avg}(1, r)$ is to avoid the explicit calculation of ratio r. To see this we notice a term in the Boltzmann level scheme (3.1.5), namely, $\Phi(r_i^+)\left(F_{i+1}^n - F_i^n\right)$.

Replacing $\Phi(r_i^+)$ with $\text{avg}(1, r_i^+)$ gives

$$\begin{aligned}
&\text{avg}(1, r_i^+)\left(F_{i+1}^n - F_i^n\right) \\
&= \text{avg}\left(1, \frac{F_i^n - F_{i-1}^n}{F_{i+1}^n - F_i^n}\right)\left(F_{i+1}^n - F_i^n\right) \\
&= \text{avg}(F_{i+1}^n - F_i^n, F_i^n - F_{i-1}^n). \quad \text{(following the property (3.1.6b))}
\end{aligned}$$

In this fashion all such terms containing $\Phi(r)$ in equation (3.1.5) can be converted to the averaging function form. Furthermore, the products like $\frac{v_1+|v_1|}{2}\Phi(r_i^+)\left(F_{i+1}^n - F_i^n\right)$ in equation (3.1.5) can be written as

$$\begin{aligned}
&\frac{v_1 + |v_1|}{2}\text{avg}(F_{i+1}^n - F_i^n, F_i^n - F_{i-1}^n) \\
&= \text{avg}\left(\frac{v_1 + |v_1|}{2}(F_{i+1}^n - F_i^n), \frac{v_1 + |v_1|}{2}(F_i^n - F_{i-1}^n)\right)
\end{aligned}$$

and similarly the products like $v_1\frac{v_1+|v_1|}{2}\Phi(r_i^+)\left(F_{i+1}^n - F_i^n\right)$ will become

$$\text{avg}\left(v_1\frac{v_1 + |v_1|}{2}(F_{i+1}^n - F_i^n), v_1\frac{v_1 + |v_1|}{2}(F_i^n - F_{i-1}^n)\right)$$

in view of the property (3.1.6b). Once all the terms containing $\Phi(r)$ in equation (3.1.5) are replaced by averaging function form, the $\boldsymbol{\Psi}$-moment of this equation can be taken to get the Euler level scheme. However, while taking moment, integrations like the following are encountered

$$\begin{aligned}
&\int_0^\infty dI \int_{-\infty}^\infty dv_1 \boldsymbol{\Psi} \text{avg}\left(\frac{v_1 \pm |v_1|}{2}(F_{i+1}^n - F_i^n), \frac{v_1 \pm |v_1|}{2}(F_i^n - F_{i-1}^n)\right), \\
&\int_0^\infty dI \int_{-\infty}^\infty dv_1 \boldsymbol{\Psi} \text{avg}\left(v_1\frac{v_1 \pm |v_1|}{2}(F_{i+1}^n - F_i^n), v_1\frac{v_1 \pm |v_1|}{2}(F_i^n - F_{i-1}^n)\right), \quad \text{etc.}
\end{aligned} \tag{3.1.9}$$

At this stage a crucial approximation is made and expressions (3.1.9) are replaced with

$$\begin{aligned}
&\text{avg}\left(\int_0^\infty dI \int_{-\infty}^\infty dv_1 \boldsymbol{\Psi}\frac{v_1 \pm |v_1|}{2}(F_{i+1}^n - F_i^n), \int_0^\infty dI \int_{-\infty}^\infty dv_1 \boldsymbol{\Psi}\frac{v_1 \pm |v_1|}{2}(F_i^n - F_{i-1}^n)\right), \\
&\text{avg}\left(\int_0^\infty dI \int_{-\infty}^\infty dv_1 \boldsymbol{\Psi} v_1\frac{v_1 \pm |v_1|}{2}(F_{i+1}^n - F_i^n), \int_0^\infty dI \int_{-\infty}^\infty dv_1 \boldsymbol{\Psi} v_1\frac{v_1 \pm |v_1|}{2}(F_i^n - F_{i-1}^n)\right), \quad \text{etc.},
\end{aligned} \tag{3.1.10}$$

where KFVS split fluxes "$\mathbf{FX}^\pm = \int_0^\infty dI \int_{-\infty}^\infty dv_1 \boldsymbol{\Psi}\frac{v_1 \pm |v_1|}{2}F$" can be recognized as the arguments for the first avg function for which closed form expressions (2.3.3) and (2.3.4) are already known.

The other avg function has arguments involving the moments given by

$$\begin{aligned}
\mathbf{GX}^{\pm} &= \int_0^{\infty} dI \int_{-\infty}^{\infty} dv_1 \boldsymbol{\Psi} v_1 \frac{v_1 \pm |v_1|}{2} F \\
&= \left\langle \boldsymbol{\Psi}, v_1 \frac{v_1 \pm |v_1|}{2} F \right\rangle \\
&= \begin{bmatrix} GX^{(1)^{\pm}} \\ GX^{(2)^{\pm}} \\ GX^{(3)^{\pm}} \end{bmatrix} \\
&= \begin{bmatrix} p + \rho u^2 \\ (3p + \rho u^2)u \\ \frac{\gamma}{\gamma-1}\frac{p^2}{\rho} + pu^2\frac{5\gamma-3}{2(\gamma-1)} + \frac{\rho u^4}{2} \end{bmatrix} X^{\pm} \pm \begin{bmatrix} \rho u \\ 2p + \rho u^2 \\ (\frac{2\gamma-1}{\gamma-1}p + \frac{1}{2}\rho u^2)u \end{bmatrix} Y
\end{aligned} \tag{3.1.11}$$

where $X^{\pm}$ and Y are given by (2.3.4). With the approximation (3.1.10) and the new moments (3.1.11) defined, the $\boldsymbol{\Psi}$-moment of the Boltzmann level flux-limited scheme (3.1.5) becomes

$$\begin{aligned}
\mathbf{U}_i^{n+1} &= \mathbf{U}_i^n - \lambda\left[\left(\mathbf{FX}_i^{+^n} - \mathbf{FX}_{i-1}^{+^n}\right) + \left(\mathbf{FX}_{i+1}^{-^n} - \mathbf{FX}_i^{-^n}\right)\right] \\
&- \frac{\lambda}{2}\left[\text{avg}\left(\left(\mathbf{FX}_{i+1}^{+^n} - \mathbf{FX}_i^{+^n}\right), \left(\mathbf{FX}_i^{+^n} - \mathbf{FX}_{i-1}^{+^n}\right)\right) - \text{avg}\left(\left(\mathbf{FX}_i^{+^n} - \mathbf{FX}_{i-1}^{+^n}\right), \left(\mathbf{FX}_{i-1}^{+^n} - \mathbf{FX}_{i-2}^{+^n}\right)\right)\right] \\
&+ \frac{\lambda}{2}\left[\text{avg}\left(\left(\mathbf{FX}_{i+2}^{-^n} - \mathbf{FX}_{i+1}^{-^n}\right), \left(\mathbf{FX}_{i+1}^{-^n} - \mathbf{FX}_i^{-^n}\right)\right) - \text{avg}\left(\left(\mathbf{FX}_{i+1}^{-^n} - \mathbf{FX}_i^{-^n}\right), \left(\mathbf{FX}_i^{-^n} - \mathbf{FX}_{i-1}^{-^n}\right)\right)\right] \\
&+ \frac{\lambda^2}{2}\left[\text{avg}\left(\left(\mathbf{GX}_{i+1}^{+^n} - \mathbf{GX}_i^{+^n}\right), \left(\mathbf{GX}_i^{+^n} - \mathbf{GX}_{i-1}^{+^n}\right)\right) - \text{avg}\left(\left(\mathbf{GX}_i^{+^n} - \mathbf{GX}_{i-1}^{+^n}\right), \left(\mathbf{GX}_{i-1}^{+^n} - \mathbf{GX}_{i-2}^{+^n}\right)\right)\right] \\
&+ \frac{\lambda^2}{2}\left[\text{avg}\left(\left(\mathbf{GX}_{i+2}^{-^n} - \mathbf{GX}_{i+1}^{-^n}\right), \left(\mathbf{GX}_{i+1}^{-^n} - \mathbf{GX}_i^{-^n}\right)\right) - \text{avg}\left(\left(\mathbf{GX}_{i+1}^{-^n} - \mathbf{GX}_i^{-^n}\right), \left(\mathbf{GX}_i^{-^n} - \mathbf{GX}_{i-1}^{-^n}\right)\right)\right].
\end{aligned} \tag{3.1.12}$$

This is the Euler level flux-limited scheme. Here averaging function "avg" is given by equations (3.1.7) or any other average satisfying (3.1.6) and (3.1.4) when written in $\Phi(r) = \text{avg}(1, r)$ form at the Boltzmann level. In addition, it is clear that the approximation done in going from expressions (3.1.9) to (3.1.10) does not guarantee that the TVD condition (3.1.4) gets exactly satisfied at the Boltzmann level. So the Euler level scheme (3.1.12) is expected to be oscillatory or over diffusive at times, however, numerical experiments show that the scheme works well with negligible spurious oscillations near high gradients and the dissipation is significantly lower than any first order scheme. Furthermore, (3.1.12) can be written as

$$\mathbf{U}_i^{n+1} = \mathbf{U}_i^n - \lambda\left[\left(\mathbf{FX}_i^{+^n} - \mathbf{FX}_{i-1}^{+^n}\right) + \left(\mathbf{FX}_{i+1}^{-^n} - \mathbf{FX}_i^{-^n}\right)\right] + A,$$

where A refers to anti-dissipation terms.

Thus, the FLKS scheme can be seen as a higher order version of KFVS scheme. This is not

surprising because the Boltzmann level scheme (3.1.5) is nothing but a limited combination of CIR and Lax-Wendroff schemes. Any other combination, e.g., modified CIR [41, 47] and Lax-Wendroff, etc., with proper TVD criteria will give rise to a different limited scheme, but this thesis intends to explore kinetic version of conventional limiting procedures. Now using property (3.1.6b) scheme (3.1.12) can be rewritten as

$$\begin{aligned}
U_i^{(k)^{n+1}} &= U_i^{(k)^n} - \lambda\left[\left(FX_i^{(k)^{+^n}} - FX_{i-1}^{(k)^{+^n}}\right) + \left(FX_{i+1}^{(k)^{-^n}} - FX_i^{(k)^{-^n}}\right)\right] \\
&- \frac{\lambda}{2}\left[\Phi\left(R_i^{(k)^+}\right)\left(FX_{i+1}^{(k)^{+^n}} - FX_i^{(k)^{+^n}}\right) - \Phi\left(R_{i-1}^{(k)^+}\right)\left(FX_i^{(k)^{+^n}} - FX_{i-1}^{(k)^{+^n}}\right)\right] \\
&+ \frac{\lambda}{2}\left[\Phi\left(S_{i+1}^{(k)^-}\right)\left(FX_{i+1}^{(k)^{-^n}} - FX_i^{(k)^{-^n}}\right) - \Phi\left(S_i^{(k)^-}\right)\left(FX_i^{(k)^{-^n}} - FX_{i-1}^{(k)^{-^n}}\right)\right] \\
&+ \frac{\lambda^2}{2}\left[\Phi\left(T_i^{(k)^+}\right)\left(GX_{i+1}^{(k)^{+^n}} - GX_i^{(k)^{+^n}}\right) - \Phi\left(T_{i-1}^{(k)^+}\right)\left(GX_i^{(k)^{+^n}} - GX_{i-1}^{(k)^{+^n}}\right)\right] \\
&+ \frac{\lambda^2}{2}\left[\Phi\left(V_{i+1}^{(k)^-}\right)\left(GX_{i+1}^{(k)^{-^n}} - GX_i^{(k)^{-^n}}\right) - \Phi\left(V_i^{(k)^-}\right)\left(GX_i^{(k)^{-^n}} - GX_{i-1}^{(k)^{-^n}}\right)\right]; \quad k = 1, 2, 3
\end{aligned} \tag{3.1.13}$$

where

$$\begin{aligned}
\Phi\left(R_i^{(k)^+}\right) &= \text{avg}\left(1, R_i^{(k)^+}\right) \\
\Phi\left(S_i^{(k)^-}\right) &= \text{avg}\left(1, S_i^{(k)^-}\right) \\
\Phi\left(T_i^{(k)^+}\right) &= \text{avg}\left(1, T_i^{(k)^+}\right) \\
\Phi\left(V_i^{(k)^-}\right) &= \text{avg}\left(1, V_i^{(k)^-}\right)
\end{aligned} \tag{3.1.14}$$

and

$$\begin{aligned}
R_i^{(k)^+} &= \frac{FX_i^{(k)^{+^n}} - FX_{i-1}^{(k)^{+^n}}}{FX_{i+1}^{(k)^{+^n}} - FX_i^{(k)^{+^n}}} \\
S_i^{(k)^-} &= \frac{FX_{i+1}^{(k)^{-^n}} - FX_i^{(k)^{-^n}}}{FX_i^{(k)^{-^n}} - FX_{i-1}^{(k)^{-^n}}} \\
T_i^{(k)^+} &= \frac{GX_i^{(k)^{+^n}} - GX_{i-1}^{(k)^{+^n}}}{GX_{i+1}^{(k)^{+^n}} - GX_i^{(k)^{+^n}}} \\
V_i^{(k)^-} &= \frac{GX_{i+1}^{(k)^{-^n}} - GX_i^{(k)^{-^n}}}{GX_i^{(k)^{-^n}} - GX_{i-1}^{(k)^{-^n}}}.
\end{aligned} \tag{3.1.15}$$

In the form (3.1.13), the limiters can be incorporated conventionally by first figuring out the ratios (3.1.15). We notice here that the ratios use difference of "split fluxes" $FX^{\pm}$ and $GX^{\pm}$.

This "split flux" nomenclature is used because

$$\begin{aligned}\langle \boldsymbol{\Psi}, v_1 F\rangle &= \left\langle \boldsymbol{\Psi}, \frac{v_1+|v_1|}{2}F + \frac{v_1-|v_1|}{2}F \right\rangle \\ &= \left\langle \boldsymbol{\Psi}, \frac{v_1+|v_1|}{2}F \right\rangle + \left\langle \boldsymbol{\Psi}, \frac{v_1-|v_1|}{2}F \right\rangle \end{aligned} \tag{3.1.16a}$$

so that $$\mathbf{FX} = \mathbf{FX}^+ + \mathbf{FX}^-, \quad \text{which is already known by (2.3.5).} \tag{3.1.16b}$$

In addition,

$$\begin{aligned}\langle \boldsymbol{\Psi}, v_1^2 F\rangle &= \left\langle \boldsymbol{\Psi}, v_1\frac{v_1+|v_1|}{2}F + v_1\frac{v_1-|v_1|}{2}F \right\rangle \\ &= \left\langle \boldsymbol{\Psi}, v_1\frac{v_1+|v_1|}{2}F \right\rangle + \left\langle \boldsymbol{\Psi}, v_1\frac{v_1-|v_1|}{2}F \right\rangle \end{aligned} \tag{3.1.17a}$$

so that $$\mathbf{GX} = \mathbf{GX}^+ + \mathbf{GX}^-, \tag{3.1.17b}$$

where $\mathbf{GX} = \langle \boldsymbol{\Psi}, v_1^2 F\rangle$ kind of flux arises due to the use of Lax-Wendroff flux in flux-limiting in equation (3.1.1).

The flux-limited scheme of the form (3.1.13) can be utilized to formulate kinetic versions of some well-known second order accurate schemes which are not TVD, namely, Lax-Wendroff, Warming-Beam and Fromm schemes by taking

$$\begin{aligned}\Phi(r) &= 1 \quad \text{for Lax-Wendroff scheme} \\ &= r \quad \text{for Warming-Beam scheme} \\ &= \frac{1+r}{2} \quad \text{for Fromm scheme.}\end{aligned}$$

In addition, $\Phi(r) = 0$ gives the KFVS scheme which is a first order accurate TVD scheme. Finally, the scheme (3.1.12) is put in the conservation form

$$\mathbf{U}_i^{n+1} = \mathbf{U}_i^n - \lambda\left[\hat{\mathbf{f}}^n_{i+\frac{1}{2}} - \hat{\mathbf{f}}^n_{i-\frac{1}{2}}\right], \tag{3.1.18a}$$

where

$$\begin{aligned}\hat{\mathbf{f}}^{n}_{i+\frac{1}{2}} &= \left(\mathbf{FX}^{+^n}_{i} + \mathbf{FX}^{-^n}_{i+1}\right) \\ &+ \frac{1}{2}\text{avg}\left(\left(\mathbf{FX}^{+^n}_{i+1} - \mathbf{FX}^{+^n}_{i}\right), \left(\mathbf{FX}^{+^n}_{i} - \mathbf{FX}^{+^n}_{i-1}\right)\right) \\ &- \frac{1}{2}\text{avg}\left(\left(\mathbf{FX}^{-^n}_{i+2} - \mathbf{FX}^{-^n}_{i+1}\right), \left(\mathbf{FX}^{-^n}_{i+1} - \mathbf{FX}^{-^n}_{i}\right)\right) \\ &- \frac{\lambda}{2}\text{avg}\left(\left(\mathbf{GX}^{+^n}_{i+1} - \mathbf{GX}^{+^n}_{i}\right), \left(\mathbf{GX}^{+^n}_{i} - \mathbf{GX}^{+^n}_{i-1}\right)\right) \\ &- \frac{\lambda}{2}\text{avg}\left(\left(\mathbf{GX}^{-^n}_{i+2} - \mathbf{GX}^{-^n}_{i+1}\right), \left(\mathbf{GX}^{-^n}_{i+1} - \mathbf{GX}^{-^n}_{i}\right)\right)\end{aligned} \tag{3.1.18b}$$

is the time averaged numerical flux from time step n to $n+1$ at the cell interface position $x_{i+\frac{1}{2}}$. Here a 1D spatial domain is assumed with cell $\left[x_{i-\frac{1}{2}}, x_{i+\frac{1}{2}}\right]$ as the i^{th} cell with $\Delta x = x_{i+\frac{1}{2}} - x_{i-\frac{1}{2}}$.

3.1.2 Method 2

An alternative straightforward way to get an Euler level scheme from the Boltzmann level scheme (3.1.5) is the following:

Step 1: Calculate the ratios $r^{\pm}$ using (3.1.3).

Step 2: Calculate all $\Phi(r^{\pm})$ values using a limiter satisfying TVD criteria (3.1.4).

Step 3: Take the $\boldsymbol{\Psi}$-moment of equation (3.1.5).

While implementing these steps the first problem that arises is that the Boltzmann equation (2.2.1) is not a single linear advection equation. F is a velocity distribution function and the range of molecular velocity v_1 is from $-\infty$ to $+\infty$, so that equation (2.2.1) can be visualized as a system of infinitely many linear advection equations where in each equation a particular value of F is being advected by a particular v_1. Thus the ratios $r^{\pm}$ in scheme (3.1.5) are infinitely many valued and the same is the case with $\Phi(r^{\pm})$ values. The **Method** 1 circumvented this problem by using the avg function and using the approximation in going from (3.1.9) to (3.1.10). The form of equation (3.1.13) in this method clearly shows that a "representative ratio" (given by the ratio of differences of split fluxes (3.1.15)) to obtain single values of $r^{\pm}$ and hence $\Phi(r^{\pm})$ works. This use of representative ratio provides motivation to try other ways to calculate single values of $r^{\pm}$ and $\Phi(r^{\pm})$. The following procedure is followed:

Step 1: Calculate the ratios $r^{\pm}$ using the conservative variables. Use

$$r_i^+ = \begin{cases} \frac{U_i^{(1)^n} - U_{i-1}^{(1)^n}}{U_{i+1}^{(1)^n} - U_i^{(1)^n}} & \text{in mass equation,} \\ \frac{U_i^{(2)^n} - U_{i-1}^{(2)^n}}{U_{i+1}^{(2)^n} - U_i^{(2)^n}} & \text{in momentum equation,} \\ \frac{U_i^{(3)^n} - U_{i-1}^{(3)^n}}{U_{i+1}^{(3)^n} - U_i^{(3)^n}} & \text{in energy equation} \end{cases} \tag{3.1.19a}$$

$$\text{and} \quad r_i^- = \frac{1}{r_i^+}. \tag{3.1.19b}$$

Step 2: Calculate all $\Phi(r^{\pm})$ values using a limiter satisfying TVD criteria (3.1.4).

Step 3: Take the $\boldsymbol{\Psi}$-moment of equation (3.1.5) treating $\Phi(r^{\pm})$ as constants.

This methodology yields an Euler level scheme of the form (3.1.13) with limiter values decided by the ratios (3.1.19).

3.1.3 Method 3

A slight deviation from **Method** 2 where $\Phi(r^{\pm})$ values are not entirely fixed by the conservative variables before taking moment, but they depend on local values of distribution functions as well, may improve the performance of the scheme. Let us write terms containing $\Phi(r^{\pm})$ in equation (3.1.5) as

$$\Phi(r_i^+)\left(F_{i+1}^n - F_i^n\right) = p_1 F_{i+1}^n + q_1 F_i^n + r_1 F_{i-1}^n \tag{3.1.20a}$$

$$\Phi(r_{i-1}^+)\left(F_i^n - F_{i-1}^n\right) = p_2 F_i^n + q_2 F_{i-1}^n + r_2 F_{i-2}^n \tag{3.1.20b}$$

$$\Phi(r_{i+1}^-)\left(F_{i+1}^n - F_i^n\right) = p_3 F_{i+2}^n + q_3 F_{i+1}^n + r_3 F_i^n \tag{3.1.20c}$$

$$\Phi(r_i^-)\left(F_i^n - F_{i-1}^n\right) = p_4 F_{i+1}^n + q_4 F_i^n + r_4 F_{i-1}^n \tag{3.1.20d}$$

where coefficients $p_1, q_1, r_1, p_2, q_2, r_2, p_3, q_3, r_3, p_4, q_4$ and r_4 are themselves functions of the ratio $r^{\pm}$ given by equation (3.1.3). For a chosen limiter function $\Phi(r^{\pm})$ equation (3.1.20) can give many solution sets for the coefficients p_1, q_1, r_1, etc., as a function of $r^{\pm}$. Now an Euler level scheme can be obtained by following the steps given below.

Step 1: Substitute the $\Phi(r_i^+)\left(F_{i+1}^n - F_i^n\right)$, $\Phi(r_i^-)\left(F_i^n - F_{i-1}^n\right)$, etc., terms in equation (3.1.5) by the coefficient form (3.1.20).

Step 2: Treating the coefficients as constants take the $\boldsymbol{\Psi}$-moment of (3.1.5). This gives the following Euler level scheme

$$\begin{aligned}\mathbf{U}_i^{n+1} = \mathbf{U}_i^n &- \lambda\left[(\mathbf{F}\mathbf{X}_i^{+^n} - \mathbf{F}\mathbf{X}_{i-1}^{+^n}) + (\mathbf{F}\mathbf{X}_{i+1}^{-^n} - \mathbf{F}\mathbf{X}_i^{-^n})\right] \\ &- \frac{\lambda}{2}\left[\left\{p_1\mathbf{F}\mathbf{X}_{i+1}^{+^n} + (q_1-p_2)\mathbf{F}\mathbf{X}_i^{+^n} + (r_1-q_2)\mathbf{F}\mathbf{X}_{i-1}^{+^n} - r_2\mathbf{F}\mathbf{X}_{i-2}^{+^n}\right\}\right. \\ &\left. - \left\{p_3\mathbf{F}\mathbf{X}_{i+2}^{-^n} + (q_3-p_4)\mathbf{F}\mathbf{X}_{i+1}^{-^n} + (r_3-q_4)\mathbf{F}\mathbf{X}_i^{-^n} - r_4\mathbf{F}\mathbf{X}_{i-1}^{-^n}\right\}\right] \\ &+ \frac{\lambda^2}{2}\left[\left\{p_1\mathbf{G}\mathbf{X}_{i+1}^{+^n} + (q_1-p_2)\mathbf{G}\mathbf{X}_i^{+^n} + (r_1-q_2)\mathbf{G}\mathbf{X}_{i-1}^{+^n} - r_2\mathbf{G}\mathbf{X}_{i-2}^{+^n}\right\}\right. \\ &\left. + \left\{p_3\mathbf{G}\mathbf{X}_{i+2}^{-^n} + (q_3-p_4)\mathbf{G}\mathbf{X}_{i+1}^{-^n} + (r_3-q_4)\mathbf{G}\mathbf{X}_i^{-^n} - r_4\mathbf{G}\mathbf{X}_{i-1}^{-^n}\right\}\right].\end{aligned} \tag{3.1.21}$$

Step 3: Calculate $r^{\pm}$ using the representative ratio given by (3.1.19). Select one set of coefficients out of many possible sets, as mentioned earlier, for a chosen limiter $\Phi(r_i^{\pm})$ and use the representative $r^{\pm}$ value to calculate the coefficient values. Each possible set of coefficients gives a different scheme. So the procedure gives a class of schemes. For example, the coefficients given by

$$\begin{array}{lll} p_1 = \Phi(r_i^+), & q_1 = -\Phi(r_i^+), & r_1 = 0; \\ p_2 = \Phi(r_{i-1}^+), & q_2 = -\Phi(r_{i-1}^+), & r_2 = 0; \\ p_3 = 0, & q_3 = \Phi(r_{i+1}^-), & r_3 = -\Phi(r_{i+1}^-); \\ p_4 = 0, & q_4 = \Phi(r_i^-), & r_4 = -\Phi(r_i^-) \end{array} \tag{3.1.22}$$

is one possible solution set out of many which satisfies equation (3.1.20), and this reproduces **Method** 2.

Numerical experiments show that all the schemes of the class of schemes (3.1.21) do not perform equally well. This suggests that some extra constraints in determining coefficients p_1, q_1, r_1, etc., using equation (3.1.20) is needed. If limiter function $\Phi(r^{\pm})$ is visualized as made up of infinitesimal linear segments at all $r^{\pm}$ values (which is always possible) then a unique set of coefficients p_1, q_1, r_1, etc., results satisfying (3.1.20). In other words, $\Phi(r^{\pm})$ in terms of p_1, q_1, r_1, etc., should give the equation of tangent to $\Phi(r^{\pm})$ at all $r^{\pm}$. This consideration puts two more constraints other than (3.1.20) in determining p_1, q_1, r_1, etc., which are described next.

(I) $\Phi(r^{\pm})$ should be representable in a linear function form of $r^{\pm}$ at all $r^{\pm}$:

Writing equation (3.1.20a) as

$$\begin{aligned}\Phi(r_i^+)\left(F_{i+1}^n - F_i^n\right) &= p_1(F_{i+1}^n - F_i^n) + (p_1+q_1)F_i^n + r_1F_{i-1}^n \\ &= p_1(F_{i+1}^n - F_i^n) - r_1(F_i^n - F_{i-1}^n) \quad (\text{taking} \quad p_1+q_1 = -r_1)\end{aligned}$$

gives

$$\Phi(r_i^+) = -r_1 r_i^+ + p_1 \quad \text{where} \quad p_1+q_1+r_1 = 0. \tag{3.1.23a}$$

Similarly,

$$\Phi(r_{i-1}^+) = -r_2 r_i^+ + p_2 \quad \text{where} \quad p_2+q_2+r_2 = 0, \tag{3.1.23b}$$

$$\Phi(r_{i+1}^-) = p_3 r_i^- - r_3 \quad \text{where} \quad p_3+q_3+r_3 = 0, \tag{3.1.23c}$$

and

$$\Phi(r_i^-) = p_4 r_i^- - r_4 \quad \text{where} \quad p_4+q_4+r_4 = 0, \tag{3.1.23d}$$

using equations (3.1.20b), (3.1.20c) and (3.1.20d), respectively.

(II) The slope of $\Phi(r^{\pm})$ should be equal to the slope of line segment representation given by (3.1.23a), (3.1.23b), (3.1.23c) and (3.1.23d) at all $r^{\pm}$, i.e.,

$$\frac{d\Phi(r_i^+)}{dr_i^+} = -r_1, \tag{3.1.24a}$$

$$\frac{d\Phi(r_{i-1}^+)}{dr_{i-1}^+} = -r_2, \tag{3.1.24b}$$

$$\frac{d\Phi(r_{i+1}^-)}{dr_{i+1}^-} = p_3 \tag{3.1.24c}$$

and

$$\frac{d\Phi(r_i^-)}{dr_i^-} = p_4. \tag{3.1.24d}$$

Thus equations (3.1.20), (3.1.23) and (3.1.24) determine coefficients p_1, q_1, r_1, etc., as a unique function of $r^{\pm}$ for scheme (3.1.21). As an example the coefficients for the minmod limiter ABKG shown in Figure 3.1(b) is given next. We have the minmod limiter

$$\Phi(r) = \begin{cases} 1, & r \geq 1 \\ r, & 0 \leq r < 1 \\ 0, & r < 0 \end{cases} \tag{3.1.25}$$

Use of this $\Phi(r)$ in equation (3.1.20) with constraints (3.1.23) and (3.1.24) yields

$$\begin{cases} p_1 = 1, q_1 = -1, r_1 = 0 & \text{for} \quad r_i^+ \geq 1 \\ p_1 = 0, q_1 = 1, r_1 = -1 & \text{for} \quad 0 \leq r_i^+ < 1 \\ p_1 = 0, q_1 = 0, r_1 = 0 & \text{for} \quad r_i^+ < 0 \end{cases} \quad \begin{cases} p_2 = 1, q_2 = -1, r_2 = 0 & \text{for} \quad r_{i-1}^+ \geq 1 \\ p_2 = 0, q_2 = 1, r_2 = -1 & \text{for} \quad 0 \leq r_{i-1}^+ < 1 \\ p_2 = 0, q_2 = 0, r_2 = 0 & \text{for} \quad r_{i-1}^+ < 0 \end{cases}$$

$$\begin{cases} p_3 = 0, q_3 = 1, r_3 = -1 & \text{for} \quad r_{i+1}^- \geq 1 \\ p_3 = 1, q_3 = -1, r_3 = 0 & \text{for} \quad 0 \leq r_{i+1}^- < 1 \\ p_3 = 0, q_3 = 0, r_3 = 0 & \text{for} \quad r_{i+1}^- < 0 \end{cases} \quad \begin{cases} p_4 = 0, q_4 = 1, r_4 = -1 & \text{for} \quad r_i^- \geq 1 \\ p_4 = 1, q_4 = -1, r_4 = 0 & \text{for} \quad 0 \leq r_i^- < 1 \\ p_4 = 0, q_4 = 0, r_4 = 0 & \text{for} \quad r_i^- < 0 \end{cases}$$

This set of coefficients incorporates minmod limiter in scheme (3.1.21). As another example Van Leer limiter ABKH in Figure 3.1(b) is

$$\Phi(r) = \begin{cases} \frac{2r}{1+r}, & r \geq 0 \\ 0, & r < 0 \end{cases} \tag{3.1.26}$$

Use of this $\Phi(r)$ in equation (3.1.20) with constraints (3.1.23) and (3.1.24) yields

$$\begin{cases} p_1 = \frac{2{r_i^+}^2}{\left(1+r_i^+\right)^2}, q_1 = \frac{-2\left(r_i^+-1\right)}{\left(r_i^++1\right)}, r_1 = \frac{-2}{\left(1+r_i^+\right)^2} & \text{for} \quad r_i^+ \geq 0 \\ p_1 = 0, q_1 = 0, r_1 = 0 & \text{for} \quad r_i^+ < 0 \end{cases}$$

$$\begin{cases} p_2 = \frac{2{r_{i-1}^+}^2}{\left(1+r_{i-1}^+\right)^2}, q_2 = \frac{-2\left(r_{i-1}^+-1\right)}{\left(r_{i-1}^++1\right)}, r_2 = \frac{-2}{\left(1+r_{i-1}^+\right)^2} & \text{for} \quad r_{i-1}^+ \geq 0 \\ p_2 = 0, q_2 = 0, r_2 = 0 & \text{for} \quad r_{i-1}^+ < 0 \end{cases}$$

$$\begin{cases} p_3 = \frac{2}{\left(1+r_{i+1}^-\right)^2}, q_3 = \frac{2\left(r_{i+1}^--1\right)}{\left(r_{i+1}^-+1\right)}, r_3 = \frac{-2{r_{i+1}^-}^2}{\left(1+r_{i+1}^-\right)^2} & \text{for} \quad r_{i+1}^- \geq 0 \\ p_3 = 0, q_3 = 0, r_3 = 0 & \text{for} \quad r_{i+1}^- < 0 \end{cases}$$

$$\begin{cases} p_4 = \frac{2}{\left(1+r_i^-\right)^2}, q_4 = \frac{2\left(r_i^--1\right)}{\left(r_i^-+1\right)}, r_4 = \frac{-2{r_i^-}^2}{\left(1+r_i^-\right)^2} & \text{for} \quad r_i^- \geq 0 \\ p_4 = 0, q_4 = 0, r_4 = 0 & \text{for} \quad r_i^- < 0 \end{cases}$$

This coefficient set incorporates Van Leer limiter in scheme (3.1.21).

All the three methods work equally well for all tests carried out except for two, namely, Einfeldt et. al. [56] test involving strong rarefaction wave and Woodward-Colella blast wave test [57]. **Method** 2 fails in Einfeldt test. **Method** 3 gives negative pressure and density

in Woodward-Colella test when Van Leer or superbee limiters are used; however, it works for minmod and other less compressive limiters. Thus these two methods need further improvement. **Method** 1 works for all tests without any difficulty, so its robustness is evident. Thus from now onwards all discussions will be around **Method** 1 and the term "FLKS scheme" in the rest of the thesis will refer to this method only.

3.2 Relaxing TVD Criterion in FLKS Scheme

The FLKS scheme (3.1.12) contains anti-dissipation terms, not present in KFVS scheme, to reduce and regulate dissipation. Flux-limiting procedure [26] which has been used at the Boltzmann level regulates artificial viscosity by combining a first-order scheme (CIR) which has high artificial viscosity and a second-order scheme (Lax-Wendroff) which has low viscosity, using a local data dependent limiter function Φ. This Φ satisfies the TVD condition (3.1.4) to avoid spurious wiggles. The superbee limiter ABCKEF in Figure 3.1(b) is known to be the least dissipative in the second order shaded zone. If dissipation is needed to be reduced further, then TVD criterion may get violated. One simple way to relax the condition (3.1.4) is to use a less dissipative scheme in place of Lax-Wendroff scheme at the Boltzmann level while using the same unmodified TVD criterion. Small amount of relaxation may allow some less significant spurious wiggles at high gradient regions, however, the discontinuities like shocks, contacts, etc., in the flow-field is expected to be captured well.

A scheme in conservation form for the linear advection equation

$$\frac{\partial u}{\partial t} + \frac{\partial f(u)}{\partial x} = 0; \quad f(u) = au \quad (a\text{=constant}) \tag{3.2.1}$$

where u is a conserved variable which gets advected at wave speed a, is given by

$$u_i^{n+1} = u_i^n - \lambda \left[\hat{f}^n_{i+\frac{1}{2}} - \hat{f}^n_{i-\frac{1}{2}} \right], \tag{3.2.2a}$$

where

$$\hat{f}^n_{i+\frac{1}{2}} = \frac{1}{2} a (u_i^n + u_{i+1}^n) - \frac{1}{2} \varepsilon^n_{i+\frac{1}{2}} (u_{i+1}^n - u_i^n) \tag{3.2.2b}$$

is the time averaged flux at the face $x_{i+\frac{1}{2}}$ at the i^{th} cell $\left[x_{i-\frac{1}{2}}, x_{i+\frac{1}{2}} \right]$. Here $\hat{f}^n_{i+\frac{1}{2}}$ has been written in "artificial viscosity" form [53] with coefficient of artificial viscosity $\varepsilon^n_{i+\frac{1}{2}}$. The Lax-Wendroff scheme for (3.2.1) has $\varepsilon^n_{i+\frac{1}{2}} = \lambda a^2$. It is known that Lax-Wendroff scheme has the minimum artificial viscosity satisfying linear stability [53]. However, if the artificial viscosity coefficient

$\varepsilon^n_{i+\frac{1}{2}} = \lambda a^2$ is still modified by multiplying with a constant, say b (≤ 1), then linear stability is violated, but a less dissipative scheme than Lax-Wendroff results with $\varepsilon^n_{i+\frac{1}{2}} = b\lambda a^2$. Considering the collisionless Boltzmann equation (2.2.1) as a linear advection equation, the modified less dissipative Lax-Wendroff type scheme for (2.2.1) is given by

$$F_i^{n+1} = F_i^n - \lambda \left[\hat{f}^n_{i+\frac{1}{2}} - \hat{f}^n_{i-\frac{1}{2}} \right] \tag{3.2.3a}$$

where

$$\hat{f}^n_{i+\frac{1}{2}} = \frac{1}{2} v_1 (F_i^n + F_{i+1}^n) - \frac{1}{2} \varepsilon^n_{i+\frac{1}{2}} (F^n_{i+1} - F^n_i) \tag{3.2.3b}$$

with

$$\varepsilon^n_{i+\frac{1}{2}} = b\lambda v_1^2 \quad (b \leq 1) \tag{3.2.3c}$$

If this scheme (3.2.3) is used in place of original Lax-Wendroff scheme in deriving Boltzmann level scheme (3.1.5); only the term $\frac{\lambda^2}{2}$ needs to be replaced with $b\frac{\lambda^2}{2}$. If the TVD criterion (3.1.4) is not modified then TVD condition gets relaxed more and more as b is assigned values below 1 gradually. The $\boldsymbol{\Psi}$-moment of this modified Boltzmann level scheme gives the Euler level scheme

$$\mathbf{U}_i^{n+1} = \mathbf{U}_i^n - \lambda \left[\hat{\mathbf{f}}^n_{i+\frac{1}{2}} - \hat{\mathbf{f}}^n_{i-\frac{1}{2}} \right] \tag{3.2.4a}$$

where

$$\begin{aligned} \hat{\mathbf{f}}^n_{i+\frac{1}{2}} &= \left(\mathbf{F}\mathbf{X}_i^{+^n} + \mathbf{F}\mathbf{X}_{i+1}^{-_n}\right) \\ &+ \frac{1}{2}\text{avg}\left(\left(\mathbf{F}\mathbf{X}_{i+1}^{+^n} - \mathbf{F}\mathbf{X}_i^{+^n}\right), \left(\mathbf{F}\mathbf{X}_i^{+^n} - \mathbf{F}\mathbf{X}_{i-1}^{+^n}\right)\right) \\ &- \frac{1}{2}\text{avg}\left(\left(\mathbf{F}\mathbf{X}_{i+2}^{-_n} - \mathbf{F}\mathbf{X}_{i+1}^{-_n}\right), \left(\mathbf{F}\mathbf{X}_{i+1}^{-_n} - \mathbf{F}\mathbf{X}_i^{-_n}\right)\right) \\ &- b\frac{\lambda}{2}\text{avg}\left(\left(\mathbf{G}\mathbf{X}_{i+1}^{+^n} - \mathbf{G}\mathbf{X}_i^{+^n}\right), \left(\mathbf{G}\mathbf{X}_i^{+^n} - \mathbf{G}\mathbf{X}_{i-1}^{+^n}\right)\right) \\ &- b\frac{\lambda}{2}\text{avg}\left(\left(\mathbf{G}\mathbf{X}_{i+2}^{-_n} - \mathbf{G}\mathbf{X}_{i+1}^{-_n}\right), \left(\mathbf{G}\mathbf{X}_{i+1}^{-_n} - \mathbf{G}\mathbf{X}_i^{-_n}\right)\right); \quad b \leq 1. \end{aligned} \tag{3.2.4b}$$

Use of any limiter function $\Phi(r)$ with b less than 1 will give crisper shocks, contacts, etc. But taking a value of b far below 1 will give large spurious oscillations and the scheme may fail due to instability. So b is a handy parameter and should be chosen on trial and error basis depending on the situation. The empiricism introduced by the parameter b can be removed by making it data dependent using some nonlinear stability analysis. But this has not been attempted in this thesis. In all the tests performed by us a value of b around 0.5 always works without any significant spurious oscillations.

3.3 Use of Extremum-Preserving Limiter in FLKS Scheme

It is well-known that use of a TVD criterion results in clipping the extrema. This problem is extensively addressed in literature [58–60]. The remedy suggested is the use of more relaxed stability criteria than TVD (e.g., TVB, ENO). Section 3.2 gave one simple but blunt way to relax TVD criterion. This does reduce clipping error as the numerical experiments show, but a more sophisticated and reliable way is needed. Sekora-Colella [61, 62] have formulated extremum-preserving limiters for MUSCL and PPM. They suggest that these limiters fit into any scheme which uses conventional limiting procedure. The new extremum-preserving limiter for MUSCL has been adapted for use in FLKS scheme.

Van Leer introduced the so called MUSCL approach [18, 19]. As far as linear advection is concerned there is no difference between the flux-limited approach of Sweby and the slope-limited approach in MUSCL [5, 63]. The MUSCL approach gives the slope-limited scheme for the linear advection equation (3.2.1) in conservation form (3.2.2a) with

$$\hat{f}^n_{i+\frac{1}{2}} = \begin{cases} au^n_i + \frac{1}{2}a(1-\lambda a)S_i\Delta x, & a \geq 0 \\ au^n_{i+1} - \frac{1}{2}a(1+\lambda a)S_{i+1}\Delta x, & a < 0 \end{cases} \tag{3.3.1}$$

where slope S is the limited-slope and satisfies some TVD criterion. The flux-limited approach of Sweby gives the same conservative flux $\hat{f}^n_{i+\frac{1}{2}}$ as

$$\hat{f}^n_{i+\frac{1}{2}} = \begin{cases} au^n_i + \frac{1}{2}a(1-\lambda a)\Phi(r^+_i)(u_{i+1} - u^n_i), & a \geq 0 \\ au^n_{i+1} - \frac{1}{2}a(1+\lambda a)\Phi(r^-_{i+1})(u^n_{i+1} - u^n_i), & a < 0 \end{cases} \tag{3.3.2}$$

where $\Phi(r^{\pm})$ is the flux-limiter with

$$r^+_i = \frac{u^n_i - u^n_{i-1}}{u^n_{i+1} - u^n_i} \tag{3.3.3a}$$

$$\text{and} \quad r^-_i = \frac{u^n_{i+1} - u^n_i}{u^n_i - u^n_{i-1}}. \tag{3.3.3b}$$

The equation (3.3.2) was used to obtain the Boltzmann level flux-limited formula (3.1.1). Now comparing equations (3.3.1) and (3.3.2), we get

$$S_i = \begin{cases} \Phi(r^+_i)\left(\frac{u^n_{i+1} - u^n_i}{\Delta x}\right), & a \geq 0 \\ \Phi(r^-_i)\left(\frac{u^n_i - u^n_{i-1}}{\Delta x}\right), & a < 0 \end{cases} \tag{3.3.4}$$

This equation clearly demonstrates that the flux-limiters $\Phi(r^{\pm})$ which are thought as limiting amount of flux contribution in flux-averaging of two fluxes (a first-order and a second-order flux) in Sweby's method (3.3.2), are actually limiting the slopes $\frac{u_{i+1}^n - u_i^n}{\Delta x}$ and $\frac{u_i^n - u_{i-1}^n}{\Delta x}$ of the linear reconstruction in the i^{th} cell $\left[x_{i-\frac{1}{2}}, x_{i+\frac{1}{2}}\right]$ in the reconstruction phase of MUSCL procedure. Thus a limited slope S can be obtained from a given flux-limiter $\Phi(r^{\pm})$ using (3.3.4) and vice versa. Equation (3.3.4) can be written as

$$\Delta u_i = \begin{cases} \Phi(r_i^+)\left(u_{i+1}^n - u_i^n\right), & a \geq 0 \\ \Phi(r_i^-)\left(u_i^n - u_{i-1}^n\right), & a < 0 \end{cases} \tag{3.3.5}$$

where

$$\Delta u_i = S_i \Delta x. \tag{3.3.6}$$

Van Leer [18] gives the slope-limited version of Van Leer limiter in terms of Δu_i as

$$\Delta u_i = \begin{cases} \frac{2\Delta_+ u_i \Delta_- u_i}{\Delta_+ u_i + \Delta_- u_i}, & \Delta_+ u_i \Delta_- u_i > 0 \\ 0, & \text{otherwise} \end{cases} \tag{3.3.7}$$

where

$$\Delta_+ u_i = u_{i+1}^n - u_i^n \tag{3.3.8a}$$

and

$$\Delta_- u_i = u_i^n - u_{i-1}^n. \tag{3.3.8b}$$

The same paper mentions another version of Van Leer limiter (which is more compressive than (3.3.7)) as

$$\Delta u_i = \begin{cases} \text{sign}\left(\Delta_c u_i\right) \min\left(|\Delta_c u_i|, |\Delta_{\text{lim}} u_i|\right), & \Delta_+ u_i \Delta_- u_i > 0 \\ 0, & \text{otherwise} \end{cases} \tag{3.3.9}$$

where

$$\Delta_{\text{lim}} u_i = 2\text{min}\left(|\Delta_- u_i|, |\Delta_+ u_i|\right), \tag{3.3.10a}$$

$$\Delta_c u_i = \frac{1}{2}(u_{i+1}^n - u_{i-1}^n). \tag{3.3.10b}$$

This limiter, which we call the "second type Van Leer limiter", can be reorganized in a flux-limiter format using (3.3.5) to obtain $\Phi(r^{\pm})$, which can then be used in FLKS scheme (3.1.13) with ratios (3.1.15) defined using split fluxes $FX^{\pm}$ and $GX^{\pm}$. Alternatively, we can replace

term $\Phi\left(R_i^{(k)^+}\right)\left(FX_{i+1}^{(k)^{+^n}} - FX_i^{(k)^{+^n}}\right)$ in equation (3.1.13) by

$$\Delta FX_i^{(k)^+} = \begin{cases} \text{sign}\left(\Delta_c FX_i^{(k)^+}\right) \min\left(\left|\Delta_c FX_i^{(k)^+}\right|, \left|\Delta_{\lim} FX_i^{(k)^+}\right|\right), & \Delta_+ FX_i^{(k)^+} \Delta_- FX_i^{(k)^+} > 0 \\ 0, & \text{otherwise} \end{cases} \tag{3.3.11}$$

which is of the form given in equation (3.3.9) where $FX^{(k)^+}$ is used in place of u where

$$\Delta_+ FX_i^{(k)^+} = FX_{i+1}^{(k)^{+^n}} - FX_i^{(k)^{+^n}}, \tag{3.3.12a}$$

$$\Delta_- FX_i^{(k)^+} = FX_i^{(k)^{+^n}} - FX_{i-1}^{(k)^{+^n}}, \tag{3.3.12b}$$

$$\Delta_c FX_i^{(k)^+} = \frac{1}{2}\left(FX_{i+1}^{(k)^{+^n}} - FX_{i-1}^{(k)^{+^n}}\right), \tag{3.3.12c}$$

$$\Delta_{\lim} FX_i^{(k)^+} = 2\min\left(\left|\Delta_- FX_i^{(k)^+}\right|, \left|\Delta_+ FX_i^{(k)^+}\right|\right), \tag{3.3.12d}$$

and similarly we replace the term $\Phi\left(R_{i-1}^{(k)^+}\right)\left(FX_i^{(k)^{+^n}} - FX_{i-1}^{(k)^{+^n}}\right)$ by $\Delta FX_{i-1}^{(k)^+}$, the term $\Phi\left(S_{i+1}^{(k)^-}\right)\left(FX_{i+1}^{(k)^{-^n}} - FX_i^{(k)^{-^n}}\right)$ by

$$\Delta FX_{i+1}^{(k)^-} = \begin{cases} \text{sign}\left(\Delta_c FX_{i+1}^{(k)^-}\right) \min\left(\left|\Delta_c FX_{i+1}^{(k)^-}\right|, \left|\Delta_{\lim} FX_{i+1}^{(k)^-}\right|\right), & \Delta_+ FX_{i+1}^{(k)^-} \Delta_- FX_{i+1}^{(k)^-} > 0 \\ 0, & \text{otherwise} \end{cases} \tag{3.3.13}$$

where

$$\Delta_+ FX_{i+1}^{(k)^-} = FX_{i+2}^{(k)^{-^n}} - FX_{i+1}^{(k)^{-^n}}, \tag{3.3.14a}$$

$$\Delta_- FX_{i+1}^{(k)^-} = FX_{i+1}^{(k)^{-^n}} - FX_i^{(k)^{-^n}}, \tag{3.3.14b}$$

$$\Delta_c FX_{i+1}^{(k)^-} = \frac{1}{2}\left(FX_{i+2}^{(k)^{-^n}} - FX_i^{(k)^{-^n}}\right), \tag{3.3.14c}$$

$$\Delta_{\lim} FX_{i+1}^{(k)^-} = 2\min\left(\left|\Delta_- FX_{i+1}^{(k)^-}\right|, \left|\Delta_+ FX_{i+1}^{(k)^-}\right|\right), \tag{3.3.14d}$$

and so on for all such terms containing Φ. This way the Van Leer limiter (3.3.9) gets adapted for use in FLKS scheme (3.1.13).

Sekora-Colella [61] describes the following steps to get the extremum-preserving version of limiter (3.3.9):

Step 1: Calculate the following quantities:

$$\Delta_{--}u_i = u_{i-1}^n - u_{i-2}^n \tag{3.3.15a}$$

$$\Delta_{-}u_i = u_{i}^n - u_{i-1}^n \tag{3.3.15b}$$

$$\Delta_{c}u_i = \frac{1}{2}(u_{i+1}^n - u_{i-1}^n) \tag{3.3.15c}$$

$$\Delta_{+}u_i = u_{i+1}^n - u_{i}^n \tag{3.3.15d}$$

$$\Delta_{++}u_i = u_{i+2}^n - u_{i+1}^n \tag{3.3.15e}$$

Step 2: Define extremum if the following condition is satisfied:

$$\min(\Delta_{-}u_i\Delta_{+}u_i, \Delta_{--}u_i\Delta_{++}u_i) < 0 \tag{3.3.16}$$

Step 3: If condition (3.3.16) is not satisfied, use the original Van Leer limiter

$$\Delta u_i = \text{sign}\left(\Delta_c u_i\right) \min\left(|\Delta_c u_i|, |\Delta_{\text{lim}} u_i|\right), \tag{3.3.17}$$

where

$$\Delta_{\text{lim}} u_i = 2\text{min}\left(|\Delta_{-} u_i|, |\Delta_{+} u_i|\right).$$

Step 4: If condition (3.3.16) is satisfied then compute the following 2^{nd} derivatives:

$$D_{-}^2 u_i = \frac{1}{(\Delta x)^2}\left(u_i^n - 2u_{i-1}^n + u_{i-2}^n\right) \tag{3.3.18a}$$

$$D_{c}^2 u_i = \frac{1}{(\Delta x)^2}\left(u_{i+1}^n - 2u_{i}^n + u_{i-1}^n\right) \tag{3.3.18b}$$

$$D_{+}^2 u_i = \frac{1}{(\Delta x)^2}\left(u_{i+2}^n - 2u_{i+1}^n + u_{i}^n\right) \tag{3.3.18c}$$

Step 5: Find the minimum 2^{nd} derivative as

$$D_{\text{lim}}^2 u_i = \min\left(\left|D_c^2 u_i\right|, \max\left(\text{sign}\left(D_c^2 u_i\right) D_{-}^2 u_i, 0\right), \max\left(\text{sign}\left(D_c^2 u_i\right) D_{+}^2 u_i, 0\right)\right) \tag{3.3.19}$$

Step 6: Apply the modified extremum-preserving Van Leer limiter at the extremum:

$$\Delta u_i = \text{sign}(\Delta_c u_i)\text{min}\left(|\Delta_c u_i|, |\Delta_{\text{lim}} u_i|\right), \tag{3.3.20}$$

where

$$\Delta_{\lim} u_i = \begin{cases} \min\left(2|\Delta_- u_i|, C_{VL}\frac{3(\Delta x)^2}{2} D^2_{\lim} u_i\right), & \text{sign}\left(D^2_c u_i\right)\Delta_c u_i < 0 \\ \min\left(2|\Delta_+ u_i|, C_{VL}\frac{3(\Delta x)^2}{2} D^2_{\lim} u_i\right), & \text{otherwise.} \end{cases} \tag{3.3.21}$$

Here C_{VL} is a constant and as $C_{VL} \to 0$, the extremum-preserving limiter approaches the original Van Leer limiter.

This extremum-preserving limiter is adapted in the FLKS scheme (3.1.13) in a similar fashion as is done to adapt the second type Van Leer limiter (3.3.9). The terms like $\Phi\left(R_i^{(k)^+}\right)\left(FX_{i+1}^{(k)^{+^n}} - FX_i^{(k)^{+^n}}\right)$ etc., containing Φ in equation (3.1.13) are replaced by $\Delta FX_i^{(k)^+}$ etc., and then $\Delta_{--}FX^{(k)^+}, \Delta_- FX^{(k)^+}$, $\Delta_c FX^{(k)^+}$, etc., are calculated using the split fluxes similar to calculating $\Delta_{--}u, \Delta_- u, \Delta_c u$, etc., following Step 1 to Step 6 above.

3.4 Results and Discussion

This section includes several test problems to evaluate the performance of the FLKS scheme. For time evolution a global time step Δt is determined first for time integration. This Δt depends on a CFL value chosen. We use

$$\Delta t = \text{CFL} \times \frac{\Delta x}{\max\limits_i \left(|u_i| + a_i\right)}, \tag{3.4.1}$$

where u is fluid velocity, a is sonic speed and i is the cell index. In the tables and figures to follow, FLKSmm, FLKSvl and FLKSsb stand for FLKS scheme with minmod, Van Leer and superbee limiters, respectively, with $b = 1.0$. When showing results for $b < 1.0$, explicit mention of the b value is done.

First, accuracy analysis is performed to show the order of convergence of the scheme using a test problem which has smooth solution, and then other test problems have been solved and compared with the exact solution to judge the accuracy and robustness of the scheme. In all the tests, the physical quantities are in SI units, however, the units are not mentioned explicitly.

3.4.1 Accuracy test

An exact periodic solution for 1D Euler equations is used as given in [64]:

$$\rho(x,t) = 1.0 + 0.2\sin(\pi(x - ut)), \quad u(x,t) = 0.1, \quad p(x,t) = 0.5. \tag{3.4.2}$$

A computational domain $[-1, 1]$ is taken and the computation stops at $t = 0.5$. The grid is refined successively and error norm for density is calculated. Table 3.1 shows the L_1- and L_∞-norm-based orders for CFL values of 0.5, 0.2 and 0.01 when minmod limiter is used with FLKS scheme. It is clear that as the CFL number is reduced the order of accuracy improves. This trend is somewhat similar to the observation made in [65, 66]. For a CFL number of 0.01, close to second order convergence in L_1 error norm is achieved. L_∞ order is consistently very low and little above 1.0. This low value can probably be attributed to the low order of reduction of clipping errors due to limiting at extrema. Table 3.2 shows the L_1- and L_∞-norm-based orders for CFL value

Table 3.1 Order of accuracy of FLKS scheme with minmod limiter for 1D case. L_1 and L_∞ error norms for density are used for order calculation.

Scheme	Number of cells	L_1 error	L_1 order	L_∞ error	L_∞ order
FLKSmm, CFL= 0.5	20	0.004011		0.011836	
	40	0.001667	1.27	0.005383	1.14
	80	0.000801	1.06	0.002659	1.02
	160	0.000372	1.11	0.001255	1.08
	320	0.000184	1.02	0.000600	1.06
	640	0.000094	0.97	0.000288	1.06
	1280	0.000045	1.06	0.000138	1.06
FLKSmm, CFL= 0.2	20	0.003059		0.010213	
	40	0.001071	1.51	0.004870	1.07
	80	0.000394	1.44	0.002245	1.12
	160	0.000164	1.26	0.000995	1.17
	320	0.000084	0.97	0.000439	1.18
	640	0.000039	1.11	0.000193	1.19
	1280	0.000018	1.12	0.000085	1.18
FLKSmm, CFL= 0.01	20	0.003800		0.009909	
	40	0.001309	1.54	0.004731	1.07
	80	0.000372	1.82	0.002113	1.16
	160	0.000098	1.92	0.000904	1.22
	320	0.000025	1.97	0.000378	1.26
	640	0.000006	2.06	0.000156	1.28
	1280	0.000002	1.58	0.000064	1.29

of 0.01 when FLKS scheme uses second type Van Leer limiter (FLKSvl2) and its extremum-preserving version (FLKSext-pre). The L_1- and L_∞-errors for the extremum-preserving version of limiter is always lower for all grid resolutions. The order using extremum-preserving limiter for coarse grids is close to 2.0, but for finer grids the order reduces and comes close to 1.0. This suggests that the local correction made for extrema capturing does not necessarily improve the order of accuracy of the full scheme, however, the accuracy measured in L_1- and L_∞-norm are always better, particularly due to reduced clipping at extrema.

Table 3.2 Order of accuracy of FLKS scheme with second type Van Leer limiter and extremum-preserving limiter for 1D case. L_1 and L_∞ error norms for density are used for order calculation.

Scheme	Number of cells	L_1 error	L_1 order	L_∞ error	L_∞ order
FLKSvl2, CFL= 0.01	20	0.000523764		0.003532233	
	40	0.000185556	1.50	0.001394115	1.34
	80	0.000046705	1.99	0.000489105	1.51
	160	0.000013734	1.77	0.000174996	1.48
	320	0.000005236	1.39	0.000061348	1.51
	640	0.000002103	1.32	0.000021550	1.51
	1280	0.000001078	0.96	0.000007731	1.48
FLKSext-pre, CFL= 0.01	20	0.000330909		0.001358641	
	40	0.000074986	2.14	0.000214040	2.67
	80	0.000020837	1.84	0.000057753	1.89
	160	0.000008331	1.32	0.000022353	1.37
	320	0.000004090	1.02	0.000010391	1.11
	640	0.000001906	1.10	0.000004991	1.06
	1280	0.000001030	0.89	0.000003392	0.56

3.4.2 1D Riemann problems

Here three Riemann problems are considered. The first one is the well-known Sod's shock tube problem [67]. The initial condition for this problem is

$$(\rho, p, u) = \begin{cases} (1.0, 100000.0, 0), & -10 \leq x < 0 \\ (0.125, 10000.0, 0), & 0 \leq x < 10 \end{cases} \tag{3.4.3}$$

The calculation stops at a time of 0.01. Figure 3.2 shows the schematic of the setup. The tube in the setup contains two chambers separated by a diaphragm. The left chamber (Driver section) contains high pressure and high density gas whereas the right chamber (Driven section) has relatively low pressure and density. When the diaphragm is ruptured, this setup results in a normal shock moving to the right, a contact discontinuity following it, and an expansion fan moving to the left. This problem is modelled as a 1D problem and solved. The stopping time is chosen such that the calculation stops before the shock or the expansion head reaches the boundary of the computational domain. A CFL number of 0.25 has been used, but FLKS also works for higher CFL numbers close to 1 without difficulty. Figures 3.3(a), 3.3(b), 3.3(c) and 3.3(d), respectively, show the plots of pressure, density, velocity and internal energy obtained with 501 grid points using FLKS scheme with Van Leer limiter. There are no visible spurious

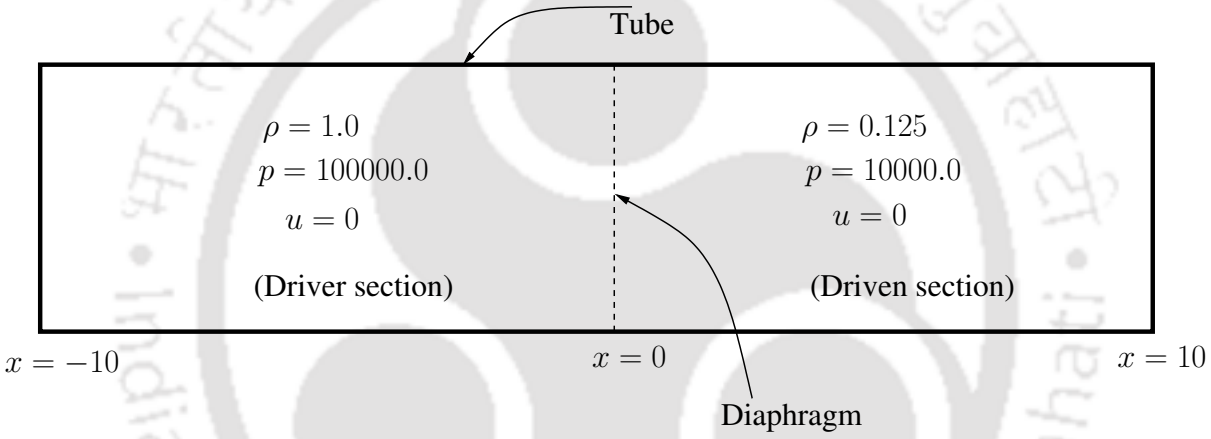

Figure 3.2. Shock tube

oscillations. If a more compressive limiter like superbee is used in place of Van Leer limiter then small spurious wiggles appear near the expansion fan corner and the contact discontinuity corner, as can be seen in Figure 3.4. It seems that as the grid is refined, undershoots around the rarefaction and contact are getting bigger and FLKS with superbee limiter is not convergent, but as explained next this is not the case. Figure 3.4 compares the density plot obtained for Sod's shock tube problem using $31, 51$ and 101 grid points. Figure 3.4(b) shows a zoomed view of the rarefaction tail corner and Figure 3.4(c) shows a zoomed view of the contact discontinuity corner. It can be seen that as the grid is refined from 31 points to 51 points and then to 101 points, the spurious oscillations gradually become visible. The coarse grids of 31 and 51 points are not sufficient to resolve the small spurious oscillations when superbee limiter is used with FLKS scheme. However, once the oscillations become visible at a sufficient resolution using 101

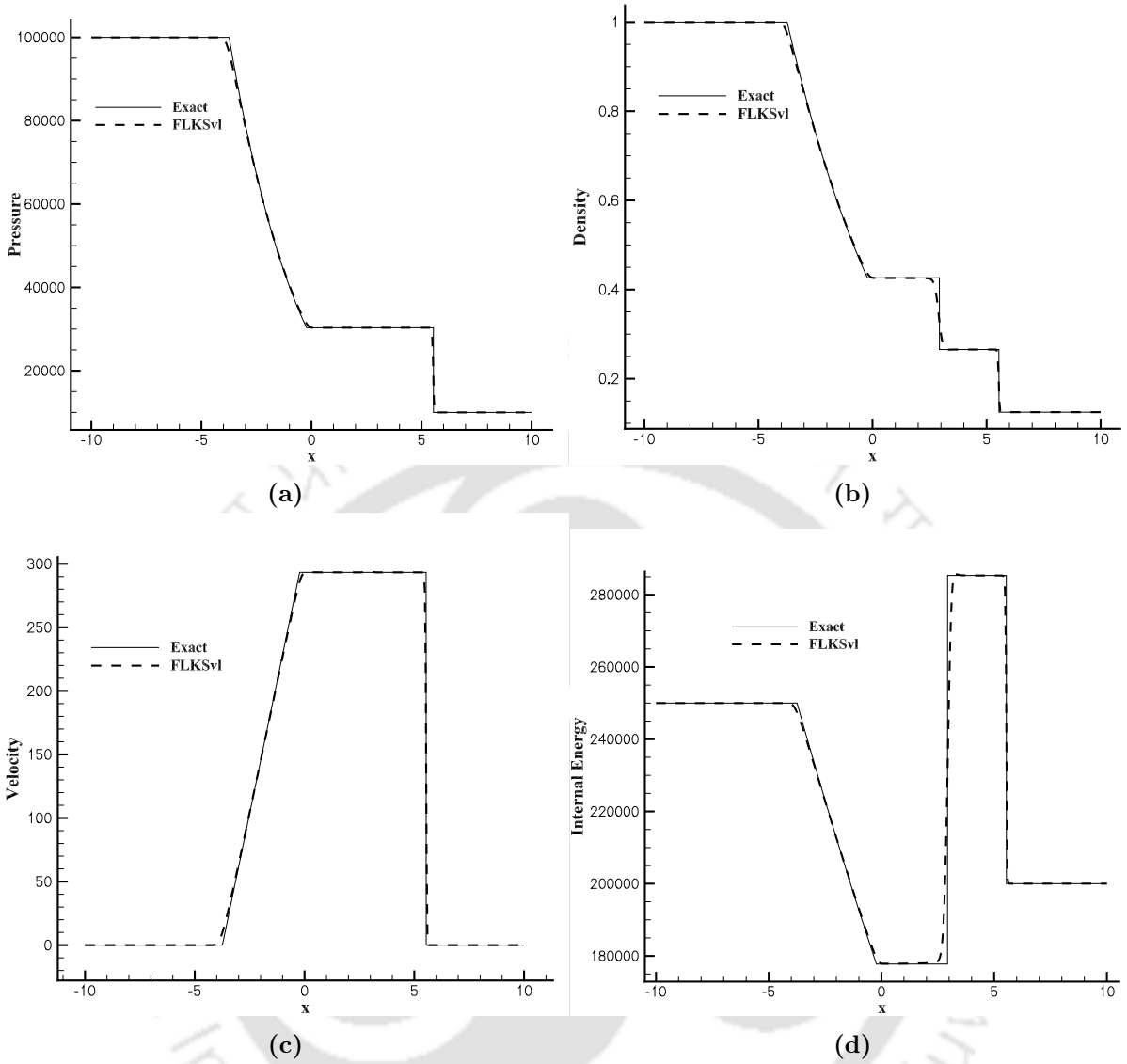

Figure 3.3. Sod's shock tube problem. Plots for (a) pressure, (b) density, (c) velocity and (d) internal energy obtained with 501 grid points. The calculation stops at a time of 0.01.

grid points, further refinement of grid does not increase the size of oscillations. Figure 3.5(b) and 3.5(c) show the magnified view of the rarefaction and contact corners, respectively, when $301, 501$ and 701 grid points are used. Clearly, as the grid is refined the size of oscillations reduce and therefore, FLKS with superbee limiter is convergent as well.

The second Riemann problem considered is also a Sod's shock tube type problem with a different initial condition given in the work of Laney [53] as

$$(\rho, p, u) = \begin{cases} (1.0, 100000.0, 0), & -10 \leq x < 0 \\ (0.01, 1000.0, 0), & 0 \leq x < 15 \end{cases} \tag{3.4.4}$$

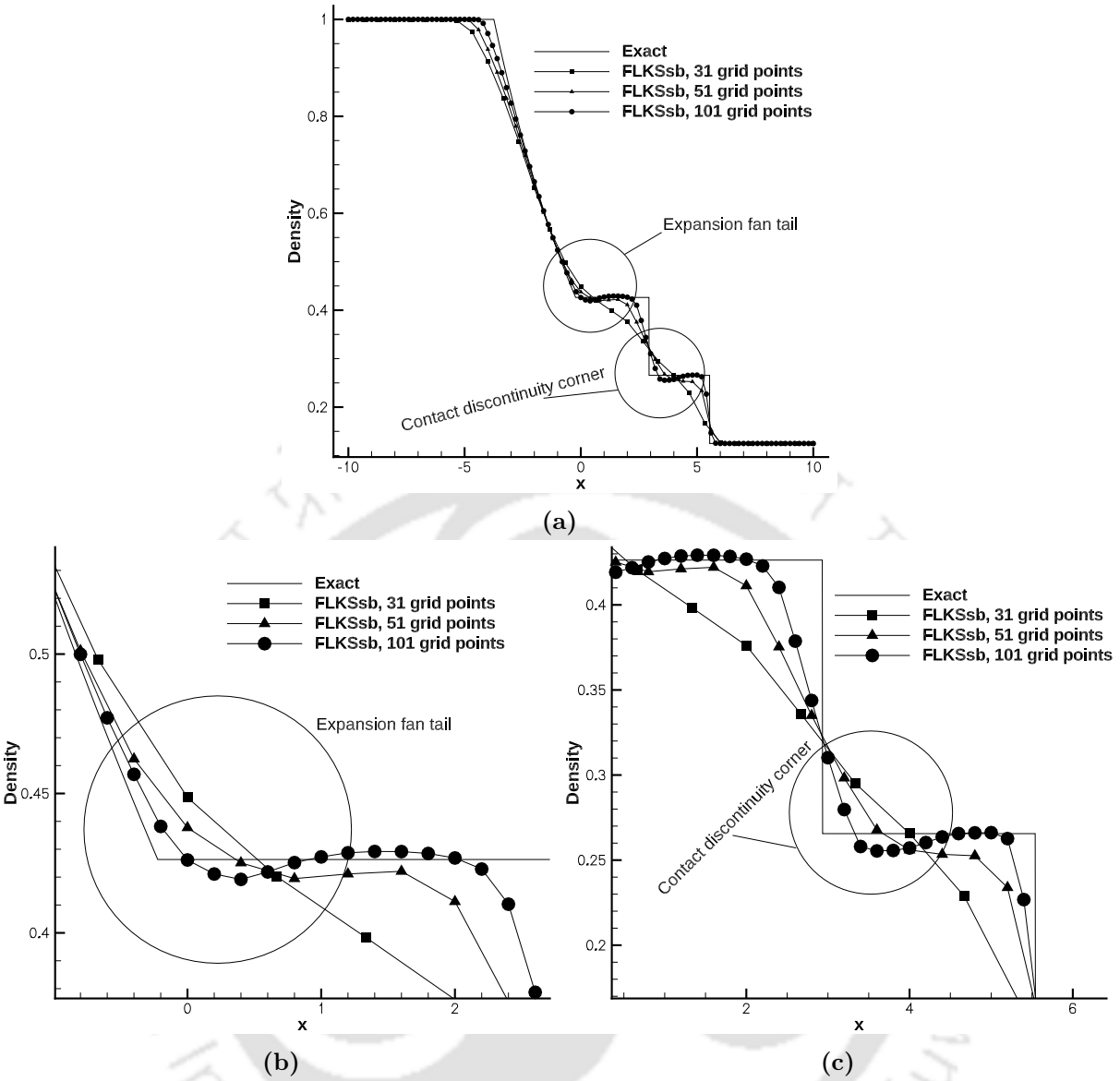

Figure 3.4. Sod shock tube problem. (a) Density plot obtained using 31, 51 and 101 grid points. (b) Magnified view of the rarefaction tail corner of (a). (c) Magnified view of the contact discontinuity corner of (a).

and the calculation stops at a time of 0.01. This initial condition results in a expansive sonic point at $x = 0$ in the expansion fan region. At such sonic points many schemes cause expansion shocks to appear which are nonphysical and an indication of violation of the second law of thermodynamics. Roe's approximate Riemann solver [22] is one such scheme. Figure 3.6(a) shows a comparison of Roe's scheme with FLKS scheme. The FLKS scheme does not give an expansion shock and hence suggesting entropy condition satisfaction.

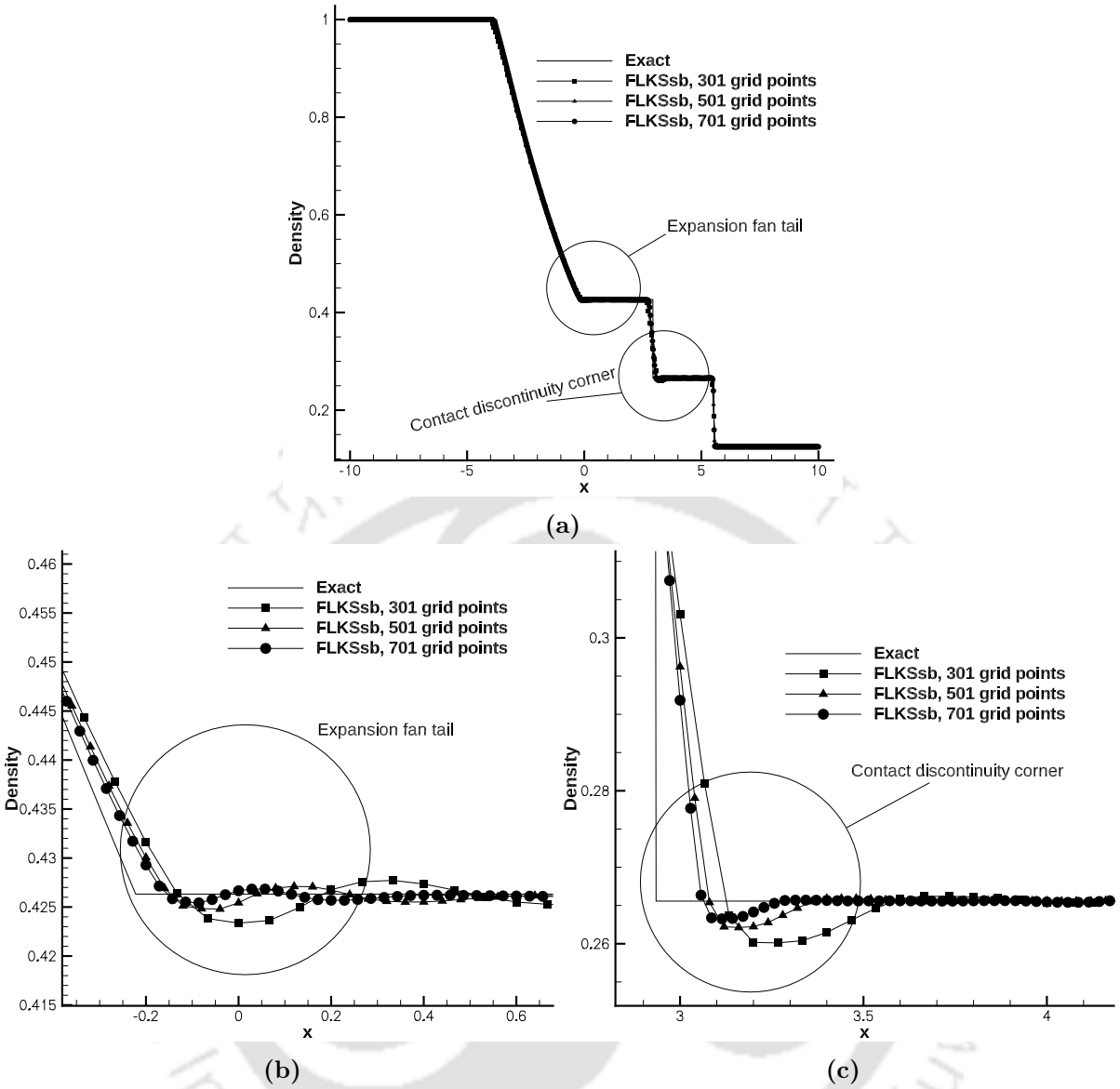

Figure 3.5. Sod shock tube problem. (a) Density plot obtained using $301, 501$ and 701 grid points. (b) Magnified view of the rarefaction tail corner of (a). (c) Magnified view of the contact discontinuity corner of (a).

The third Riemann problem considered is the Einfeldt et. al. test [56]. The initial condition is

$$(\rho, p, u) = \begin{cases} (1.0, 0.4, -2.0), & -0.5 \leq x < 0 \\ (1.0, 0.4, 2.0), & 0 \leq x < 0.5 \end{cases} \tag{3.4.5}$$

and the calculation stops at a time of 0.1. The problem consists of two strong rarefaction waves, one moving to the left and the other to right, and produces a very low pressure and density region around $x = 0$. Many schemes fail, giving negative pressure and density in the region and therefore, violate the so called positivity property. Thus this test serves to judge the positivity of

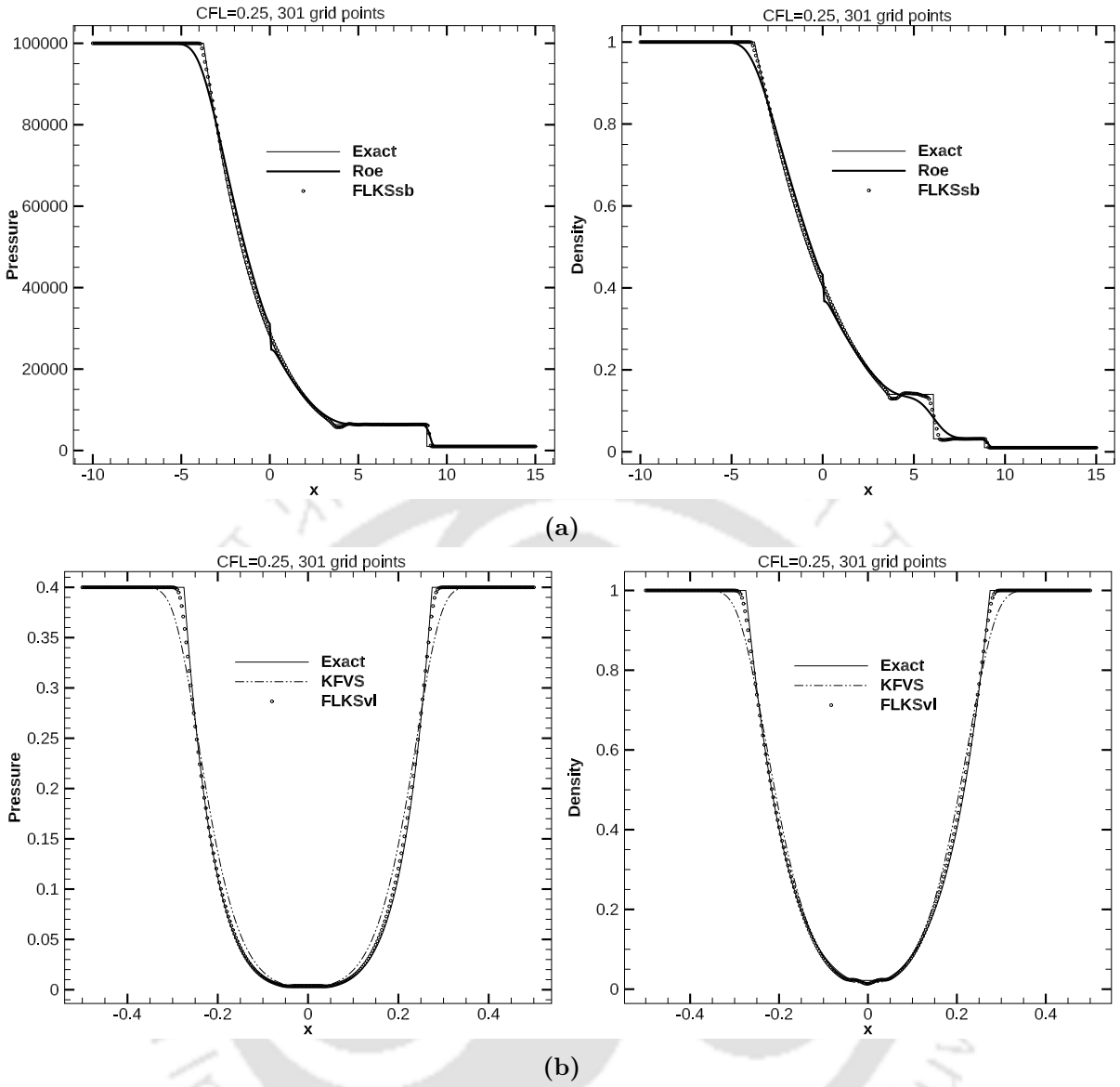

Figure 3.6. (a) Pressure (left) and density (right) plots for Sod type shock tube problem that gives expansive sonic point in expansion fan region. (b) Pressure (left) and density (right) plots for Einfeldt et. al. test involving strong rarefaction wave.

a scheme. Figure 3.6(b) shows pressure and density plots using KFVS and FLKS schemes. Both the schemes satisfy positivity and FLKS being a high resolution scheme resolves the corners of the expansion fans well.

3.4.3 Blast wave problem

This test problem is described in the work of Woodward and Colella [57]. A tube of unit length is considered with computational domain $[0, 1]$. Initially three constant states of a gamma law gas ($\gamma = 1.4$) at rest is filled in the tube which is closed at the ends by reflecting walls. The

density is 1.0 everywhere. The pressure in the leftmost $\frac{1}{10}$th portion is 1000, in the rightmost $\frac{1}{10}$th portion is 100, and in the rest of the tube is 0.01. Thus there are two discontinuities in the initial condition. The schematic of the setup is shown in Figure 3.7. Once the flow starts

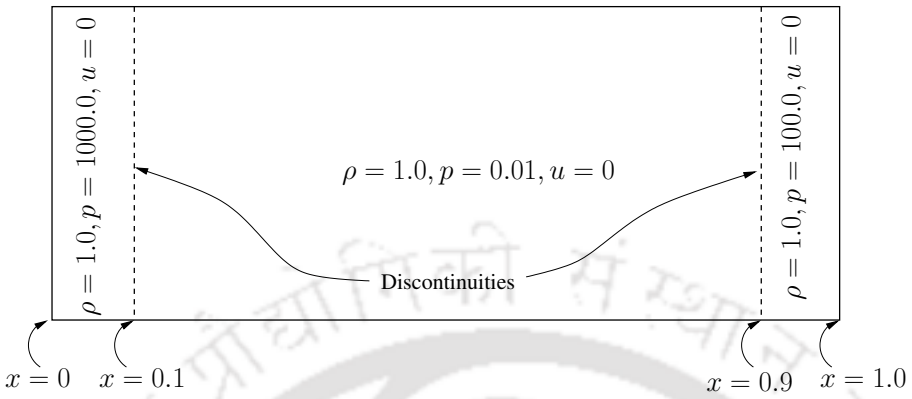

Figure 3.7. 1D blast wave problem setup

evolving two blast waves get generated and collide with each other. Calculation is stopped at a time of 0.038. By this time multiple interactions of discontinuities like shocks and contacts take place. At the walls, reflection boundary treatment is done. Interaction of discontinuities takes place in small regions and hence a fine grid is needed to resolve the flow features properly. Figure 3.8 shows performance of FLKS scheme with Van Leer limiter. For all calculations a CFL number of 0.25 has been used, although higher CFL values up to around 1.0 can be used. Exact solution of this problem is not known, so the Sweby's flux limited version of Roe scheme as described in the work of Roe [52] with Van Leer limiter is used to generate results on a fine grid with 4001 grid points. This is taken as the reference solution for comparison. Figure 3.8(a) shows density and velocity plots on a grid with 301 points. Figure 3.8(b) shows similar plots on a grid with 1001 points. The improvement in capturing sharp corners and discontinuities is obvious with refinement of grid.

3.4.4 Shu-Osher shock-entropy wave interaction problem

This test problem is discussed in the work of Shu and Osher [68]. This problem involves a computational domain $[-5, 5]$. The domain is initialized as

$$\rho = 3.857143, \quad u = 2.629369, \quad p = 10.33333 \quad \text{for} \quad x < -4,$$
$$\rho = 1 + 0.2 \sin 5x, \quad u = 0, \quad p = 1.0 \quad \text{for} \quad x \geq -4.$$

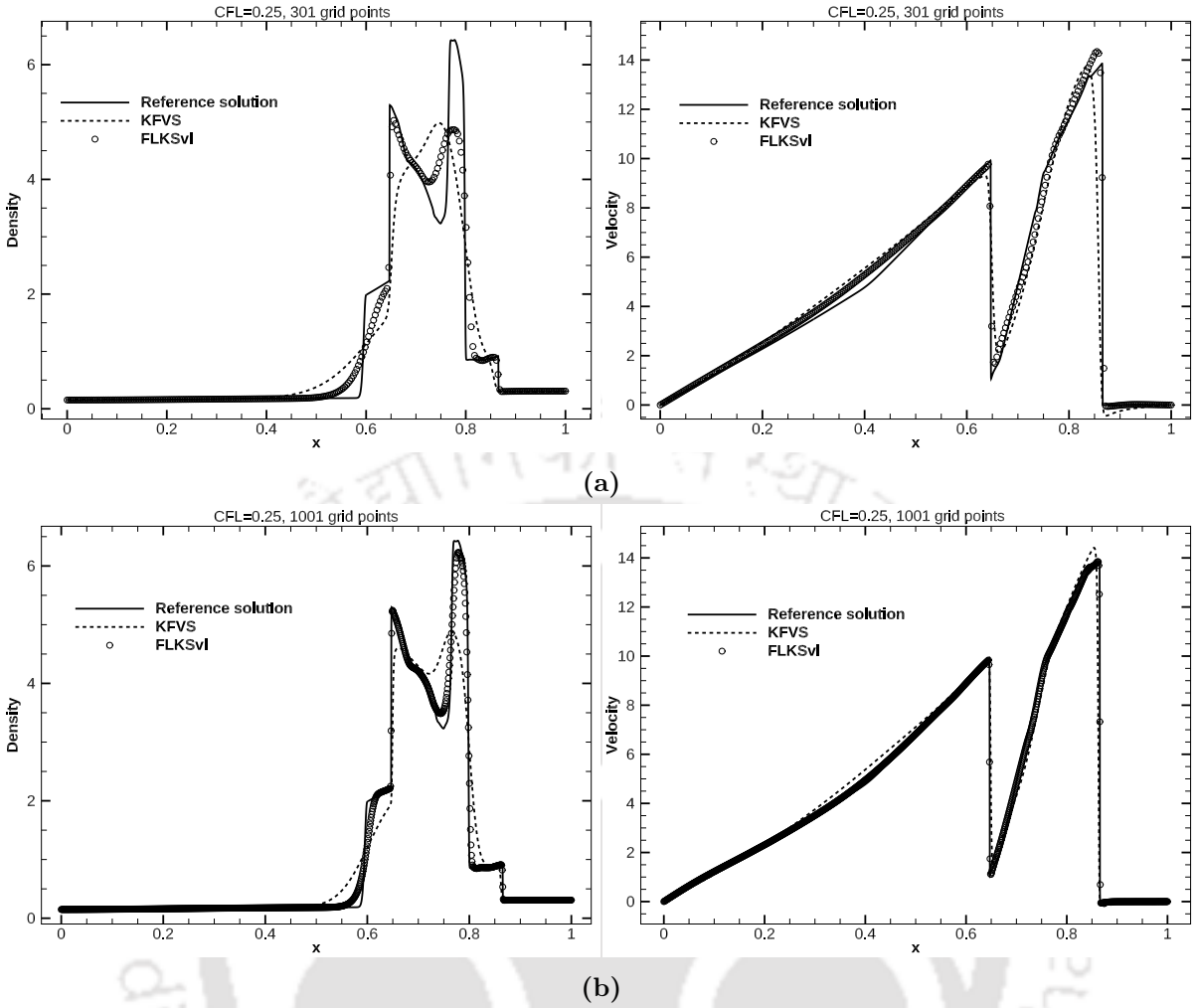

Figure 3.8. 1D Blast wave problem. Density (left) and velocity (right) plots obtained using (a) 301 and (b) 1001 grid points, respectively with CFL= 0.25. The calculation stops at a time of 0.038.

This setup results in an interaction of a Mach 3 shock and a sine wave in density. The calculation stops at a time of 1.8.

Figure 3.9 shows the density plot using 501 grid points. A CFL number of 0.8 is used. This test is considered here to check the compatibility of extremum-preserving limiter with FLKS scheme. The adaptation of extremum-preserving Van Leer limiter with FLKS scheme is described in Section 3.3. Again the density plot obtained using Sweby's flux limited version of Roe scheme [52] with 2001 grid points is taken as the reference solution. The figure clearly shows the improvement in extrema capturing with extremum-preserving limiter.

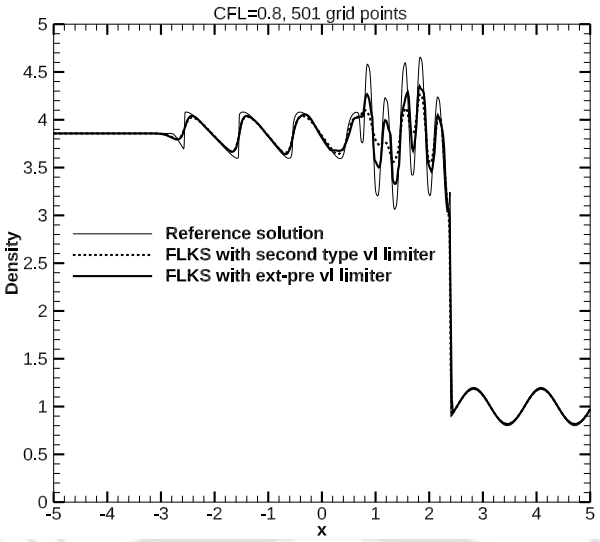

Figure 3.9. Density plot obtained for Shu-Osher problem using 501 grid points with CFL= 0.8. The calculation stops at a time of 1.8.

3.4.5 Comparison of FLKS scheme with a high resolution KFVS scheme

A comparison of the performance of FLKS scheme and the second-order high resolution KFVS scheme (HRKFVS) [38] for Sod and blast wave tests is shown in the Figure 3.10. "HRKFVS

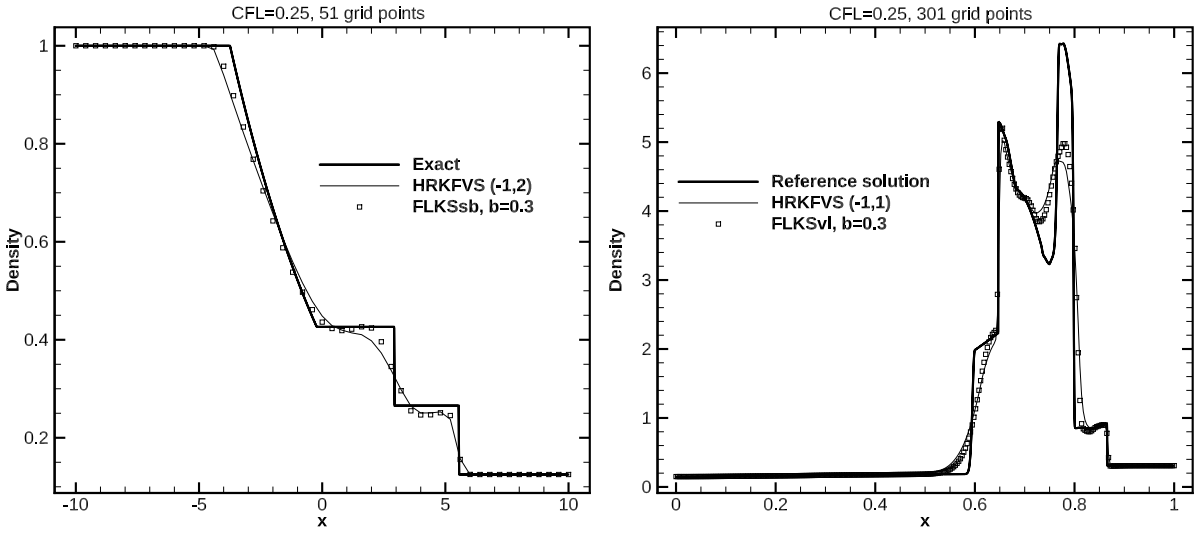

(a) Sod test **(b)** Blast wave test

Figure 3.10. Comparison of FLKS scheme with HRKFVS scheme.

$(-1, 2)$" indicates that two user adjustable parameters -1 and 2 have been used with HRKFVS. The parameters in HRKFVS and FLKS schemes are so chosen as to give very accurate solution within their capabilities. These optimum values of the parameters for both the schemes provide a fair comparison. We observe that FLKS scheme gives better resolution at shocks, contacts,

corners of expansion fans and other high gradient regions. In addition, FLKS scheme is flexible enough to allow the use of specifically designed limiters. An example is the extrema-preserving limiter as described in Section 3.3.

3.5 Conclusions

This chapter gives the formulation of the FLKS scheme. Three different methods are discussed to arrive at the final Euler level formulation. Careful evaluation of the performance of these schemes for several standard test problems suggest that **Method** 1 is the best among them. This FLKS scheme is then modified to make a provision for relaxing TVD criteria such that even better resolution can be obtained at discontinuities. An extremum-preserving limiter is also adapted to be used with FLKS. This results in the reduction of extrema clipping. Finally, several test problems are solved to demonstrate the accuracy and robustness of the new scheme. It is observed that FLKS achieves close to second order accuracy for small CFL numbers and the accuracy is better than second-order HRKFVS solution. The next chapter discusses a 2D version of the scheme.

Chapter 4

Extension of 1D FLKS Scheme to 2D on Cartesian Grid

This chapter proposes a way to extend the 1D FLKS scheme to 2D Cartesian grids. Several stringent tests are performed with the 2D version of the scheme to test its accuracy and robustness.

4.1 2D FLKS Scheme Using Dimensional Splitting

The simplest and straightforward way to extend a scheme for 1D Euler equations to 2D case is to use dimensional splitting. On a Cartesian mesh this method first splits the 2D Euler equations (2.4.1) into two 1D augmented Euler equations [5] in the x- and y-directions, respectively.

$$\frac{\partial \mathbf{U}}{\partial t} + \frac{\partial \mathbf{FX}}{\partial x} = 0 \tag{4.1.1a}$$

$$\frac{\partial \mathbf{U}}{\partial t} + \frac{\partial \mathbf{FY}}{\partial y} = 0 \tag{4.1.1b}$$

The equations (4.1.1a) have one extra y-direction momentum equation and equations (4.1.1b) have one extra x-direction momentum equation unlike the 1D Euler equations (2.1.1). Dimensional splitting requires equation (4.1.1a) to be solved in x-direction (x-sweep) and equation (4.1.1b) to be solved in y-direction (y-sweep) separately in sequences where the solution of a sweep serves as the initial condition for the next consecutive sweep.

The FLKS scheme (3.1.12) or (3.1.13) cannot be directly implemented to solve the augmented Euler equations (4.1.1) since there are extra momentum equations involved. We first split the 2D Boltzmann equation (2.5.1) into two separate 1D advection equations as

$$\frac{\partial F}{\partial t} + v_1 \frac{\partial F}{\partial x} = 0, \tag{4.1.2a}$$

$$\frac{\partial F}{\partial t} + v_2 \frac{\partial F}{\partial y} = 0. \tag{4.1.2b}$$

Now the $\boldsymbol{\Psi}$-moment (defined by equation (2.5.4)) of these equations (4.1.2a) and (4.1.2b) give equations (4.1.1a) and (4.1.1b), respectively. One can thus follow the same flux-limited procedure as used in Section 3.1 to obtain Boltzmann level schemes of the form (3.1.5) for the split 1D Boltzmann equations (4.1.2). The $\boldsymbol{\Psi}$-moment (2.5.4) of these Boltzmann level schemes then gives the Euler level schemes of the form (3.1.12) for augmented Euler equations (4.1.1a) and (4.1.1b), respectively, as

$$\begin{aligned}
\mathbf{U}_{i,j}^{n+1} &= \mathbf{U}_{i,j}^{n} - \lambda_1 \left[\left(\mathbf{FX}_{i,j}^{+^n} - \mathbf{FX}_{i-1,j}^{+^n} \right) + \left(\mathbf{FX}_{i+1,j}^{-^n} - \mathbf{FX}_{i,j}^{-^n} \right) \right] \\
&- \frac{\lambda_1}{2} \left[\text{avg} \left(\left(\mathbf{FX}_{i+1,j}^{+^n} - \mathbf{FX}_{i,j}^{+^n} \right), \left(\mathbf{FX}_{i,j}^{+^n} - \mathbf{FX}_{i-1,j}^{+^n} \right) \right) - \text{avg} \left(\left(\mathbf{FX}_{i,j}^{+^n} - \mathbf{FX}_{i-1,j}^{+^n} \right), \left(\mathbf{FX}_{i-1,j}^{+^n} - \mathbf{FX}_{i-2,j}^{+^n} \right) \right) \right] \\
&+ \frac{\lambda_1}{2} \left[\text{avg} \left(\left(\mathbf{FX}_{i+2,j}^{-^n} - \mathbf{FX}_{i+1,j}^{-^n} \right), \left(\mathbf{FX}_{i+1,j}^{-^n} - \mathbf{FX}_{i,j}^{-^n} \right) \right) - \text{avg} \left(\left(\mathbf{FX}_{i+1,j}^{-^n} - \mathbf{FX}_{i,j}^{-^n} \right), \left(\mathbf{FX}_{i,j}^{-^n} - \mathbf{FX}_{i-1,j}^{-^n} \right) \right) \right] \\
&+ \frac{\lambda_1^2}{2} \left[\text{avg} \left(\left(\mathbf{GX}_{i+1,j}^{+^n} - \mathbf{GX}_{i,j}^{+^n} \right), \left(\mathbf{GX}_{i,j}^{+^n} - \mathbf{GX}_{i-1,j}^{+^n} \right) \right) - \text{avg} \left(\left(\mathbf{GX}_{i,j}^{+^n} - \mathbf{GX}_{i-1,j}^{+^n} \right), \left(\mathbf{GX}_{i-1,j}^{+^n} - \mathbf{GX}_{i-2,j}^{+^n} \right) \right) \right] \\
&+ \frac{\lambda_1^2}{2} \left[\text{avg} \left(\left(\mathbf{GX}_{i+2,j}^{-^n} - \mathbf{GX}_{i+1,j}^{-^n} \right), \left(\mathbf{GX}_{i+1,j}^{-^n} - \mathbf{GX}_{i,j}^{-^n} \right) \right) - \text{avg} \left(\left(\mathbf{GX}_{i+1,j}^{-^n} - \mathbf{GX}_{i,j}^{-^n} \right), \left(\mathbf{GX}_{i,j}^{-^n} - \mathbf{GX}_{i-1,j}^{-^n} \right) \right) \right]
\end{aligned} \tag{4.1.3a}$$

and

$$\begin{aligned}
\mathbf{U}_{i,j}^{n+1} &= \mathbf{U}_{i,j}^{n} - \lambda_2 \left[\left(\mathbf{FY}_{i,j}^{+^n} - \mathbf{FY}_{i,j-1}^{+^n} \right) + \left(\mathbf{FY}_{i,j+1}^{-^n} - \mathbf{FY}_{i,j}^{-^n} \right) \right] \\
&- \frac{\lambda_2}{2} \left[\text{avg} \left(\left(\mathbf{FY}_{i,j+1}^{+^n} - \mathbf{FY}_{i,j}^{+^n} \right), \left(\mathbf{FY}_{i,j}^{+^n} - \mathbf{FY}_{i,j-1}^{+^n} \right) \right) - \text{avg} \left(\left(\mathbf{FY}_{i,j}^{+^n} - \mathbf{FY}_{i,j-1}^{+^n} \right), \left(\mathbf{FY}_{i,j-1}^{+^n} - \mathbf{FY}_{i,j-2}^{+^n} \right) \right) \right] \\
&+ \frac{\lambda_2}{2} \left[\text{avg} \left(\left(\mathbf{FY}_{i,j+2}^{-^n} - \mathbf{FY}_{i,j+1}^{-^n} \right), \left(\mathbf{FY}_{i,j+1}^{-^n} - \mathbf{FY}_{i,j}^{-^n} \right) \right) - \text{avg} \left(\left(\mathbf{FY}_{i,j+1}^{-^n} - \mathbf{FY}_{i,j}^{-^n} \right), \left(\mathbf{FY}_{i,j}^{-^n} - \mathbf{FY}_{i,j-1}^{-^n} \right) \right) \right] \\
&+ \frac{\lambda_2^2}{2} \left[\text{avg} \left(\left(\mathbf{GY}_{i,j+1}^{+^n} - \mathbf{GY}_{i,j}^{+^n} \right), \left(\mathbf{GY}_{i,j}^{+^n} - \mathbf{GY}_{i,j-1}^{+^n} \right) \right) - \text{avg} \left(\left(\mathbf{GY}_{i,j}^{+^n} - \mathbf{GY}_{i,j-1}^{+^n} \right), \left(\mathbf{GY}_{i,j-1}^{+^n} - \mathbf{GY}_{i,j-2}^{+^n} \right) \right) \right] \\
&+ \frac{\lambda_2^2}{2} \left[\text{avg} \left(\left(\mathbf{GY}_{i,j+2}^{-^n} - \mathbf{GY}_{i,j+1}^{-^n} \right), \left(\mathbf{GY}_{i,j+1}^{-^n} - \mathbf{GY}_{i,j}^{-^n} \right) \right) - \text{avg} \left(\left(\mathbf{GY}_{i,j+1}^{-^n} - \mathbf{GY}_{i,j}^{-^n} \right), \left(\mathbf{GY}_{i,j}^{-^n} - \mathbf{GY}_{i,j-1}^{-^n} \right) \right) \right],
\end{aligned} \tag{4.1.3b}$$

where $\lambda_1 = \frac{\Delta t}{\Delta x}$ and $\lambda_2 = \frac{\Delta t}{\Delta y}$, and the split fluxes $\mathbf{FX}^{\pm}$, $\mathbf{FY}^{\pm}$, $\mathbf{GX}^{\pm}$ and $\mathbf{GY}^{\pm}$ are given by

$$\mathbf{FX}^{\pm} = \begin{bmatrix} FX^{(1)^{\pm}} \\ FX^{(2)^{\pm}} \\ FX^{(3)^{\pm}} \\ FX^{(4)^{\pm}} \end{bmatrix} = \left\langle \boldsymbol{\Psi}, \frac{v_1 \pm |v_1|}{2} F \right\rangle$$

$$= \begin{bmatrix} \rho u \\ p + \rho u^2 \\ \rho u v \\ \left\{ \frac{\gamma}{\gamma - 1} p + \frac{1}{2} \rho (u^2 + v^2) \right\} u \end{bmatrix} X_1^{\pm} \pm \begin{bmatrix} \rho \\ \rho u \\ \rho v \\ \frac{\gamma+1}{2(\gamma-1)} p + \frac{1}{2} \rho (u^2 + v^2) \end{bmatrix} Y_1 \quad (4.1.4a)$$

$$\mathbf{FY}^{\pm} = \begin{bmatrix} FY^{(1)^{\pm}} \\ FY^{(2)^{\pm}} \\ FY^{(3)^{\pm}} \\ FY^{(4)^{\pm}} \end{bmatrix} = \left\langle \boldsymbol{\Psi}, \frac{v_2 \pm |v_2|}{2} F \right\rangle$$

$$= \begin{bmatrix} \rho v \\ \rho u v \\ p + \rho v^2 \\ \left\{ \frac{\gamma}{\gamma - 1} p + \frac{1}{2} \rho (u^2 + v^2) \right\} v \end{bmatrix} X_2^{\pm} \pm \begin{bmatrix} \rho \\ \rho u \\ \rho v \\ \frac{\gamma+1}{2(\gamma-1)} p + \frac{1}{2} \rho (u^2 + v^2) \end{bmatrix} Y_2 \quad (4.1.4b)$$

$$\mathbf{GX}^{\pm} = \begin{bmatrix} GX^{(1)^{\pm}} \\ GX^{(2)^{\pm}} \\ GX^{(3)^{\pm}} \\ GX^{(4)^{\pm}} \end{bmatrix} = \left\langle \boldsymbol{\Psi}, v_1 \frac{v_1 \pm |v_1|}{2} F \right\rangle$$

$$= \begin{bmatrix} p + \rho u^2 \\ (3p + \rho u^2) u \\ (p + \rho u^2) v \\ \frac{\gamma}{\gamma - 1} \frac{p^2}{\rho} + \frac{5\gamma - 3}{2(\gamma - 1)} p u^2 + \frac{1}{2} p v^2 + \frac{\rho u^2}{2} (u^2 + v^2) \end{bmatrix} X_1^{\pm} \pm \begin{bmatrix} \rho u \\ 2p + \rho u^2 \\ \rho u v \\ \frac{2\gamma - 1}{\gamma - 1} p u + \frac{\rho u}{2} (u^2 + v^2) \end{bmatrix} Y_1 \quad (4.1.4c)$$

$$\mathbf{GY}^{\pm} = \begin{bmatrix} GY^{(1)^{\pm}} \\ GY^{(2)^{\pm}} \\ GY^{(3)^{\pm}} \\ GY^{(4)^{\pm}} \end{bmatrix} = \left\langle \boldsymbol{\Psi}, v_2 \frac{v_2 \pm |v_2|}{2} F \right\rangle$$

$$= \begin{bmatrix} p + \rho v^2 \\ (p + \rho v^2)u \\ (3p + \rho v^2)v \\ \frac{\gamma}{\gamma-1}\frac{p^2}{\rho} + \frac{5\gamma-3}{2(\gamma-1)}pv^2 + \frac{1}{2}pu^2 + \frac{\rho v^2}{2}(u^2+v^2) \end{bmatrix} X_2^{\pm} \pm \begin{bmatrix} \rho v \\ \rho uv \\ 2p + \rho v^2 \\ \frac{2\gamma-1}{\gamma-1}pv + \frac{\rho v}{2}(u^2+v^2) \end{bmatrix} Y_2, \tag{4.1.4d}$$

where

$$X_1^{\pm} = \frac{1 \pm \mathrm{erf}(S_1)}{2}, \quad Y_1 = \frac{e^{-S_1^2}}{2\sqrt{\pi\beta}}, \quad S_1 = u\sqrt{\beta} \tag{4.1.5a}$$

$$X_2^{\pm} = \frac{1 \pm \mathrm{erf}(S_2)}{2}, \quad Y_2 = \frac{e^{-S_2^2}}{2\sqrt{\pi\beta}}, \quad S_2 = v\sqrt{\beta} \tag{4.1.5b}$$

with $\beta = \frac{1}{2RT}$. One can again notice as in (3.1.16) and (3.1.17) that

$$\begin{aligned} \langle \boldsymbol{\Psi}, v_1 F \rangle &= \left\langle \boldsymbol{\Psi}, \frac{v_1 + |v_1|}{2} F + \frac{v_1 - |v_1|}{2} F \right\rangle \\ &= \left\langle \boldsymbol{\Psi}, \frac{v_1 + |v_1|}{2} F \right\rangle + \left\langle \boldsymbol{\Psi}, \frac{v_1 - |v_1|}{2} F \right\rangle \end{aligned} \tag{4.1.6a}$$

$$\text{So,} \quad \mathbf{FX} = \mathbf{FX}^{+} + \mathbf{FX}^{-} \tag{4.1.6b}$$

and

$$\begin{aligned} \langle \boldsymbol{\Psi}, v_2 F \rangle &= \left\langle \boldsymbol{\Psi}, \frac{v_2 + |v_2|}{2} F + \frac{v_2 - |v_2|}{2} F \right\rangle \\ &= \left\langle \boldsymbol{\Psi}, \frac{v_2 + |v_2|}{2} F \right\rangle + \left\langle \boldsymbol{\Psi}, \frac{v_2 - |v_2|}{2} F \right\rangle \end{aligned} \tag{4.1.6c}$$

$$\text{So,} \quad \mathbf{FY} = \mathbf{FY}^{+} + \mathbf{FY}^{-}. \tag{4.1.6d}$$

In addition,

$$\begin{aligned}\left\langle \boldsymbol{\Psi}, v_1^2 F \right\rangle &= \left\langle \boldsymbol{\Psi}, v_1 \frac{v_1 + |v_1|}{2} F + v_1 \frac{v_1 - |v_1|}{2} F \right\rangle \\ &= \left\langle \boldsymbol{\Psi}, v_1 \frac{v_1 + |v_1|}{2} F \right\rangle + \left\langle \boldsymbol{\Psi}, v_1 \frac{v_1 - |v_1|}{2} F \right\rangle \qquad (4.1.7a)\end{aligned}$$

$$\text{So,} \quad \mathbf{GX} = \mathbf{GX}^+ + \mathbf{GX}^- \qquad (4.1.7b)$$

and

$$\begin{aligned}\left\langle \boldsymbol{\Psi}, v_2^2 F \right\rangle &= \left\langle \boldsymbol{\Psi}, v_2 \frac{v_2 + |v_2|}{2} F + v_1 \frac{v_2 - |v_2|}{2} F \right\rangle \\ &= \left\langle \boldsymbol{\Psi}, v_2 \frac{v_2 + |v_2|}{2} F \right\rangle + \left\langle \boldsymbol{\Psi}, v_2 \frac{v_2 - |v_2|}{2} F \right\rangle \qquad (4.1.7c)\end{aligned}$$

$$\text{So,} \quad \mathbf{GY} = \mathbf{GY}^+ + \mathbf{GY}^-, \qquad (4.1.7d)$$

where $\mathbf{GX} = \left\langle \boldsymbol{\Psi}, v_1^2 F \right\rangle$ and $\mathbf{GY} = \left\langle \boldsymbol{\Psi}, v_2^2 F \right\rangle$ kind of fluxes arise due to the use of Lax-Wendroff flux in flux-limiting as in equation (3.1.1).

Now 2D version of FLKS scheme can be implemented using dimensional splitting where x-sweep and y-sweep are done by equations (4.1.3a) and (4.1.3b), respectively. In addition, as in 1D case the TVD criterion gets relaxed by multiplying $\frac{\lambda_1^2}{2}$ and $\frac{\lambda_2^2}{2}$ terms by b (< 1.0).

4.2 Results and Discussion

This section discusses several test problems for 2D inviscid flows. For time evolution a global time step Δt is determined first for time integration. This Δt depends on a CFL value chosen. We use

$$\Delta t = \text{CFL} \times \min\left(\frac{\Delta x}{\max\limits_{i,j} \left(|u_{i,j}| + a_{i,j} \right)}, \frac{\Delta y}{\max\limits_{i,j} \left(|v_{i,j}| + a_{i,j} \right)} \right) \qquad (4.2.1)$$

where u and v are x- and y-components of fluid velocity, and i and j denote x- and y-direction cell indices, respectively. In the tables and figures to follow, FLKSmm, FLKSvl and FLKSsb stand for FLKS scheme with minmod, Van Leer and superbee limiters, respectively, with $b = 1.0$. When showing results for $b < 1.0$, explicit mention of the b value is done.

Here accuracy test is performed first and then four test problems are solved with FLKS scheme on Cartesian mesh using dimensional splitting. Sweeps in x- and y-direction are performed with a constant time step size Δt on the n^{th} time level data $\mathbf{U}^n$ to get $(n+1)^{th}$ time level solution $\mathbf{U}^{n+1}$. Denoting the x-sweep and y-sweep in operator form as $X^{(\Delta t)}$ and $Y^{(\Delta t)}$,

respectively, the accuracy analysis has been done using

$$\mathbf{U}^{n+1} = \frac{1}{2}\left[X^{(\Delta t)}Y^{(\Delta t)} + Y^{(\Delta t)}X^{(\Delta t)}\right](\mathbf{U}^n) \tag{4.2.2}$$

which is expected to give second-order time accuracy [5] and the four test problems have been solved using

$$\mathbf{U}^{n+1} = Y^{(\Delta t)}X^{(\Delta t)}(\mathbf{U}^n) \tag{4.2.3}$$

which is a first-order time accurate method [5]. As in Chapter 3, the physical quantities in all the tests are in SI units, however, the units are not mentioned explicitly.

4.2.1 Accuracy test

The isentropic vortex problem as described in the work of Balsara [69] is used for accuracy test. A computational domain $[-5, 5] \times [-5, 5]$ with periodic boundaries is used and the calculation stops at a time of 10.0. The full detail of the problem is not mentioned here as is well described in the work of Balsara [69] and other references. Table 4.1 shows the global order of accuracy

Table 4.1 Order of accuracy of FLKS scheme with minmod limiter for 2D case on Cartesian grid. L_1 and L_∞ error norms for density are used for order calculation.

Scheme	Number of cells	L_1 error	L_1 order	L_∞ error	L_∞ order
FLKSmm, CFL= 0.25	20×20	0.022952		0.380314	
	40×40	0.014929	0.62	0.298839	0.35
	80×80	0.007160	1.06	0.138135	1.11
	160×160	0.003137	1.19	0.060332	1.20
	320×320	0.001410	1.15	0.030322	0.99
FLKSmm, CFL= 0.1	20×20	0.022633		0.376710	
	40×40	0.013935	0.70	0.282006	0.42
	80×80	0.005717	1.29	0.114663	1.30
	160×160	0.002036	1.49	0.049403	1.21
	320×320	0.000765	1.41	0.026204	0.91

of FLKS scheme with minmod limiter. L_1 and L_∞ error norms for density are used for order calculation. Here again as in 1D, low CFL values give better order of convergence and hence CFL values 0.25 and 0.1 are chosen.

4.2.2 Forward facing step problem

This well-known test problem is described in the work of Woodward and Colella [57]. A uniform Mach 3 flow enters a wind tunnel of length 3 units and width 1 unit. The tunnel contains a step of height 0.2 units situated at a distance of 0.6 units from the left-hand-side entry. At the left end continuous flow of a gamma-law gas ($\gamma = 1.4$) with density 1.4, pressure 1.0 and x-velocity 3.0 (y-velocity is 0) is supplied, and at the right end of the tunnel zero gradient boundary condition is imposed. At the top and bottom solid boundary, reflection boundary treatment is done. The domain is initialized with the inflow gas condition.

Figure 4.1 shows the density contours on a 240×80 Cartesian grid. A CFL number of 0.5 has been used and the calculation stops at 4.0 time units. The calculation works for higher CFL values close to 1.0 as well. No special treatment for the singular step corner point has been done. Figures 4.1(a), 4.1(b) and 4.1(c), respectively show the calculations by first order KFVS scheme, FLKS scheme with minmod limiter and FLKS scheme with superbee limiter. The figures clearly show the expected improvement in the results by using the present flux limited scheme compared to KFVS scheme. Clearly the reflected shock, the curved shock ahead of the step and the Mach stem are captured well by FLKS. Furthermore, as more compressive limiter is used (while going from minmod limiter to superbee limiter), the crispness of the shocks increases. The sonic line just above the corner of the step makes several schemes to give an expansion shock suggesting the violation of entropy condition. The first-order Godunov scheme is an example [57], and as the Figures 4.1(b) and 4.1(c) clearly show, FLKS does not display any such nonphysical behaviour.

4.2.3 Double Mach reflection problem

Woodward and Colella [57] describe the setting for this test problem. A Mach 10 shock in air ($\gamma = 1.4$) interacts with an oblique wedge. The angle between the wedge and shock front is 60°. The wedge surface is made to lie along x-axis. A $[0, 4] \times [0, 1]$ computational domain is considered. Initially the shock is incident at $x = \frac{1}{6}$ and $y = 0$ position and extends up to the top of the problem domain at $y = 1$, the air ahead of the shock is at rest and has density 1.4 and pressure 1. Behind the shock post shock condition is initialized. The region from $x = 0$ to $x = \frac{1}{6}$ at the wedge surface is always assigned initial post shock condition, and at the surface beyond $x = \frac{1}{6}$ reflection boundary condition is applied. The left-hand boundary at $x = 0$ is also fixed with the initial post shock value. At the right hand boundary $x = 4$, all gradients are set

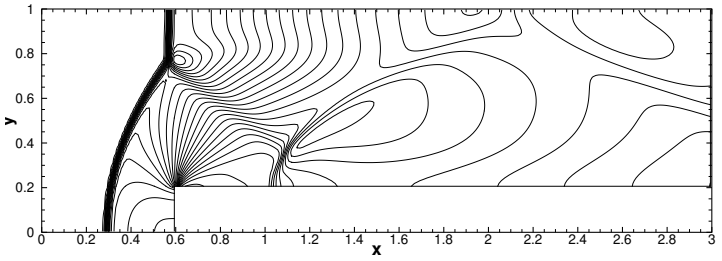

(a) First order KFVS scheme

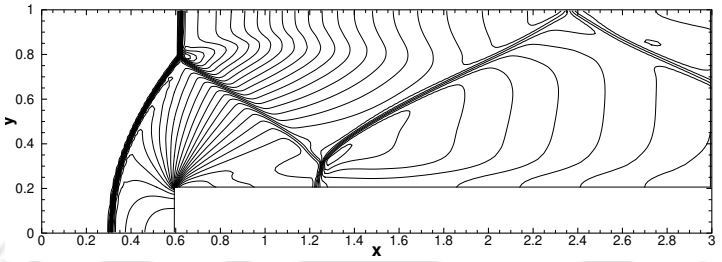

(b) FLKS scheme with minmod limiter

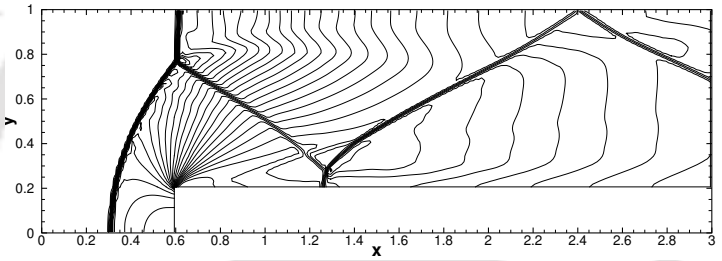

(c) FLKS scheme with superbee limiter

Figure 4.1. Density plot for forward facing step problem using 240×80 Cartesian grid, showing 25 contour levels from 0.6401 to 6.2695 at a time of 4.0.

to zero. The top boundary at $y = 1$ is assigned values in order to follow the exact motion of the Mach 10 shock. A schematic of the setup is shown in Figure 4.2.

Figure 4.3(a) shows results on a 960×240 Cartesian grid with a CFL number of 0.25 and Figure 4.3(b) shows results on a 1600×400 Cartesian grid with a CFL number of 0.5. For a higher CFL value up to around 1.0, FLKS scheme works without difficulty. Figure 4.3 clearly shows the higher resolution achieved by the FLKS scheme in comparison to first order KFVS scheme. In particular, KFVS scheme being highly dissipative is unable to capture the curling up of the primary slip line at the wedge surface (Figure 4.3(a)), but FLKS scheme captures it well apart from clearly resolving the reflected shocks and Mach stems (Figures 4.3(a) and 4.3(b)). Figure 4.3(b) particularly shows higher resolution obtained on a fine grid with superbee limiter. It may be noted that the detailed features of rolling up of the slip line obtained by the present scheme on a relatively coarser grid of 1600×400 is even better than that given by the second-order-accurate genuinely multidimensional Riemann solver [70] on a finer grid of

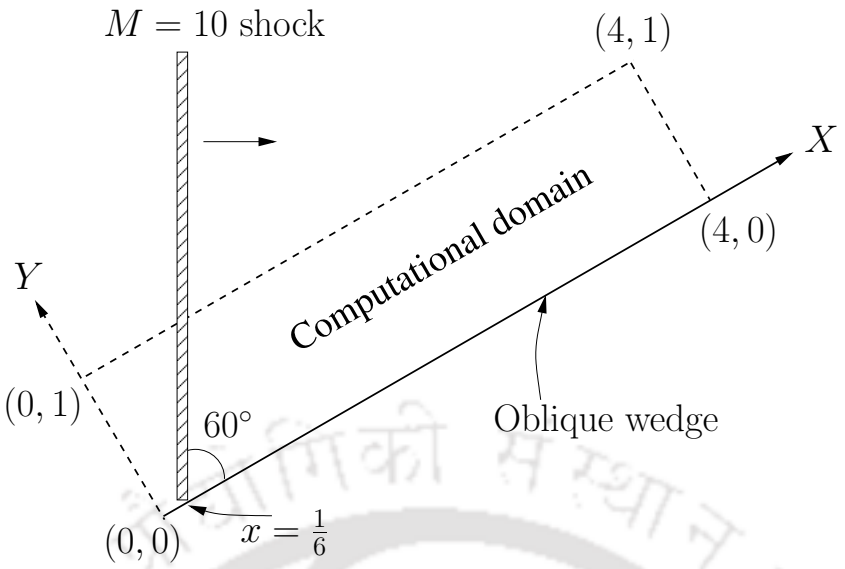

Figure 4.2. Double Mach reflection problem setup

1920×480. Figure 4.4 shows comparison of the performance of extremum-preserving version

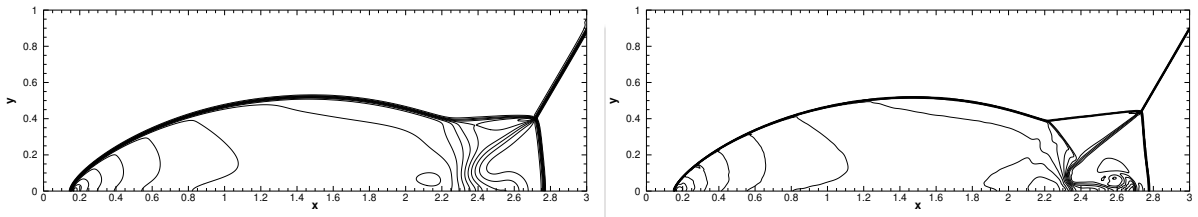

(a) First order KFVS scheme (left) and FLKS scheme with second type Van Leer limiter (right), 960×240 Cartesian grid

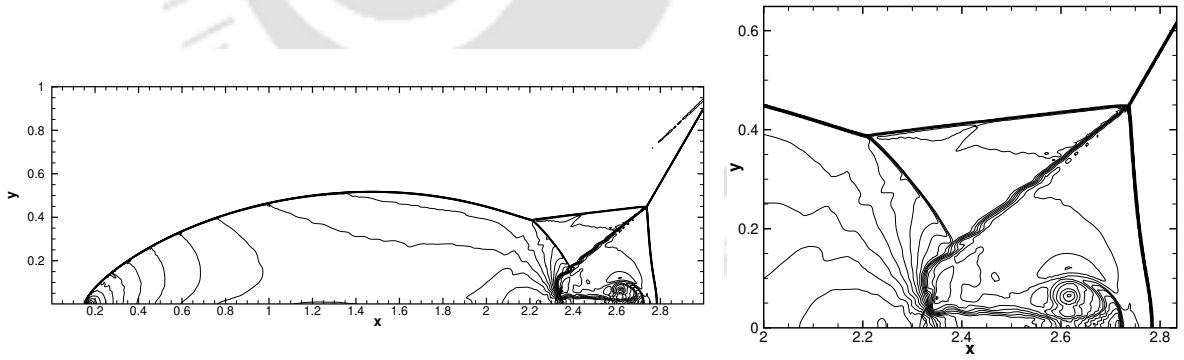

(b) FLKS scheme with superbee limiter, 1600×400 Cartesian grid

Figure 4.3. Density plot for double mach reflection problem. (a) Results for KFVS scheme (left) and FLKS scheme with second type Van Leer limiter (right) using 960×240 Cartesian grid showing 25 contour levels from 1.0 to 20.8. (b) Results for FLKS scheme with superbee limiter for full domain (left) and for expanded triple points region (right) using 1600×400 Cartesian grid showing 36 contour levels from 1.98477 to 22.4517.

of limiter (3.3.9) with the original one on a 960×240 Cartesian grid with a CFL number

of 0.25. When extremum-preserving Van Leer limiter (discussed in Section 3.3) is used with FLKS scheme, only CFL values below 0.5 work. For clarity only the region of the two triple points where most of the interactions are taking place is shown. Figures 4.4(a) and 4.4(b) show that the extremum-preserving limiter seems to capture with better resolution the corners of the curling up configuration of the primary slip line when hit by secondary reflected shock. Thus the compatibility of the extremum-preserving limiter [61] with FLKS scheme in 2D is evident.

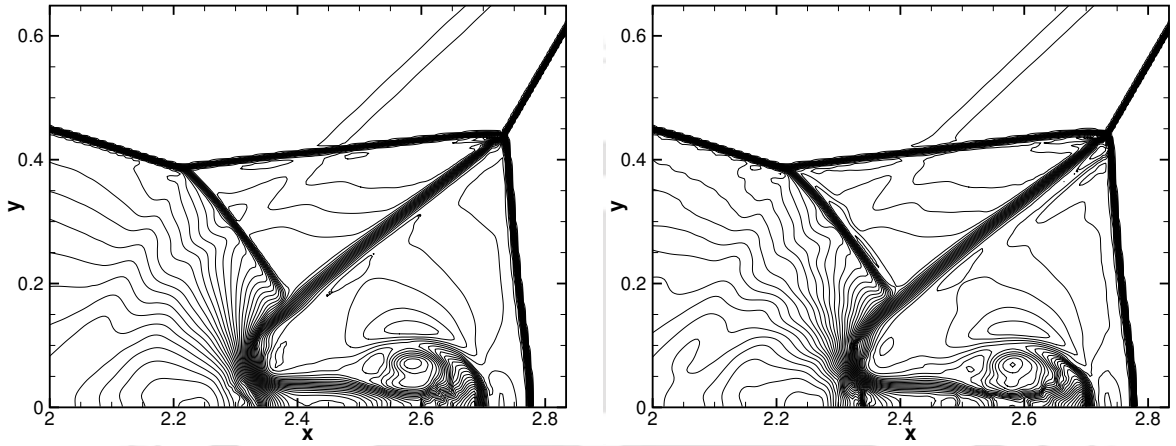

(a) FLKS scheme with second type Van Leer limiter **(b)** FLKS scheme with extremum-preserving second type Van Leer limiter

Figure 4.4. Density plot for double mach reflection problem using 960×240 Cartesian grid, showing 100 contour levels from 1.6097 to 22.3675 at a time of 0.2.

4.2.4 2D Riemann problems

Multidimensional Riemann problems are good tests for a numerical scheme for judging its capability of resolving multidimensional flow features. Brio et al. [71] and Balsara [69] provide the settings for two Riemann problems. A $[-1, 1] \times [-1, 1]$ computational domain is taken. For the first 2D Riemann problem, the following set of values are taken:

$$p = 1.5, \quad \rho = 1.5, \quad u = 0.0, \quad v = 0.0 \quad \text{for} \quad x > 0, \quad y > 0$$

$$p = 0.3, \quad \rho = 0.5323, \quad u = 1.206, \quad v = 0.0 \quad \text{for} \quad x < 0, \quad y > 0$$

$$p = 0.029, \quad \rho = 0.1379, \quad u = 1.206, \quad v = 1.206 \quad \text{for} \quad x < 0, \quad y < 0$$

$$p = 0.3, \quad \rho = 0.5323, \quad u = 0.0, \quad v = 1.206 \quad \text{for} \quad x > 0, \quad y < 0.$$

A schematic is shown in Figure 4.5. This problem has been solved on a 400×400 Cartesian grid with a CFL number of 0.5 (the calculation works for higher CFL values up to around 1.0 as

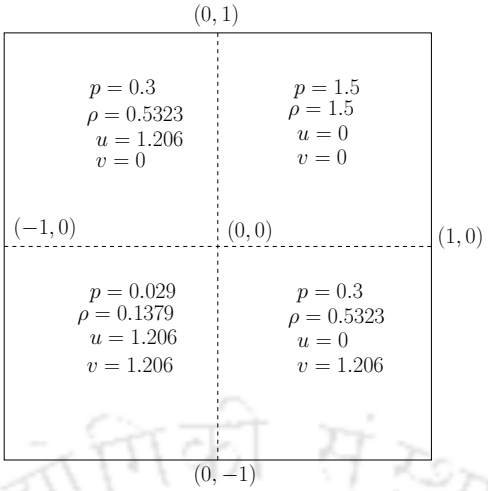

Figure 4.5. First 2D Riemann problem setup

well). The calculation stops at a time of 1.1. The problem starts with four shocks and results in a double Mach reflection. Figure 4.6 shows density contours obtained at time 1.1. Figures 4.6(a) and 4.6(b), respectively show results using first order KFVS scheme and FLKS scheme with superbee limiter. The high resolution obtained with the present flux-limited scheme is obvious. Figures 4.6(c) and 4.6(d) show results using FLKS scheme with superbee limiter with $b = 0.75$ and $b = 0.5$, respectively. These b values relax the TVD criterion gradually as discussed in Section 3.2. This relaxation improves the results, and the shocks, slip lines and the mushroom cap get captured crisply. Figure 4.6(d) shows some spurious oscillations which is expected with a low value of b. A well-designed limiter can give better results with negligible wiggles.

The second Riemann problem consists of the following set of values:

$$
\begin{aligned}
&p = 0.4, \quad \rho = 0.5313, \quad u = 0.0, \quad v = 0.0 \quad \text{for} \quad x > 0, \quad y > 0 \\
&p = 1.0, \quad \rho = 1.0, \quad u = 0.7276, \quad v = 0.0 \quad \text{for} \quad x < 0, \quad y > 0 \\
&p = 1.0, \quad \rho = 0.8, \quad u = 0.0, \quad v = 0.0 \quad \text{for} \quad x < 0, \quad y < 0 \\
&p = 1.0, \quad \rho = 1.0, \quad u = 0.0, \quad v = 0.7276 \quad \text{for} \quad x > 0, \quad y < 0.
\end{aligned}
$$

A schematic is shown in Figure 4.7. This problem is solved on a 400×400 Cartesian grid with a CFL number of 0.5. The calculation stops at a time of 0.52. The solution evolves starting with two shocks and two slip lines. Figure 4.8 shows the density contours obtained by using the KFVS and FLKS schemes. It is clear that flux-limiting makes the shocks and contacts resolve better. Furthermore, referring to Figures 4.8(c) and 4.8(d) we see that the curling up of the slip lines gets captured progressively better as the value of b is reduced from 0.3 to 0.0. But again

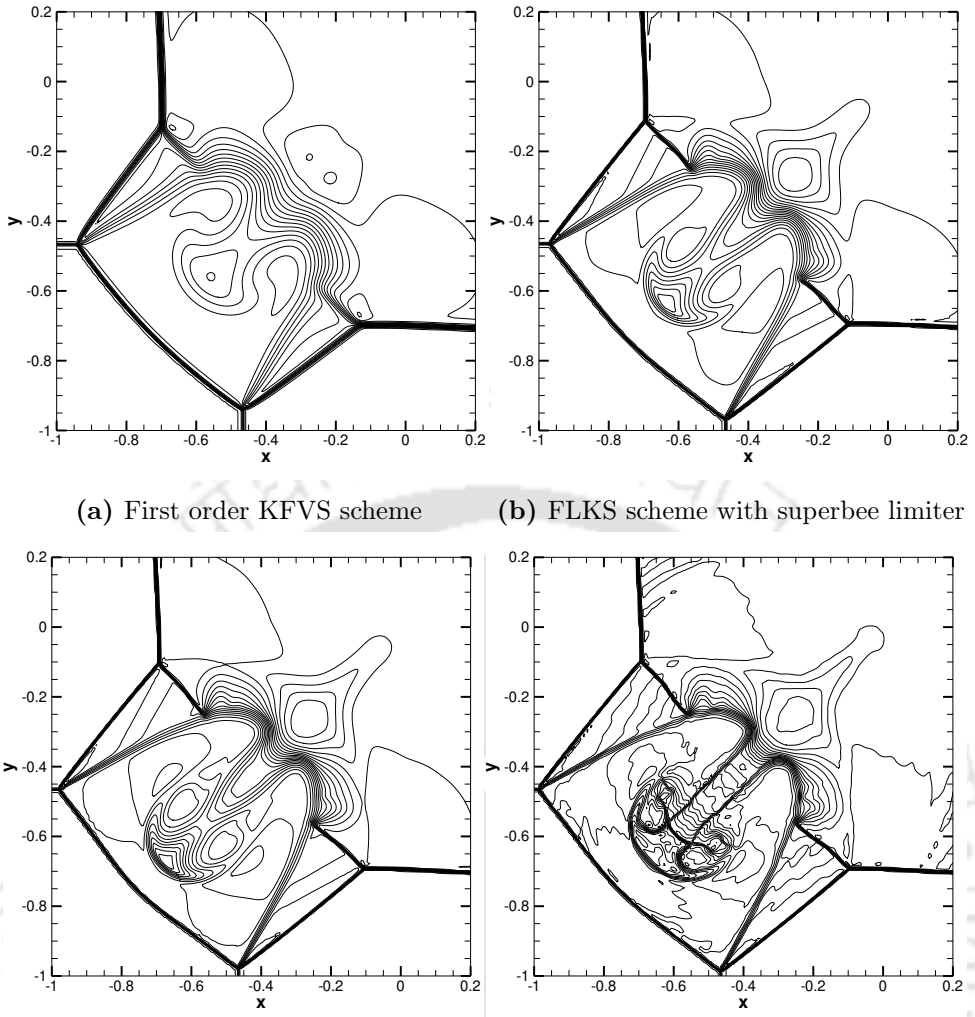

(a) First order KFVS scheme **(b)** FLKS scheme with superbee limiter

(c) FLKS scheme with superbee limiter, b=0.75 **(d)** FLKS scheme with superbee limiter, b=0.5

Figure 4.6. Density plot for first 2D Riemann problem using 400×400 Cartesian grid, showing 28 contour levels from 0.138 to 1.77 at a time of 1.1.

the spurious wiggles come up due to too much relaxation of the TVD condition.

4.3 Conclusions

A 2D version of FLKS scheme on Cartesian grids using dimensional splitting is discussed in this chapter. The order of accuracy is close to 2.0 for small CFL numbers as was the case in 1D. The limiters perform as usual, i.e., the more compressive limiter gives better resolution at discontinuities or high gradient regions. Extrema-preserving limiter when adapted in this 2D formulation works as expected. Although this dimensional splitting procedure is not as sophisticated as a multidimensional Riemann solver but the accuracy achieved and multidimensional flow feature

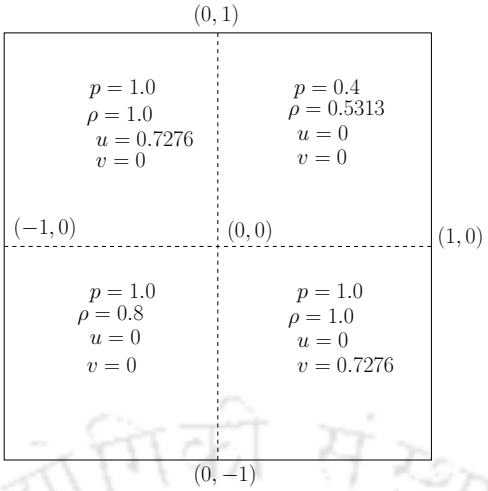

Figure 4.7. Second 2D Riemann problem setup

capturing is better than one such Riemann solver as has been observed in the case of double Mach reflection test problem. The next chapter suggests an extension of the 2D scheme for solution of the Navier-Stokes equations.

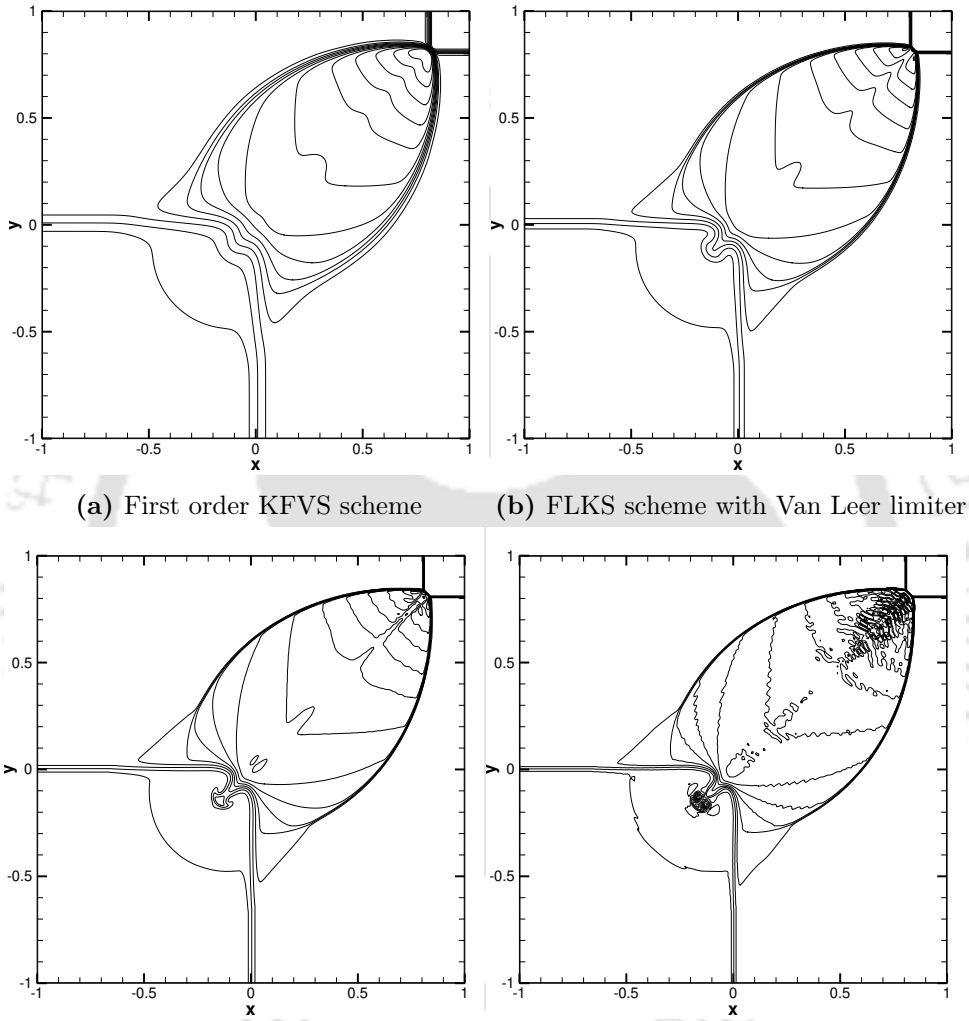

(a) First order KFVS scheme **(b)** FLKS scheme with Van Leer limiter

(c) FLKS scheme with Van Leer limiter, b=0.3 **(d)** FLKS scheme with Van Leer limiter, b=0

Figure 4.8. Density plot for second 2D Riemann problem using 400 × 400 Cartesian grid, showing 20 contour levels from 0.531 to 1.70 at a time of 0.52.

Chapter 5

Extension of FLKS Scheme to Viscous Flows

In the previous chapter, FLKS scheme is used for the solution of 2D Euler equations. This chapter extends the scheme to Navier-Stokes equations for the solution of viscous flow problems. Two different methodologies have been proposed for the extension. The first method simply uses central differencing for the viscous flux terms, which is a very popular way in the literature for Navier-Stokes solutions. The second method uses the full Boltzmann equation with collision term approximated by BGK model, and then Chapman-Enskog procedure followed by Chou-Baganoff [72] splitting of viscous terms results in the final scheme.

5.1 Dimensional Splitting and Discretization of Viscous Flux Terms using Central Differencing

For extending the FLKS scheme to Navier-Stokes equations (2.6.1) we split them into two parts,

$$\frac{\partial \mathbf{U}}{\partial t} + \frac{\partial \mathbf{FX}}{\partial x} = \frac{\partial \mathbf{FX}_v}{\partial x} \tag{5.1.1a}$$

$$\frac{\partial \mathbf{U}}{\partial t} + \frac{\partial \mathbf{FY}}{\partial y} = \frac{\partial \mathbf{FY}_v}{\partial y} \tag{5.1.1b}$$

as is done for dimensional splitting for the Euler equations (2.4.1). The left hand sides of equations (5.1.1a) and (5.1.1b) are discretized using FLKS scheme for the inviscid Euler part and the viscous flux terms are discretized using second-order central differencing in a conventional manner.

For the discretization of x-direction viscous flux terms in equations (5.1.1a) we require derivatives $\frac{\partial u}{\partial x}$, $\frac{\partial u}{\partial y}$, $\frac{\partial v}{\partial x}$, $\frac{\partial v}{\partial y}$ and $\frac{\partial T}{\partial x}$, and u and v values at cell face positions $(i \pm \frac{1}{2}, j)$ for a cell (i, j). The derivatives $\frac{\partial u}{\partial x}$ and $\frac{\partial u}{\partial y}$ are approximated by central differencing as follows:

$$\left(\frac{\partial u}{\partial x}\right)_{i+\frac{1}{2},j} = \frac{u_{i+1,j} - u_{i,j}}{\Delta x}, \tag{5.1.2a}$$

$$\left(\frac{\partial u}{\partial y}\right)_{i+\frac{1}{2},j} = \frac{(u_{i,j+1} + u_{i+1,j+1}) - (u_{i,j-1} + u_{i+1,j-1})}{4\Delta y}. \tag{5.1.2b}$$

By replacing i by $i-1$ in equations (5.1.2) we get the derivatives $\left(\frac{\partial u}{\partial x}\right)_{i-\frac{1}{2},j}$ and $\left(\frac{\partial u}{\partial y}\right)_{i-\frac{1}{2},j}$. In a similar way the derivatives $\left(\frac{\partial v}{\partial x}\right)_{i\pm\frac{1}{2},j}$, $\left(\frac{\partial v}{\partial y}\right)_{i\pm\frac{1}{2},j}$ and $\left(\frac{\partial T}{\partial x}\right)_{i\pm\frac{1}{2},j}$ are obtained. We also use

$$u_{i+\frac{1}{2},j} = \frac{u_{i,j} + u_{i+1,j}}{2}, \tag{5.1.3a}$$

$$v_{i+\frac{1}{2},j} = \frac{v_{i,j} + v_{i+1,j}}{2}. \tag{5.1.3b}$$

Again replacing i by $i-1$ gives $u_{i-\frac{1}{2},j}$ and $v_{i-\frac{1}{2},j}$. The y-direction viscous flux terms in equations (5.1.1b) are discretized following the same procedure as used for equations (5.1.1a).

Thus the FLKS scheme for the Navier-Stokes equations (2.6.1) uses the discretized equations for (5.1.1a) and (5.1.1b) in x-sweep and y-sweep, respectively.

5.2 Results and Discussion for Central Differencing Procedure

Three test cases are considered for evaluating the performance of FLKS scheme as a Navier-Stokes solver. These tests are taken from the work of Xu [43]. As in earlier chapters, the dimensional physical quantities in all the tests are in SI units, however, the units are not mentioned explicitly.

5.2.1 Near incompressible Couette flow

This test involves Couette flow with a temperature gradient. It provides the means to evaluate the capability of a scheme in simulating heat conduction in a viscous flow. The stationary bottom wall is aligned in the x-direction and the top wall situated H distance away above it

moves with a speed U parallel to it. The temperatures of the bottom and top walls are kept fixed at T_0 and T_1, respectively. A schematic of the setup is shown in Figure 5.1. When the

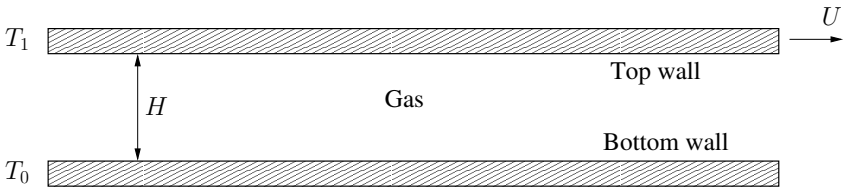

Figure 5.1. Couette flow setup

viscosity and heat conduction coefficients are constants in an incompressible flow, a steady state analytic temperature distribution [43] is obtained as follows:

$$\frac{T - T_0}{T_1 - T_0} = \frac{y}{H} + \frac{\mathrm{PrEc}}{2}\frac{y}{H}\left(1 - \frac{y}{H}\right). \tag{5.2.1}$$

Here $\mathrm{Pr} = \frac{\mu C_p}{k}$ is the Prandtl number, $\mathrm{Ec} = \frac{U^2}{C_p(T_1 - T_0)}$ is the Eckert number and C_p is the specific heat at constant pressure.

We simulate this flow by taking a computational domain of length $L = 1.0$ and width $H = 1.0$. The specific heat ratio $\gamma = 1.4$ and the specific gas constant $\mathrm{R} = 287.0$ are taken. The Mach number $M = \frac{U}{\sqrt{\gamma \mathrm{R} T_0}}$ is fixed at 0.1 to satisfy the incompressibility criterion. At the top and bottom walls isothermal no-slip boundary condition is implemented. At the left and right ends periodic boundary treatment is done. The simulation is done on a 10×10 Cartesian grid with a CFL number of 0.01, $U = 0.003$ and $\mu = 0.05$. The computational domain is initialized with $\rho = 1.0$, $u = U$, $v = 0$ and $T = T_0$. For several combinations of Pr and Ec as given in the work of Xu [43] the results obtained with FLKS scheme using Van Leer limiter are shown in Figure 5.2. The simulated result is in excellent agreement with the analytic solution. The parameters μ, U, CFL number, etc., were chosen in such a way as to keep the inherent numerical viscosity of the FLKS scheme much below the actual physical viscosity μ for obtaining correct Navier-Stokes solution. As described in the work of Xu [6, 43], a KFVS type scheme based on collisionless Boltzmann equation is actually equivalent to using a BGK collision model based Boltzmann equation with relaxation time τ of the order of the numerical time step Δt. And in order to get a correct Navier-Stokes solution the condition $\Delta t << \tau$ must be satisfied. Since the Chapman-Enskog expansion of BGK model based Boltzmann equation to get Navier-Stokes equations [2] gives

$$\mu = \tau p, \tag{5.2.2}$$

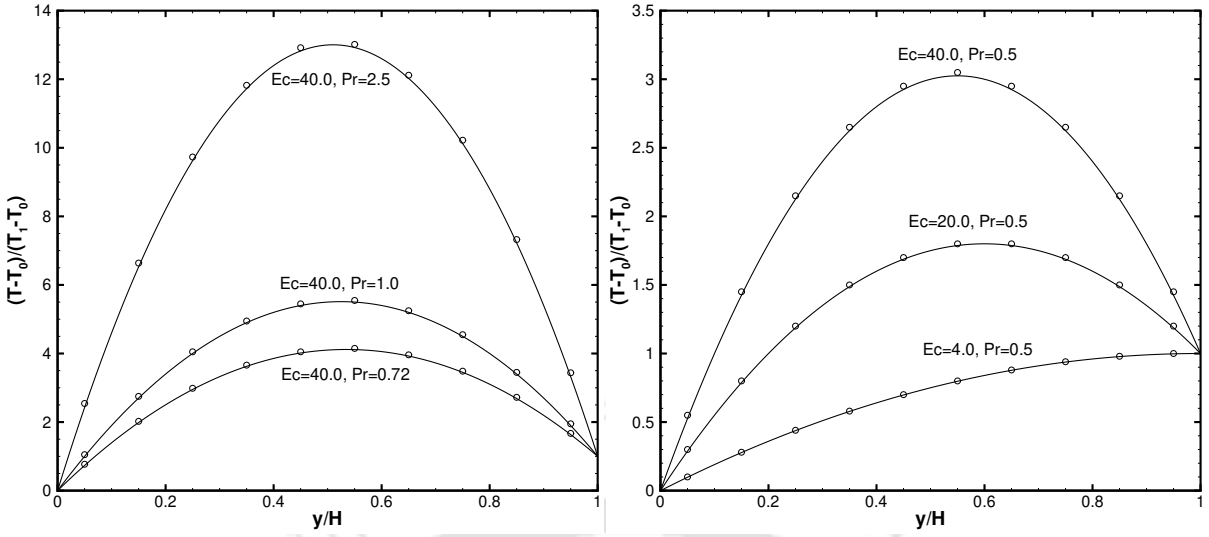

(a) Ec = 40.0 and Pr = 0.72, 1.0, 2.5 **(b)** Pr = 0.5 and Ec = 4.0, 20.0, 40.0

Figure 5.2. $(T - T_0)/(T_1 - T_0)$ vs y/H plots for near incompressible Couette flow with $M = 0.1$. The solid line is the analytic solution given by (5.2.1) and the circles show the numerically simulated result.

the order of numerical viscosity μ_{num} in FLKS scheme is estimated as

$$\mu_{num} \sim p\Delta t. \tag{5.2.3}$$

Now the condition $\Delta t << \tau$ gives $p\Delta t << p\tau$ or $\mu_{num} << \mu$. So FLKS scheme will provide accurate Navier-Stokes solution for $\epsilon = \frac{\mu_{num}}{\mu} << 1$. We now give an expression of ϵ in terms of the parameters used in the calculation here. We have

$$\epsilon = \frac{\mu_{num}}{\mu} \approx \frac{p\Delta t}{\mu} = \frac{\rho \mathrm{R} T \Delta t}{\mu}. \tag{5.2.4}$$

Now estimating T by T_0 and then using the relation $M = \frac{U}{\sqrt{\gamma \mathrm{R} T_0}}$, we get

$$\epsilon \approx \frac{\rho U^2 \Delta t}{\gamma \mu M^2}. \tag{5.2.5}$$

For the parameters ρ, U, Δt, γ, μ and M used in the test case here, equation (5.2.5) gives $\epsilon = 0.000386$ which is much smaller than 1.0 and therefore, FLKS scheme gives excellent numerical solution. We note that if the parameters are fixed in a way such that $\epsilon << 1$ is not satisfied, then the only variable Δt is the one which can be made sufficiently small to satisfy the condition. In such a case the steady state calculation will be highly time consuming.

5.2.2 Compressible Couette flow

This Couette flow test involves a large Mach number M based on the upper wall temperature and velocity. In this case compressibility effect manifests and the u-velocity profile is not linear any more. As in the work of Xu [43], $\mu \sim T$ and adiabatic lower wall condition is taken. An analytic solution for u-velocity profile as given below, is available in this situation as mentioned in Xu [43]

$$\frac{\tau_w y}{\mu_\infty U} = \frac{u}{U} + \Pr \frac{\gamma - 1}{2} M_\infty^2 \left[\frac{u}{U} - \frac{1}{3} \left(\frac{u}{U} \right)^3 \right]. \tag{5.2.6}$$

Here τ_w is the shear stress at the upper wall, μ_∞ is the viscosity coefficient corresponding to the upper wall temperature T_∞, and M_∞ is the Mach number based on upper wall velocity U.

This problem is solved on a $[0,1] \times [0,1]$ computational domain with 20×20 Cartesian grid. We set $M_\infty = 3.0$, $U = 1.0$, $\Pr = 2/3$ and $\mu = \mu_\infty \frac{T}{T_\infty}$, and use $\mu_\infty = 0.005$ and a CFL number of 0.5. The domain is initialized with $\rho = 1.0$, $u = Uy$, $v = 0$ and $T = T_\infty y$. The u-velocity profile obtained with the FLKS scheme using Van Leer limiter is shown in Figure 5.3. The

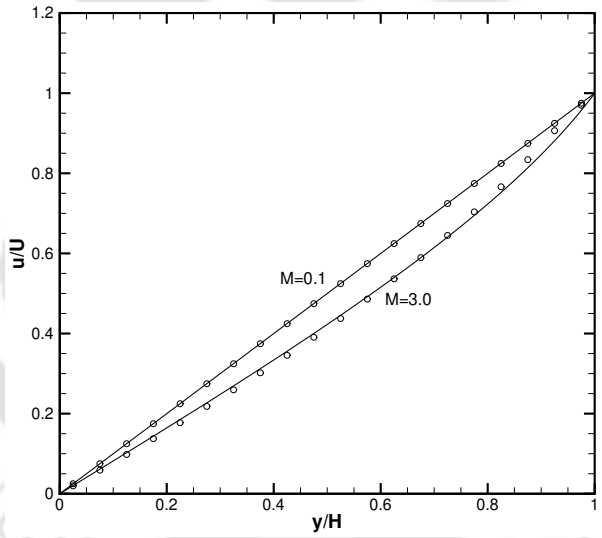

Figure 5.3. u/U vs y/H (H is the width of the domain which is 1.0) plots for compressible Couette flow with $M = 3.0$ and $M = 0.1$. The solid line is the analytic solution given by (5.2.6) and the circles show the numerically simulated result.

numerical solution is close to the analytic solution. The incompressible linear case of $M = 0.1$ is also shown to get a relative view of the compressibility effect when the Mach number goes to 3.0.

As in the previous test case of near incompressible Couette flow we can again give an estimate of ϵ based on equation (5.2.5). Taking $\mu = \mu_\infty$, $M = M_\infty$, ρ the initial value 1.0 and U the upper wall velocity, we get $\epsilon = 0.31746$. This value is below 1.0 but not too far from it as is

needed for a good numerical solution. In spite of this the produced result does not deviate much from the analytic result.

5.2.3 Laminar boundary layer flow

This test involves a laminar boundary layer with Mach number $M = 0.15$ and Reynolds number $Re = 2000$. A computational domain $[0, 32] \times [0, 12]$ is taken with a 60×60 Cartesian grid. The flat plate length is 24 units from $x = 8$ to $x = 32$ at the bottom edge of the computational domain. A flow with $\rho = 1.0$, $u = U = 0.3$, $v = V = 0$ and $M = 0.15$ is continuously fed from the left end of the domain. At the right edge of the domain simple extrapolation from the inside is done. No-slip boundary condition is applied at the plate. The flow inside the domain is initialized with the inflow condition. We take $\gamma = 1.4$, R = 287.0 and Pr = 0.72. Figure 5.4

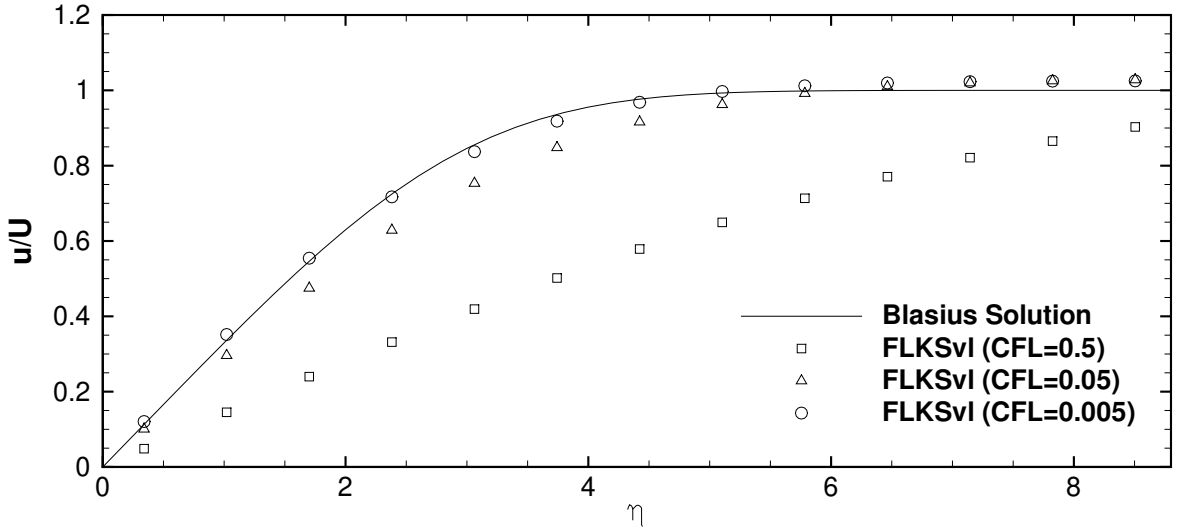

Figure 5.4. u/U vs η plot for laminar boundary layer flow with $M = 0.15$ and $Re = 2000$. The solid line is the Blasius solution. The circles, squares and triangles represent the numerical solution using FLKS scheme with Van Leer limiter for three different CFL numbers.

shows the variation of u/U with $\eta = y\sqrt{\frac{U\rho}{\mu x}}$. The results obtained by FLKS scheme using three different CFL numbers 0.5, 0.05 and 0.005 are compared with the Blasius solution. It is clear that as CFL value is reduced the effect of numerical dissipation in FLKS scheme reduces and the numerical solution goes gradually closer to the Blasius solution. This can further be explained using the equation (5.2.5). We have

$$Re = \frac{\rho U L}{\mu}$$

where L is the length of the flat plate. Expressing μ in terms of Re and putting in (5.2.5) gives

$$\epsilon = \frac{U\Delta t Re}{\gamma M^2 L}. \tag{5.2.7}$$

This expression gives $\epsilon = 39.7$, 3.97 and 0.397 for CFL values of 0.5, 0.05 and 0.005, respectively. This shows once again that a smaller Δt results in a lower numerical viscosity and hence a better Navier-Stokes solution in this case.

5.3 Discretization of the Navier-Stokes Equations Using Dimensional Splitting Combined with Chapman-Enskog Procedure

For extending the FLKS scheme to Navier-Stokes equations (2.6.1) we split it into two parts,

$$\frac{\partial \mathbf{U}}{\partial t} + \frac{\partial \mathbf{FX}}{\partial x} = \frac{\partial \mathbf{FX}_v}{\partial x} \tag{5.3.1a}$$

$$\frac{\partial \mathbf{U}}{\partial t} + \frac{\partial \mathbf{FY}}{\partial y} = \frac{\partial \mathbf{FY}_v}{\partial y} \tag{5.3.1b}$$

as is done for dimensional splitting for the Euler equations (2.4.1), where (5.3.1a) and (5.3.1b) are solved in x- and y-sweeps, respectively. Now the 2D Boltzmann equation is

$$\frac{\partial f}{\partial t} + v_1\frac{\partial f}{\partial x} + v_2\frac{\partial f}{\partial y} = \left(\frac{\partial f}{\partial t}\right)_{coll}, \tag{5.3.2}$$

where $\left(\frac{\partial f}{\partial t}\right)_{coll}$ is the collision term. Replacing the collision term by the BGK collision model [4] gives the BGK equation

$$\frac{\partial f}{\partial t} + v_1\frac{\partial f}{\partial x} + v_2\frac{\partial f}{\partial y} = -\frac{f - F}{\tau}, \tag{5.3.3}$$

where F is the local Maxwellian given by (2.5.2), and τ is the particle collision time. As already discussed in Chapter 2, the 2D Navier-Stokes equations can be obtained by taking the $\boldsymbol{\Psi}$-moment of equation (5.3.3) with $\boldsymbol{\Psi}$ given by equation (2.5.3) keeping the first two terms of the Chapman-Enskog expansion of the velocity distribution function f, i.e.,

$$\begin{aligned} f &= F - \tau\left(\frac{\partial F}{\partial t} + v_1\frac{\partial F}{\partial x} + v_2\frac{\partial F}{\partial y}\right) \\ &= F - \tau(DF) \end{aligned} \tag{5.3.4}$$

or,

$$
\begin{aligned}
f = F\Bigg[1 - \tau\Bigg[&(v_1-u)[\beta\{(v_1-u)^2+(v_2-v)^2+I\xi\}-3]\frac{\partial(lnT)}{\partial x}\\
&+(v_2-v)[\beta\{(v_1-u)^2+(v_2-v)^2+I\xi\}-3]\frac{\partial(lnT)}{\partial y}\\
&+\beta\left\{\frac{2\gamma-3}{\beta}+(3-\gamma)(v_1-u)^2-(\gamma-1)(v_2-v)^2-(\gamma-1)I\xi\right\}\frac{\partial u}{\partial x}\\
&+\beta\left\{\frac{2\gamma-3}{\beta}+(3-\gamma)(v_2-v)^2-(\gamma-1)(v_1-u)^2-(\gamma-1)I\xi\right\}\frac{\partial v}{\partial y}\\
&+2\beta(v_1-u)(v_2-v)\left(\frac{\partial u}{\partial y}+\frac{\partial v}{\partial x}\right)\Bigg]\Bigg],
\end{aligned}
\tag{5.3.5}
$$

where $\xi = \frac{2(\gamma-1)}{2-\gamma}$. We now split equation (5.3.3) into two parts as

$$
\frac{\partial f}{\partial t} + v_1\frac{\partial f}{\partial x} = -\frac{f-F}{\tau}, \tag{5.3.6a}
$$

$$
\frac{\partial f}{\partial t} + v_2\frac{\partial f}{\partial y} = -\frac{f-F}{\tau}. \tag{5.3.6b}
$$

Now the $\boldsymbol{\Psi}$-moments of equations (5.3.6a) and (5.3.6b) with f given by (5.3.4) give

$$
\begin{aligned}
&\frac{\partial}{\partial t}\left\{\int_0^\infty\int_{-\infty}^\infty\int_{-\infty}^\infty \boldsymbol{\Psi}F dv_1dv_2dI - \tau\int_0^\infty\int_{-\infty}^\infty\int_{-\infty}^\infty \boldsymbol{\Psi}(DF)dv_1dv_2dI\right\}\\
&+\frac{\partial}{\partial x}\left\{\int_0^\infty\int_{-\infty}^\infty\int_{-\infty}^\infty \boldsymbol{\Psi}v_1F dv_1dv_2dI - \tau\int_0^\infty\int_{-\infty}^\infty\int_{-\infty}^\infty \boldsymbol{\Psi}v_1(DF)dv_1dv_2dI\right\}\\
&=-\int_0^\infty\int_{-\infty}^\infty\int_{-\infty}^\infty \boldsymbol{\Psi}\frac{f-F}{\tau}dv_1dv_2dI
\end{aligned}
\tag{5.3.7a}
$$

and

$$
\begin{aligned}
&\frac{\partial}{\partial t}\left\{\int_0^\infty\int_{-\infty}^\infty\int_{-\infty}^\infty \boldsymbol{\Psi}F dv_1dv_2dI - \tau\int_0^\infty\int_{-\infty}^\infty\int_{-\infty}^\infty \boldsymbol{\Psi}(DF)dv_1dv_2dI\right\}\\
&+\frac{\partial}{\partial y}\left\{\int_0^\infty\int_{-\infty}^\infty\int_{-\infty}^\infty \boldsymbol{\Psi}v_2F dv_1dv_2dI - \tau\int_0^\infty\int_{-\infty}^\infty\int_{-\infty}^\infty \boldsymbol{\Psi}v_2(DF)dv_1dv_2dI\right\}\\
&=-\int_0^\infty\int_{-\infty}^\infty\int_{-\infty}^\infty \boldsymbol{\Psi}\frac{f-F}{\tau}dv_1dv_2dI.
\end{aligned}
\tag{5.3.7b}
$$

Using the compatibility conditions $\int_0^\infty\int_{-\infty}^\infty\int_{-\infty}^\infty \boldsymbol{\Psi}\frac{f-F}{\tau}dv_1dv_2dI = 0$ and $\int_0^\infty\int_{-\infty}^\infty\int_{-\infty}^\infty \boldsymbol{\Psi}(DF)dv_1dv_2dI = 0$ with little rearrangement gives

$$
\begin{aligned}
&\frac{\partial}{\partial t}\left\{\int_0^\infty\int_{-\infty}^\infty\int_{-\infty}^\infty \boldsymbol{\Psi}F dv_1dv_2dI\right\} + \frac{\partial}{\partial x}\left\{\int_0^\infty\int_{-\infty}^\infty\int_{-\infty}^\infty \boldsymbol{\Psi}v_1F dv_1dv_2dI\right\}\\
&=\frac{\partial}{\partial x}\left\{\tau\int_0^\infty\int_{-\infty}^\infty\int_{-\infty}^\infty \boldsymbol{\Psi}v_1(DF)dv_1dv_2dI\right\}
\end{aligned}
\tag{5.3.8a}
$$

and

$$\begin{aligned}&\frac{\partial}{\partial t}\left\{\int_0^\infty\int_{-\infty}^\infty\int_{-\infty}^\infty \boldsymbol{\Psi} F dv_1 dv_2 dI\right\}+\frac{\partial}{\partial y}\left\{\int_0^\infty\int_{-\infty}^\infty\int_{-\infty}^\infty \boldsymbol{\Psi} v_2 F dv_1 dv_2 dI\right\}\\&=\frac{\partial}{\partial y}\left\{\tau\int_0^\infty\int_{-\infty}^\infty\int_{-\infty}^\infty \boldsymbol{\Psi} v_2 (DF) dv_1 dv_2 dI\right\}\end{aligned} \tag{5.3.8b}$$

Clearly, equations (5.3.8a) and (5.3.8b) reproduce the left hand side Euler parts of equations (5.3.1a) and (5.3.1b), respectively, with the right hand side viscous fluxes given by

$$\mathbf{FX}_v=\tau\int_0^\infty\int_{-\infty}^\infty\int_{-\infty}^\infty \boldsymbol{\Psi} v_1 (DF) dv_1 dv_2 dI=\tau p\begin{bmatrix}0\\(3-\gamma)\frac{\partial u}{\partial x}-(\gamma-1)\frac{\partial v}{\partial y}\\\frac{\partial u}{\partial y}+\frac{\partial v}{\partial x}\\\left\{(3-\gamma)\frac{\partial u}{\partial x}-(\gamma-1)\frac{\partial v}{\partial y}\right\}u+\left(\frac{\partial u}{\partial y}+\frac{\partial v}{\partial x}\right)v+\frac{\gamma R}{\gamma-1}\frac{\partial T}{\partial x}\end{bmatrix} \tag{5.3.9a}$$

$$\mathbf{FY}_v=\tau\int_0^\infty\int_{-\infty}^\infty\int_{-\infty}^\infty \boldsymbol{\Psi} v_2 (DF) dv_1 dv_2 dI=\tau p\begin{bmatrix}0\\\frac{\partial u}{\partial y}+\frac{\partial v}{\partial x}\\(3-\gamma)\frac{\partial v}{\partial y}-(\gamma-1)\frac{\partial u}{\partial x}\\\left\{(3-\gamma)\frac{\partial v}{\partial y}-(\gamma-1)\frac{\partial u}{\partial x}\right\}v+\left(\frac{\partial u}{\partial y}+\frac{\partial v}{\partial x}\right)u+\frac{\gamma R}{\gamma-1}\frac{\partial T}{\partial y}\end{bmatrix}, \tag{5.3.9b}$$

where we arrive at the well-known result $\mu=\tau p$ as the coefficient of dynamic viscosity and Prandtl number $\mathrm{Pr}=1$.

Now for x-sweep a discretization scheme for equation (5.3.1a) can be written as

$$\frac{\mathbf{U}_{i,j}^{n+1}-\mathbf{U}_{i,j}^{n}}{\Delta t}+\frac{\hat{\mathbf{fx}}_{i+\frac{1}{2},j}^{n}-\hat{\mathbf{fx}}_{i-\frac{1}{2},j}^{n}}{\Delta x}=\frac{\hat{\mathbf{fx}}_{vi+\frac{1}{2},j}^{n}-\hat{\mathbf{fx}}_{vi-\frac{1}{2},j}^{n}}{\Delta x} \tag{5.3.10}$$

where $\hat{\mathbf{fx}}_{i+\frac{1}{2},j}^{n}$ and $\hat{\mathbf{fx}}_{vi+\frac{1}{2},j}^{n}$ are time averaged conservative fluxes for the inviscid and viscous parts, respectively, at cell face $(i+\frac{1}{2},j)$ of cell (i,j). Equation (5.3.10) can be written in a simplified standard form

$$\mathbf{U}_{i,j}^{n+1}=\mathbf{U}_{i,j}^{n}-\lambda_1\left[\hat{\boldsymbol{fx}}_{i+\frac{1}{2},j}^{n}-\hat{\boldsymbol{fx}}_{i-\frac{1}{2},j}^{n}\right] \tag{5.3.11}$$

where

$$\hat{\boldsymbol{fx}}_{i+\frac{1}{2},j}^{n}=\hat{\mathbf{fx}}_{i+\frac{1}{2},j}^{n}-\hat{\mathbf{fx}}_{vi+\frac{1}{2},j}^{n}. \tag{5.3.12}$$

The flux $\hat{\mathbf{fx}}^{n}_{i+\frac{1}{2},j}$ is obtained from the FLKS scheme (4.1.3a) for the x-direction split Euler equations (4.1.1a) as

$$\begin{aligned}\hat{\mathbf{fx}}^{n}_{i+\frac{1}{2},j} &= \left(\mathbf{FX}^{+^n}_{i,j} + \mathbf{FX}^{-^n}_{i+1,j}\right) \\ &+ \frac{1}{2}\text{avg}\left(\left(\mathbf{FX}^{+^n}_{i+1,j} - \mathbf{FX}^{+^n}_{i,j}\right), \left(\mathbf{FX}^{+^n}_{i,j} - \mathbf{FX}^{+^n}_{i-1,j}\right)\right) \\ &- \frac{1}{2}\text{avg}\left(\left(\mathbf{FX}^{-^n}_{i+2,j} - \mathbf{FX}^{-^n}_{i+1,j}\right), \left(\mathbf{FX}^{-^n}_{i+1,j} - \mathbf{FX}^{-^n}_{i,j}\right)\right) \\ &- \frac{\lambda_1}{2}\text{avg}\left(\left(\mathbf{GX}^{+^n}_{i+1,j} - \mathbf{GX}^{+^n}_{i,j}\right), \left(\mathbf{GX}^{+^n}_{i,j} - \mathbf{GX}^{+^n}_{i-1,j}\right)\right) \\ &- \frac{\lambda_1}{2}\text{avg}\left(\left(\mathbf{GX}^{-^n}_{i+2,j} - \mathbf{GX}^{-^n}_{i+1,j}\right), \left(\mathbf{GX}^{-^n}_{i+1,j} - \mathbf{GX}^{-^n}_{i,j}\right)\right).\end{aligned} \tag{5.3.13}$$

Now the viscous conservative flux $\hat{\mathbf{fx}}^{n}_{v_{i+\frac{1}{2},j}}$ can be obtained as follows:

$$\begin{aligned}\hat{\mathbf{fx}}^{n}_{v_{i+\frac{1}{2},j}} &= \hat{\mathbf{fx}}^{+^n}_{v_{i+\frac{1}{2},j}} + \hat{\mathbf{fx}}^{-^n}_{v_{i+\frac{1}{2},j}} \\ &= \mathbf{FX}^{+^n}_{v_{i,j}} + \mathbf{FX}^{-^n}_{v_{i+1,j}}\end{aligned} \tag{5.3.14}$$

where the positive and negative split viscous fluxes $\mathbf{FX}^{+^n}_{v_{i,j}}$ and $\mathbf{FX}^{-^n}_{v_{i+1,j}}$ can be obtained by using relation (5.3.9a) as described in Appendix B. Now inserting expressions for $\hat{\mathbf{fx}}^{n}_{i+\frac{1}{2},j}$ and $\hat{\mathbf{fx}}^{n}_{v_{i+\frac{1}{2},j}}$ from equations (5.3.13) and (5.3.14) into (5.3.12) gives

$$\begin{aligned}\hat{\boldsymbol{fx}}^{n}_{i+\frac{1}{2},j} &= \left\{\left(\mathbf{FX}^{+^n}_{i,j} - \mathbf{FX}^{+^n}_{v_{i,j}}\right) + \left(\mathbf{FX}^{-^n}_{i+1,j} - \mathbf{FX}^{-^n}_{v_{i+1,j}}\right)\right\} \\ &+ \frac{1}{2}\text{avg}\left(\left(\mathbf{FX}^{+^n}_{i+1,j} - \mathbf{FX}^{+^n}_{i,j}\right), \left(\mathbf{FX}^{+^n}_{i,j} - \mathbf{FX}^{+^n}_{i-1,j}\right)\right) \\ &- \frac{1}{2}\text{avg}\left(\left(\mathbf{FX}^{-^n}_{i+2,j} - \mathbf{FX}^{-^n}_{i+1,j}\right), \left(\mathbf{FX}^{-^n}_{i+1,j} - \mathbf{FX}^{-^n}_{i,j}\right)\right) \\ &- \frac{\lambda_1}{2}\text{avg}\left(\left(\mathbf{GX}^{+^n}_{i+1,j} - \mathbf{GX}^{+^n}_{i,j}\right), \left(\mathbf{GX}^{+^n}_{i,j} - \mathbf{GX}^{+^n}_{i-1,j}\right)\right) \\ &- \frac{\lambda_1}{2}\text{avg}\left(\left(\mathbf{GX}^{-^n}_{i+2,j} - \mathbf{GX}^{-^n}_{i+1,j}\right), \left(\mathbf{GX}^{-^n}_{i+1,j} - \mathbf{GX}^{-^n}_{i,j}\right)\right).\end{aligned} \tag{5.3.15}$$

Thus x-sweep for the solution of the 2D Navier-Stokes equations can be performed by using equation (5.3.11) where the conservative flux $\hat{\boldsymbol{fx}}^{n}_{i+\frac{1}{2},j}$ is given by (5.3.15). Similarly in y-sweep equation (5.3.1b) is solved using

$$\mathbf{U}^{n+1}_{i,j} = \mathbf{U}^{n}_{i,j} - \lambda_2\left[\hat{\boldsymbol{fy}}^{n}_{i,j+\frac{1}{2}} - \hat{\boldsymbol{fy}}^{n}_{i,j-\frac{1}{2}}\right] \tag{5.3.16}$$

where

$$\begin{aligned}\hat{\boldsymbol{fy}}^{n}_{i,j+\frac{1}{2}} &= \left\{\left(\mathbf{FY}^{+^n}_{i,j} - \mathbf{FY}_{v}{}^{+^n}_{i,j}\right) + \left(\mathbf{FY}^{-^n}_{i,j+1} - \mathbf{FY}_{v}{}^{-^n}_{i,j+1}\right)\right\} \\ &+ \frac{1}{2}\text{avg}\left(\left(\mathbf{FY}^{+^n}_{i,j+1} - \mathbf{FY}^{+^n}_{i,j}\right), \left(\mathbf{FY}^{+^n}_{i,j} - \mathbf{FY}^{+^n}_{i,j-1}\right)\right) \\ &- \frac{1}{2}\text{avg}\left(\left(\mathbf{FY}^{-^n}_{i,j+2} - \mathbf{FY}^{-^n}_{i,j+1}\right), \left(\mathbf{FY}^{-^n}_{i,j+1} - \mathbf{FY}^{-^n}_{i,j}\right)\right) \\ &- \frac{\lambda_2}{2}\text{avg}\left(\left(\mathbf{GY}^{+^n}_{i,j+1} - \mathbf{GY}^{+^n}_{i,j}\right), \left(\mathbf{GY}^{+^n}_{i,j} - \mathbf{GY}^{+^n}_{i,j-1}\right)\right) \\ &- \frac{\lambda_2}{2}\text{avg}\left(\left(\mathbf{GY}^{-^n}_{i,j+2} - \mathbf{GY}^{-^n}_{i,j+1}\right), \left(\mathbf{GY}^{-^n}_{i,j+1} - \mathbf{GY}^{-^n}_{i,j}\right)\right).\end{aligned} \tag{5.3.17}$$

Here the expressions for $\mathbf{FY}_{v}{}^{+^n}_{i,j}$ and $\mathbf{FY}_{v}{}^{-^n}_{i,j+1}$ are obtained as given in Appendix B. Also the TVD criterion gets relaxed by multiplying $\frac{\lambda_1}{2}$ and $\frac{\lambda_2}{2}$ terms in equations (5.3.15) and (5.3.17) by b (< 1.0) as is the case with FLKS scheme for 1D and 2D Euler equations. The format of the conservative flux for the Navier-Stokes equations also remains the same as that for the Euler equations and therefore, the same Euler code can be used with little modification for Navier-Stokes solution.

One final issue that needs to be resolved is the problem of unit Prandtl number. We follow the simple fix given in Tang [46], where the temperature gradient terms $\frac{\gamma R}{\gamma-1}\frac{\partial T}{\partial x}$ and $\frac{\gamma R}{\gamma-1}\frac{\partial T}{\partial y}$ in equations (5.3.9a) and (5.3.9b) are replaced by $\frac{\gamma R}{(\gamma-1)\text{Pr}}\frac{\partial T}{\partial x}$ and $\frac{\gamma R}{(\gamma-1)\text{Pr}}\frac{\partial T}{\partial y}$, respectively. The same temperature gradients appearing in the viscous split fluxes given in Appendix B are also modified similarly.

5.4 Results and Discussion for Chapman-Enskog Procedure Based Scheme

The same three test cases taken in Section 5.2 are considered for evaluating the performance of this new version of FLKS scheme as a Navier-Stokes solver.

5.4.1 Near incompressible Couette flow

We simulate this flow by taking a computational domain of length $L = 1.0$ and width $H = 1.0$. The specific heat ratio $\gamma = 1.4$ and the specific gas constant R = 287.0 are taken. The Mach number $M = \frac{U}{\sqrt{\gamma \text{R} T_0}}$ is fixed at 0.1 to satisfy the incompressibility criterion. At the top and bottom walls isothermal no-slip boundary condition is implemented. At the left and right ends periodic boundary treatment is done. The simulation is done on a 10×10 Cartesian grid. The computational domain is initialized with $\rho = 1.0$, $u = U$, $v = 0$ and $T = T_0$. For several combinations of Pr and Ec numbers as given in Xu [43] the results obtained with FLKS scheme

are shown in Figure 5.5. The simulated result is in very good agreement with the analytic

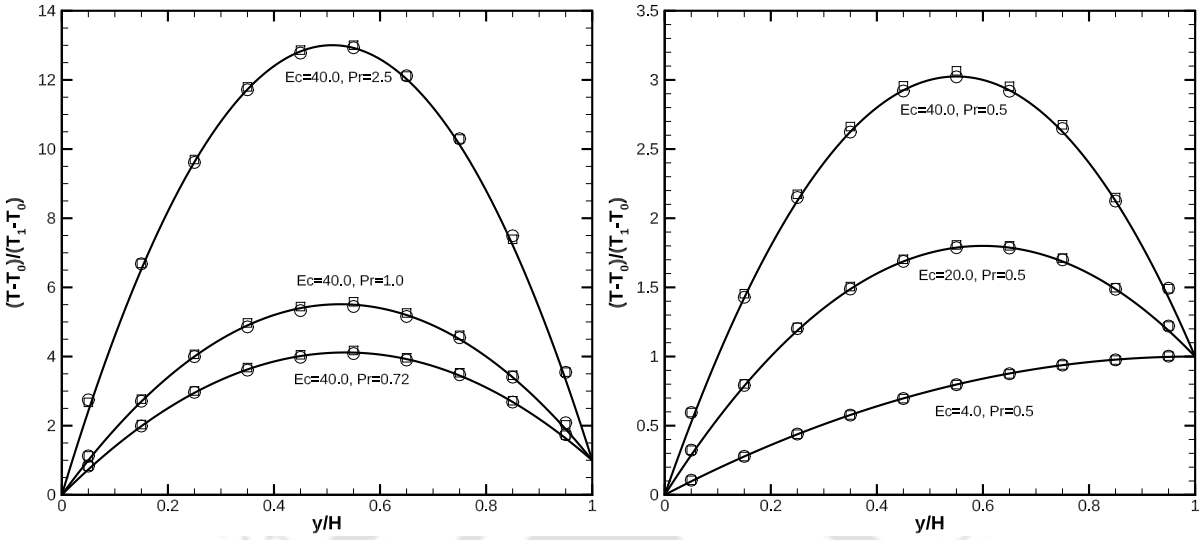

(a) Ec = 40.0 and Pr = 0.72, 1.0, 2.5 **(b)** Pr = 0.5 and Ec = 4.0, 20.0, 40.0

Figure 5.5. $(T - T_0)/(T_1 - T_0)$ vs y/H plots for near incompressible Couette flow with $M = 0.1$. The solid line is the analytic solution given by (5.2.1) and the circles and squares show the numerically simulated results for $\Delta t = 0.0013\tau$ and $\Delta t = 14.3\tau$ cases, respectively.

solution. As already described in Section 5.2, a KFVS type scheme like KFVS-NS [72] uses free transport equation with the nonequilibrium distribution function f as the initial condition. This creates a numerical collision time equal to the time-step size Δt and hence introduces numerical viscosity of the order of Δt. For an accurate Navier-Stokes solution such schemes should have the numerical viscosity much smaller than the actual physical viscosity. In other words, $\Delta t << \tau$ should be satisfied. For testing the performance of our scheme for different sizes of Δt relative to τ we have tested for the cases $\Delta t >> \tau$, $\Delta t \approx \tau$ and $\Delta t << \tau$. For estimating a representative value of τ we use the relation

$$\mu = \tau p$$

which gives,

$$\tau = \frac{\mu}{p} = \frac{\mu}{\rho \mathrm{R} T}. \tag{5.4.1}$$

Now estimating T by T_0 and then using the relation $M = \frac{U}{\sqrt{\gamma \mathrm{R} T_0}}$, we get after little manipulation

$$\tau = \frac{\mu \gamma M^2}{\rho U^2}. \tag{5.4.2}$$

In particular, we took $\Delta t = 14.3\tau$, $\Delta t = 1.3\tau$, $\Delta t = 0.0013\tau$, and many such values of Δt and every time the numerical solution was in very good agreement for all combinations of Pr and

Ec numbers as shown in Figure 5.5, where only the results for $\Delta t = 0.0013\tau$ and $\Delta t = 14.3\tau$ are shown. This clearly demonstrates that the present FLKS scheme is not restricted by the condition $\Delta t << \tau$.

5.4.2 Compressible Couette flow

This problem is solved on a $[0,1] \times [0,1]$ computational domain with 20×20 Cartesian grid. We set $M_\infty = 3.0$, $U = 1.0$, $\Pr = 2/3$ and $\mu = \mu_\infty \frac{T}{T_\infty}$, and use $\mu_\infty = 0.005$. The domain is initialized with $\rho = 1.0$, $u = Uy$, $v = 0$ and $T = T_\infty y$. The u-velocity profile obtained with the FLKS scheme is shown in Figure 5.6. The numerical solution is in good agreement with the

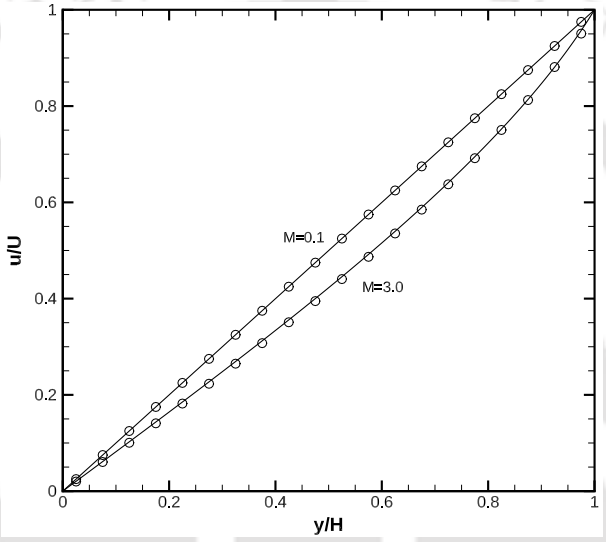

Figure 5.6. u/U vs y/H (H is the width of the domain which is 1.0) plots for compressible Couette flow with $M = 3.0$ and $M = 0.1$. The solid line is the analytic solution given by (5.2.6) and the circles show the numerically simulated result.

analytic solution. The incompressible linear case of $M = 0.1$ is also shown to get a relative view of the compressibility effect when the Mach number goes to 3.0.

5.4.3 Laminar boundary layer flow over a flat plate

A computational domain $[0, 32] \times [0, 12]$ is taken. The flat plate length is $L = 24$ units from $x = 8$ to $x = 32$ at the bottom edge of the computational domain. Two flow conditions, one with $\rho = 1.0$, $u = U = 0.3$, $v = V = 0$ and $Re = 2000$, and the other with $\rho = 1.0$, $u = U = 3.0$, $v = V = 0$ and $Re = 9000$ are considered for continuous feeding from the left end of the domain. In these two inflow conditions a representative value of τ can be estimated using relation (5.4.2) and $Re = \frac{\rho U L}{\mu}$ as

$$\tau = \frac{\gamma M^2 L}{URe}. \tag{5.4.3}$$

At the right edge of the domain simple extrapolation from the inside is done and no-slip boundary condition is applied at the plate. The flow inside the domain is initialized with the inflow condition and $\gamma = 1.4$, R = 287.0, and Pr = 0.72 are fixed. This way we get $\tau = 1.26 \times 10^{-3}$ and 2.8×10^{-5} for the $Re = 2000$ and 9000 cases, respectively. Figure 5.7 shows the variation of u/U

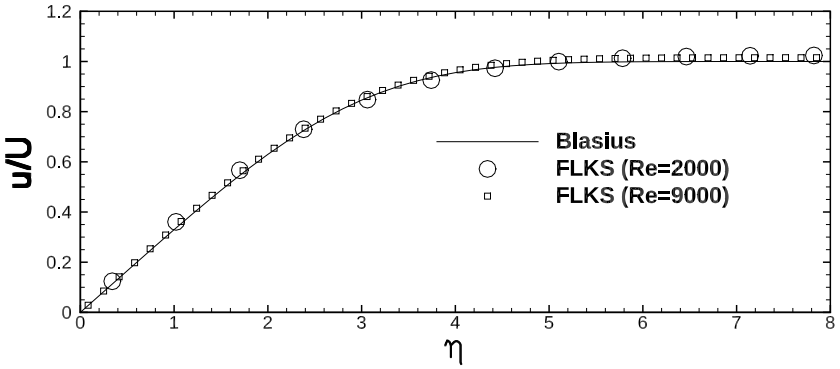

Figure 5.7. u/U vs η plot for laminar boundary layer flow with $M = 0.15$. The solid line is the Blasius solution. The circles and squares represent the numerical solution for $Re = 2000$ and 9000 cases, respectively, using FLKS scheme.

with $\eta = y\sqrt{\frac{U\rho}{\mu x}}$ at steady state obtained with the FLKS scheme using $\Delta x = 0.53, \Delta y = 0.2$ and $\Delta t = 0.08\tau$ for $Re = 2000$ case at $x = 15.2$, and using $\Delta x = 0.064, \Delta y = 0.024$ and $\Delta t = 4.3\tau$ for $Re = 9000$ case at $x = 15.9$. Both these results match well with the Blasius solution which exemplifies the capability of FLKS scheme in resolving the boundary layer solution properly.

5.5 Conclusions

This chapter proposes two different methods to extend the 2D FLKS scheme for the Euler equations to the Navier-Stokes equations. Out of the two methods, the Chapman-Enskog procedure based scheme gives accurate results independent of the size of Δt for all the cases $\Delta t >> \tau$, $\Delta t \approx \tau$ and $\Delta t << \tau$ that we have tested. The other scheme requires tweaking of the size of Δt in order to reduce the artificial viscosity in comparison to the actual viscosity. On the other hand, the Chapman-Enskog based method provides a compact formula for the conservative numerical flux as well, therefore, the same 2D Euler code can be modified easily to make it a Navier-Stokes solver. Thus, this scheme is the preferable one for a Navier-Stokes solution. Having developed a workable method based on FLKS for the Navier-Stokes solution, the next chapter proposes a procedure to implement the FLKS scheme for the Euler equations on triangular unstructured grids.

Chapter 6

2D FLKS Scheme on Triangular Unstructured Grid

Use of unstructured grid in finite volume framework to deal with complex geometries has been ubiquitous in the last few decades. This motivates the extension of FLKS scheme to unstructured grids. Researchers [33, 73] have suggested some accurate and sophisticated ways to implement a limiter-based scheme on unstructured grids which can possibly be framed in a manner to work with the FLKS scheme. However, these methodologies have not been tried in the thesis, rather a simple but approximate way to use FLKS scheme on triangular unstructured grids is proposed here. The method works well when the mesh skewness is not too high, i.e., the cells do not deviate much from an equilateral triangular shape.

6.1 The Finite Volume Formula

The integral form of the 2D Euler equations (2.4.1) is

$$\frac{d}{dt}\iiint_{CV}\mathbf{U}dV+\iint_{CS}\mathbb{F}.\mathbf{n}dA=0, \tag{6.1.1}$$

where CV stands for control volume and CS for control surface which is the boundary of CV. dV and dA are elemental control volume and control surface, respectively. $\mathbf{n}$ is the outward unit normal vector at dA. $\mathbb{F}=(\mathbf{FX},\mathbf{FY})$ is the tensor of fluxes.

A conservative discretization of equation (6.1.1) over a finite control volume gives

$$\mathbf{U}_i^{n+1} = \mathbf{U}_i^n - \frac{\Delta t}{V}\sum_{k=1}^{N} \mathbb{F}_k.\mathbf{n}_k A_k, \tag{6.1.2}$$

where N is the number of faces of the control volume or cell, V is the volume (area in 2D) of the cell, A_k is the area (length in 2D) of the k^{th} face and Δt is the time step. Also we adopt cell-centred finite volume methodology where the $\mathbf{U}$ values are stored at the cell centres of cells. A finite volume scheme gives a method to determine the value of the intercell flux $\mathbb{F}_k.\mathbf{n}_k$. Consider Figure 6.1 which shows two triangular cells ABC (denoted by L) and ABD (denoted by R) adjacent to each other which is a part of an unstructured grid. AB is the common face between cells L and R. For evaluating $\mathbb{F}.\mathbf{n}$ at the face AB for cell L, one can write

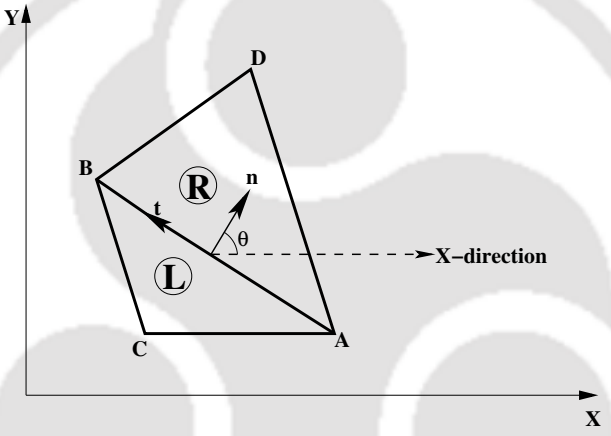

Figure 6.1. Intercell AB between the triangular cells ABC and ABD, and the rotated coordinate system $(\mathbf{n}, \mathbf{t})$.

$$\mathbb{F}.\mathbf{n} = \mathbf{FX}\cos\theta + \mathbf{FY}\sin\theta, \tag{6.1.3}$$

where $\mathbf{n} = (n_x, n_y) = (\cos\theta, \sin\theta)$. Also the Euler equations (2.4.1) are rotationally invariant [5], i.e.,

$$\mathbf{FX}(\mathbf{U})\cos\theta + \mathbf{FY}(\mathbf{U})\sin\theta = \mathbf{T}^{-1}\mathbf{FX}(\mathbf{TU}), \tag{6.1.4}$$

where $\mathbf{T}$ and $\mathbf{T}^{-1}$ are the rotation matrix and its inverse, respectively, as given below.

$$\mathbf{T} = \begin{bmatrix} 1 & 0 & 0 & 0 \\ 0 & \cos\theta & \sin\theta & 0 \\ 0 & -\sin\theta & \cos\theta & 0 \\ 0 & 0 & 0 & 1 \end{bmatrix}, \quad \mathbf{T}^{-1} = \begin{bmatrix} 1 & 0 & 0 & 0 \\ 0 & \cos\theta & -\sin\theta & 0 \\ 0 & \sin\theta & \cos\theta & 0 \\ 0 & 0 & 0 & 1 \end{bmatrix}. \tag{6.1.5}$$

We now write

$$\widetilde{\mathbf{U}} = \mathbf{T}\mathbf{U} = \begin{bmatrix} 1 & 0 & 0 & 0 \\ 0 & \cos\theta & \sin\theta & 0 \\ 0 & -\sin\theta & \cos\theta & 0 \\ 0 & 0 & 0 & 1 \end{bmatrix} \begin{bmatrix} \rho \\ \rho u \\ \rho v \\ \rho e \end{bmatrix} = \begin{bmatrix} \rho \\ \rho V_n \\ \rho V_t \\ \rho e \end{bmatrix} \quad \text{and} \quad \widetilde{\mathbf{FX}} = \mathbf{FX}(\widetilde{\mathbf{U}}) = \begin{bmatrix} \rho V_n \\ p + \rho V_n^2 \\ \rho V_n V_t \\ (p + \rho e) V_n \end{bmatrix}, \tag{6.1.6}$$

where $\widetilde{\mathbf{U}}$ is the vector of rotated conserved variables and

$$V_n = u\cos\theta + v\sin\theta \quad \text{and} \quad V_t = -u\sin\theta + v\cos\theta$$

are the fluid velocity components at the face AB in normal and tangential directions, respectively. The finite volume formula (6.1.2) using equations (6.1.3) and (6.1.4) then becomes

$$\mathbf{U}_i^{n+1} = \mathbf{U}_i^n - \frac{\Delta t}{V} \sum_{k=1}^{N} \mathbf{T}_k^{-1} \widetilde{\mathbf{FX}}_k A_k \tag{6.1.7}$$

6.2 Determination of Intercell Flux in the Finite Volume Formula

The Euler equations in the rotated frame $(\mathbf{n}, \mathbf{t})$ become the augmented one-dimensional equations [5] given by

$$\frac{\partial \widetilde{\mathbf{U}}}{\partial t} + \frac{\partial \widetilde{\mathbf{FX}}}{\partial \widetilde{x}} = 0, \tag{6.2.1}$$

where $\widetilde{x}$ is the rotated x-direction which is along the unit normal vector $\mathbf{n}$ to the face AB (the new rotated y-direction is along the unit vector $\mathbf{t}$, tangential to AB). The numerical flux $\widetilde{\mathbf{FX}}$ using FLKS scheme can be constructed for this augmented equation (6.2.1) which in turn can be used in equation (6.1.7).

The FLKS scheme for augmented 1D Euler equations in x and y-directions are already known by equation (4.1.3). Following similar procedure used in arriving at (4.1.3), i.e., first discretizing a 1D collisionless Boltzmann equation in direction $\mathbf{n}$ by Sweby's flux-limited method [26] and then taking $\boldsymbol{\Psi}$-moment by **Method** 1, gives FLKS scheme for (6.2.1) in conservation form as

$$\widetilde{\mathbf{U}}_i^{n+1} = \widetilde{\mathbf{U}}_i^n - \lambda \left[\widetilde{\mathbf{f}}_{i+\frac{1}{2}}^n - \widetilde{\mathbf{f}}_{i-\frac{1}{2}}^n \right], \tag{6.2.2a}$$

where

$$\begin{aligned}\widetilde{\mathbf{f}}^{n}_{i+\frac{1}{2}} &= \left(\widetilde{\mathbf{FX}}_i^{+^n} + \widetilde{\mathbf{FX}}_{i+1}^{-^n}\right) \\ &+ \frac{1}{2}\text{avg}\left(\left(\widetilde{\mathbf{FX}}_{i+1}^{+^n} - \widetilde{\mathbf{FX}}_i^{+^n}\right), \left(\widetilde{\mathbf{FX}}_i^{+^n} - \widetilde{\mathbf{FX}}_{i-1}^{+^n}\right)\right) \\ &- \frac{1}{2}\text{avg}\left(\left(\widetilde{\mathbf{FX}}_{i+2}^{-^n} - \widetilde{\mathbf{FX}}_{i+1}^{-^n}\right), \left(\widetilde{\mathbf{FX}}_{i+1}^{-^n} - \widetilde{\mathbf{FX}}_i^{-^n}\right)\right) \\ &- \frac{\lambda}{2}\text{avg}\left(\left(\widetilde{\mathbf{GX}}_{i+1}^{+^n} - \widetilde{\mathbf{GX}}_i^{+^n}\right), \left(\widetilde{\mathbf{GX}}_i^{+^n} - \widetilde{\mathbf{GX}}_{i-1}^{+^n}\right)\right) \\ &- \frac{\lambda}{2}\text{avg}\left(\left(\widetilde{\mathbf{GX}}_{i+2}^{-^n} - \widetilde{\mathbf{GX}}_{i+1}^{-^n}\right), \left(\widetilde{\mathbf{GX}}_{i+1}^{-^n} - \widetilde{\mathbf{GX}}_i^{-^n}\right)\right)\end{aligned} \tag{6.2.2b}$$

is the time averaged numerical flux in time Δt from time step n to $n+1$ at the cell interface position $\widetilde{x}_{i+\frac{1}{2}}$. Here a 1D spacial domain is assumed with cell $\left[\widetilde{x}_{i-\frac{1}{2}}, \widetilde{x}_{i+\frac{1}{2}}\right]$ as the i^{th} cell with uniform $\Delta\widetilde{x} = \widetilde{x}_{i+\frac{1}{2}} - \widetilde{x}_{i-\frac{1}{2}}$. Here

$$\lambda = \frac{\Delta t}{\Delta \widetilde{x}} \tag{6.2.3}$$

and all $\widetilde{\mathbf{FX}}^{\pm}$ and $\widetilde{\mathbf{GX}}^{\pm}$ are obtained by

$$\begin{aligned}\widetilde{\mathbf{FX}}^{\pm} &= \begin{bmatrix}\widetilde{FX}^{(1)^{\pm}} \\ \widetilde{FX}^{(2)^{\pm}} \\ \widetilde{FX}^{(3)^{\pm}} \\ \widetilde{FX}^{(4)^{\pm}}\end{bmatrix} = \left\langle \boldsymbol{\Psi}_n, \frac{v_n \pm |v_n|}{2} F_n \right\rangle \\ &= \begin{bmatrix} \rho V_n \\ p + \rho V_n^2 \\ \rho V_n V_t \\ \left\{\frac{\gamma}{\gamma-1}p + \frac{1}{2}\rho(V_n^2 + V_t^2)\right\} V_n \end{bmatrix} X_n^{\pm} \\ &\pm \begin{bmatrix} \rho \\ \rho V_n \\ \rho V_t \\ \frac{\gamma+1}{2(\gamma-1)}p + \frac{1}{2}\rho(V_n^2 + V_t^2) \end{bmatrix} Y_n\end{aligned} \tag{6.2.4a}$$

and

$$\widetilde{\mathbf{GX}}^{\pm} = \begin{bmatrix} \widetilde{GX}^{(1)^{\pm}} \\ \widetilde{GX}^{(2)^{\pm}} \\ \widetilde{GX}^{(3)^{\pm}} \\ \widetilde{GX}^{(4)^{\pm}} \end{bmatrix} = \left\langle \boldsymbol{\Psi}_n, v_n \frac{v_n \pm |v_n|}{2} F_n \right\rangle$$

$$= \begin{bmatrix} p + \rho V_n^2 \\ (3p + \rho V_n^2) V_n \\ (p + \rho V_n^2) V_t \\ \frac{\gamma}{\gamma-1}\frac{p^2}{\rho} + \frac{5\gamma-3}{2(\gamma-1)} p V_n^2 + \frac{1}{2} p V_t^2 + \frac{\rho V_n^2}{2}(V_n^2 + V_t^2) \end{bmatrix} X_n^{\pm}$$

$$\pm \begin{bmatrix} \rho V_n \\ 2p + \rho V_n^2 \\ \rho V_n V_t \\ \frac{2\gamma-1}{\gamma-1} p V_n + \frac{\rho V_n}{2}(V_n^2 + V_t^2) \end{bmatrix} Y_n, \tag{6.2.4b}$$

where

$$F_n = \frac{\rho}{I_0}\left(\frac{\beta}{\pi}\right) \exp\left[-\beta\left\{(v_n - V_n)^2 + (v_t - V_t)^2\right\} - \frac{I}{I_0}\right] \quad \text{and} \quad \boldsymbol{\Psi}_n = \begin{bmatrix} 1 \\ v_n \\ v_t \\ I + \frac{v_n^2 + v_t^2}{2} \end{bmatrix} \tag{6.2.5}$$

with molecular velocity components v_n and v_t in $\mathbf{n}$ and $\mathbf{t}$ directions, respectively, and

$$X_n^{\pm} = \frac{1 \pm \mathrm{erf}(S_n)}{2}, \quad Y_n = \frac{e^{-S_n^2}}{2\sqrt{\pi\beta}}, \quad S_n = V_n\sqrt{\beta}. \tag{6.2.6}$$

This scheme (6.2.2) for the augmented Euler equations (6.2.1) applies to a 1D grid along $\mathbf{n}$ (see Figure 6.2). In order to use the conservative flux (6.2.2b) in the formula (6.1.7) for the term $\widetilde{\mathbf{FX}}_k$, we need data values at four grid positions $\widetilde{x}_{i-1}, \widetilde{x}_i, \widetilde{x}_{i+1}$ and $\widetilde{x}_{i+2}$ along a 1D grid normal to k^{th} face and passing through the centre of the face where the $\widetilde{x}_{i+\frac{1}{2}}$ position is at the face as demonstrated in Figure 6.2 (assuming face AB as the k^{th} face). Let us change the name for the grid positions $\widetilde{x}_{i-1}, \widetilde{x}_i, \widetilde{x}_{i+1}$ and $\widetilde{x}_{i+2}$ shown in Figure 6.2 to $\widetilde{x}_{ll}, \widetilde{x}_l, \widetilde{x}_r$ and $\widetilde{x}_{rr}$, respectively, where subscript l, ll, r and rr denote 'left', 'left to left', 'right' and 'right to right' positions to the face AB, respectively. This nomenclature will be very handy in the subsequent discussions.

- Determining data values at positions $\widetilde{x}_{ll}, \widetilde{x}_l, \widetilde{x}_r$ and $\widetilde{x}_{rr}$ for an interface:

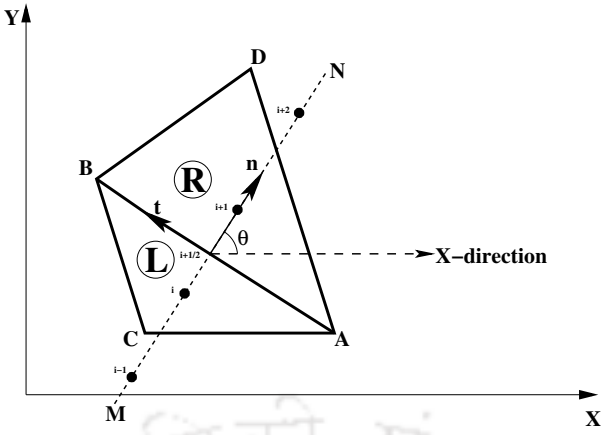

Figure 6.2. Demonstration of a 1D grid at interface AB of cells L and R.

Consider Figure 6.3, the data values at points C, Q, P and D are transferred to the points

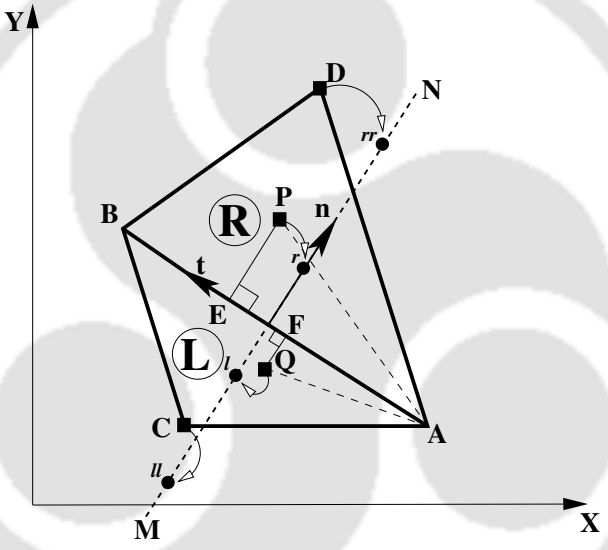

Figure 6.3. Assigning data values across face AB for flux calculation and determination of a representative grid spacing.

$\widetilde{x}_{ll}, \widetilde{x}_l, \widetilde{x}_r$ and $\widetilde{x}_{rr}$, respectively. If we consider a cell-centred method then data values at cell centres P and Q of cells R and L are known. To obtain data values at the vertices C and D, volume averaged values of the data at cell centres of the surrounding cells are used.

- Determining uniform grid spacing $\Delta\widetilde{x}$ between points ll and l, l and r, etc.:

  At first perpendiculars are drawn from cell centres P and Q on the interface AB which meet at points E and F, respectively (see Figure 6.3). Then average distance d_{av} of cell centres from the interface is determined by

$$d_{av} = \frac{\mathrm{PE} + \mathrm{QF}}{2}. \tag{6.2.7a}$$

$\Delta\widetilde{x}$ is then calculated as

$$\Delta\widetilde{x} = 2 \times d_{av}. \tag{6.2.7b}$$

The reason to calculate $\Delta\widetilde{x}$ like this is, that we always take the cell centre at the centroid of a triangular cell, so a line drawn from a vertex to the centre of the opposite face gets divided in the ratio 2 : 1 by the cell centre. Thus the vertex is twice the distance away from cell centre than the centre of the opposite face. So this $\Delta\widetilde{x}$ used in determining the positions $\widetilde{x}_{ll}, \widetilde{x}_l, \widetilde{x}_r$ and $\widetilde{x}_{rr}$ makes them land very close to cell centres and vertices if the grid is not very skewed, and hence gives good flux approximation. Now knowing the coordinates of A, P and Q, the geometry of the Figure 6.3 straightaway gives

$$\begin{aligned}\overrightarrow{AP} &= (x_P - x_A)\hat{i} + (y_P - y_A)\hat{j} \\ \overrightarrow{AQ} &= (x_Q - x_A)\hat{i} + (y_Q - y_A)\hat{j},\end{aligned}$$

where $\hat{i}$ and $\hat{j}$ are unit vectors in x and y-directions, respectively, and x_P, x_A, etc., are x-coordinates of points P, A, etc., and so on. Therefore,

$$\begin{aligned}\text{PE} &= \left|\overrightarrow{AP}.\mathbf{n}\right| = \left|\{(x_P - x_A)\hat{i} + (y_P - y_A)\hat{j}\}.(n_x\hat{i} + n_y\hat{j})\right| \\ \text{QF} &= \left|\overrightarrow{AQ}.\mathbf{n}\right| = \left|\{(x_Q - x_A)\hat{i} + (y_Q - y_A)\hat{j}\}.(n_x\hat{i} + n_y\hat{j})\right|.\end{aligned}$$

With this PE and QF, equation (6.2.7) gives

$$\Delta\widetilde{x} = |(x_P - x_A)n_x + (y_P - y_A)n_y| + |(x_Q - x_A)n_x + (y_Q - y_A)n_y|. \tag{6.2.8}$$

It should be noticed that $\Delta\widetilde{x}$ value is different for different faces.

Now having figured out the data values at points ll, l, r and rr of any face of a cell and $\Delta\widetilde{x}$ value calculated by equation (6.2.8), one can write the expression for conservative flux $\widetilde{\mathbf{FX}}_{\text{face}}$ using equation (6.2.2b) as

$$\begin{aligned}\widetilde{\mathbf{FX}}_{\text{face}} = &\left(\widetilde{\mathbf{FX}}_l^{+^n} + \widetilde{\mathbf{FX}}_r^{-^n}\right) \\ &+ \frac{1}{2}\text{avg}\left(\left(\widetilde{\mathbf{FX}}_r^{+^n} - \widetilde{\mathbf{FX}}_l^{+^n}\right), \left(\widetilde{\mathbf{FX}}_l^{+^n} - \widetilde{\mathbf{FX}}_{ll}^{+^n}\right)\right) \\ &- \frac{1}{2}\text{avg}\left(\left(\widetilde{\mathbf{FX}}_{rr}^{-^n} - \widetilde{\mathbf{FX}}_r^{-^n}\right), \left(\widetilde{\mathbf{FX}}_r^{-^n} - \widetilde{\mathbf{FX}}_l^{-^n}\right)\right) \\ &- \frac{\lambda}{2}\text{avg}\left(\left(\widetilde{\mathbf{GX}}_r^{+^n} - \widetilde{\mathbf{GX}}_l^{+^n}\right), \left(\widetilde{\mathbf{GX}}_l^{+^n} - \widetilde{\mathbf{GX}}_{ll}^{+^n}\right)\right) \\ &- \frac{\lambda}{2}\text{avg}\left(\left(\widetilde{\mathbf{GX}}_{rr}^{-^n} - \widetilde{\mathbf{GX}}_r^{-^n}\right), \left(\widetilde{\mathbf{GX}}_r^{-^n} - \widetilde{\mathbf{GX}}_l^{-^n}\right)\right)\end{aligned} \tag{6.2.9}$$

which can be written in the following manner by splitting the interface flux,

$$\widetilde{\mathbf{FX}}_{\text{face}} = \widetilde{\mathbf{FX}}^{+}_{\text{face}} + \widetilde{\mathbf{FX}}^{-}_{\text{face}}, \tag{6.2.10a}$$

where

$$\begin{aligned}
\widetilde{\mathbf{FX}}^{+}_{\text{face}} &= \widetilde{\mathbf{FX}}_{l}^{+^n} \\
&\quad + \frac{1}{2}\text{avg}\left(\left(\widetilde{\mathbf{FX}}_{r}^{+^n} - \widetilde{\mathbf{FX}}_{l}^{+^n}\right), \left(\widetilde{\mathbf{FX}}_{l}^{+^n} - \widetilde{\mathbf{FX}}_{ll}^{+^n}\right)\right) \\
&\quad - \frac{\lambda}{2}\text{avg}\left(\left(\widetilde{\mathbf{GX}}_{r}^{+^n} - \widetilde{\mathbf{GX}}_{l}^{+^n}\right), \left(\widetilde{\mathbf{GX}}_{l}^{+^n} - \widetilde{\mathbf{GX}}_{ll}^{+^n}\right)\right) \\
\text{and} \quad \widetilde{\mathbf{FX}}^{-}_{\text{face}} &= \widetilde{\mathbf{FX}}_{r}^{-^n} \\
&\quad - \frac{1}{2}\text{avg}\left(\left(\widetilde{\mathbf{FX}}_{rr}^{-^n} - \widetilde{\mathbf{FX}}_{r}^{-^n}\right), \left(\widetilde{\mathbf{FX}}_{r}^{-^n} - \widetilde{\mathbf{FX}}_{l}^{-^n}\right)\right) \\
&\quad - \frac{\lambda}{2}\text{avg}\left(\left(\widetilde{\mathbf{GX}}_{rr}^{-^n} - \widetilde{\mathbf{GX}}_{r}^{-^n}\right), \left(\widetilde{\mathbf{GX}}_{r}^{-^n} - \widetilde{\mathbf{GX}}_{l}^{-^n}\right)\right).
\end{aligned} \tag{6.2.10b}$$

Thus, this interface flux (6.2.10) with values of $\widetilde{\mathbf{FX}}^{\pm}$ and $\widetilde{\mathbf{GX}}^{\pm}$ determined by (6.2.4), when substituted in the finite volume formula (6.1.7) for $\widetilde{\mathbf{FX}}_k$ gives FLKS scheme applicable with triangular unstructured mesh.

Note: In the conservative flux expression (6.2.10) if the value of the "avg" function is put equal to zero, then

$$\widetilde{\mathbf{FX}}_{\text{face}} = \widetilde{\mathbf{FX}}_{l}^{+} + \widetilde{\mathbf{FX}}_{r}^{-} \tag{6.2.11}$$

and the first-order KFVS scheme gets implemented on the unstructured mesh.

6.3 Results and Discussion

This section discusses two test problems to show the accuracy and robustness of the FLKS scheme on unstructured grids. For time evolution a global time step Δt is determined first for each time iteration in all calculations. This Δt depends on a CFL value chosen. On triangular unstructured grid Δt is determined by following the work of Mavriplis et. al. [74] as

$$\Delta t = \text{CFL} \times \min_{i}\left(\frac{\Omega_i}{\Lambda_i}\right), \tag{6.3.1a}$$

where

$$\Lambda_i = \sum_{k=1}^{N}\left(|\mathbf{V}_{ik}\cdot\mathbf{n}_{ik}| + a_{ik}\right)A_{ik}. \tag{6.3.1b}$$

Here Ω_i is the volume of the i^{th} cell; i is the cell index. N is the number of faces of a cell (which is 3). $\mathbf{V}_{ik}$ and $\mathbf{n}_{ik}$ are the fluid velocity vector and unit outward normal vector, respectively at the k^{th} face of the i^{th} cell. a_{ik} and A_{ik} are the sonic speed and cell face area, respectively, of the k^{th} face of the i^{th} cell. The $\mathbf{V}_{ik}$ and a_{ik} values are determined at the k^{th} face as the average of values at the left and right cell centres. As in earlier chapters, the dimensional physical quantities in all the tests are in SI units, however, the units are not mentioned explicitly.

6.3.1 Accuracy test

The isentropic vortex problem as described in the work of Balsara [69] is used for accuracy test. A computational domain $[-5, 5] \times [-5, 5]$ with periodic boundaries is used and the calculation stops at a time of 10.0. Table 6.1 shows the global order of accuracy of FLKS scheme with

Table 6.1 Order of accuracy of FLKS scheme with minmod limiter for 2D case on unstructured grid. L_1 and L_∞ error norms for density are used for order calculation.

Scheme	N	L_1 error	L_1 order	L_∞ error	L_∞ order
FLKSmm, CFL= 0.9	16	0.019435		0.408662	
	32	0.013320	0.55	0.272739	0.58
	64	0.006730	0.98	0.117202	1.22
	128	0.003229	1.06	0.054754	1.10
FLKSmm, CFL= 0.1	16	0.018949		0.404165	
	32	0.011635	0.70	0.241310	0.74
	64	0.004802	1.28	0.086404	1.48
	128	0.001769	1.44	0.037408	1.21

minmod limiter for CFL values 0.9 and 0.1. N denotes the number of equal divisions of a boundary edge used in triangulating the square computational domain for getting triangular unstructured mesh. L_1 and L_∞ error norms for density are used for order calculation. Here again as in 1D, the low CFL value gives better order of convergence.

6.3.2 2D Riemann problems

The 2D Riemann problems already used on Cartesian grid in Chapter 4 are again considered here to check the capability of the FLKS scheme on triangular unstructured meshes. A CFL value of 0.5 is used for all calculations. Figure 6.4(a) shows density contours for first Riemann

problem obtained with KFVS scheme, and FLKS scheme with Van Leer limiter and $b = 0.35$. Figure 6.4(b) shows density contours for second Riemann problem. FLKS scheme captures all the flow features well.

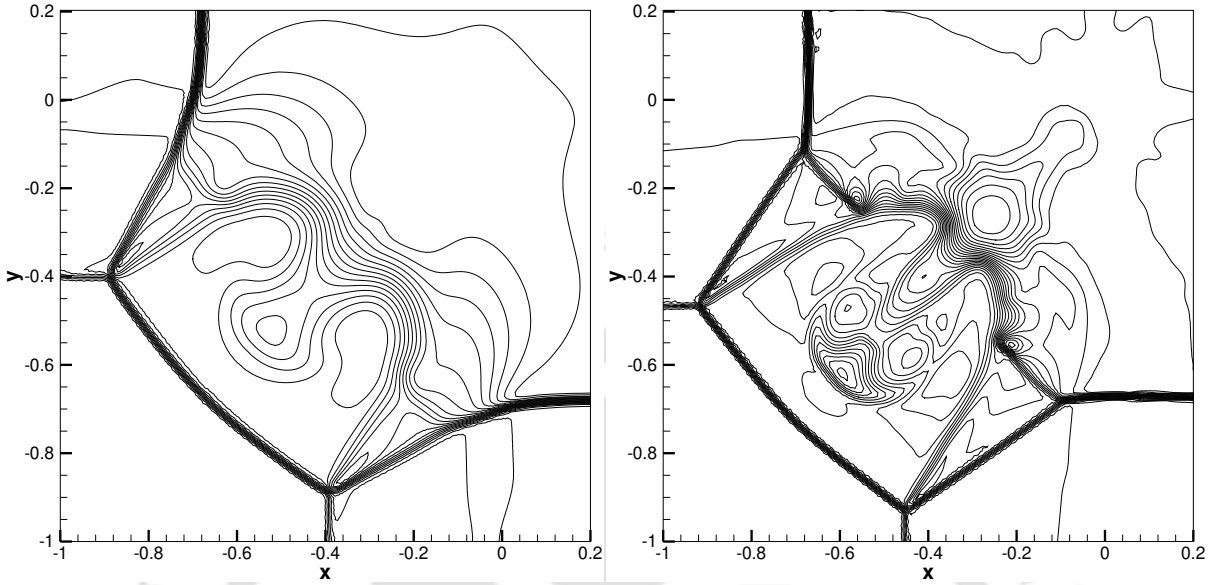

(a) First 2D Riemann problem. KFVS scheme (left) and FLKS scheme (right).

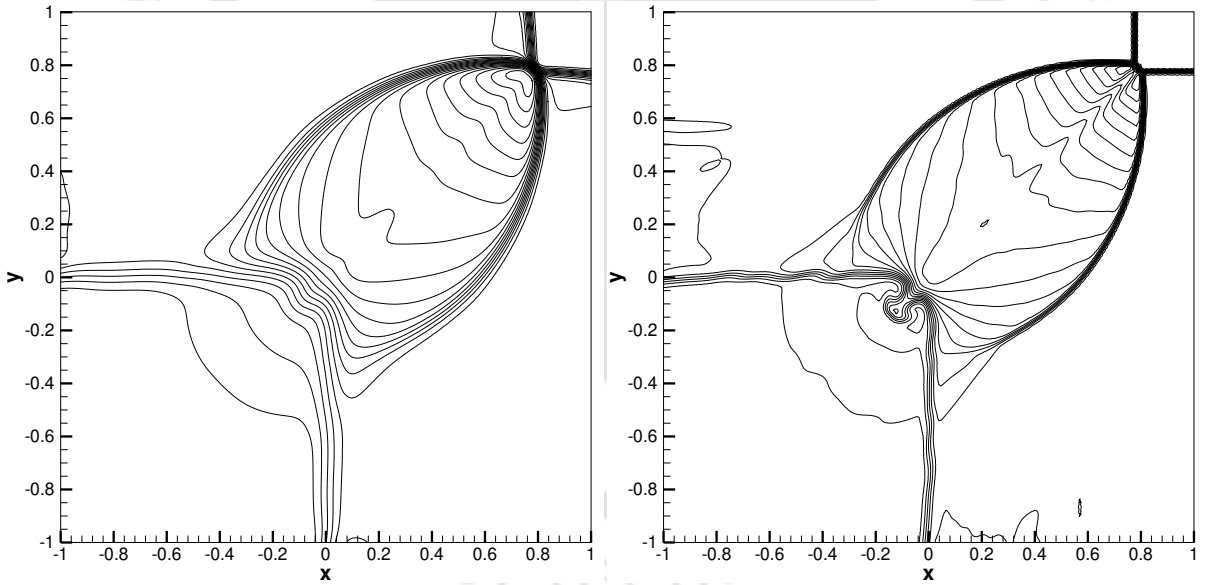

(b) Second 2D Riemann Problem. KFVS scheme (left) and FLKS scheme (right).

Figure 6.4. Density contours obtained for the two 2D Riemann problems using KFVS and FLKS schemes on triangular unstructured grid, are shown. (a) Result for first Riemann problem using 89954 triangular cells and 45378 vertices, where 30 contour levels from 0.190058 to 1.72619 have been used. The calculation stops at a time of 1.05. (b) Result for second Riemann problem using the same grid, where 30 contour levels from 0.568367 to 1.65618 have been used. The calculation stops at a time of 0.5.

6.3.3 2D blast wave problem

The 2D blast wave problem is described in the works of Toro and Balsara et. al. [5, 75]. A 2D computational domain $[-1,1] \times [-1,1]$ is taken in $x-y$ plane. From the centre $(0,0)$ upto a radial distance of 0.4, $(p, \rho, u, v) = (1.0, 1.0, 0.0, 0.0)$ is initialized, and the rest portion is given $(p, \rho, u, v) = (0.1, 0.125, 0.0, 0.0)$ values. A schematic of the setup is shown in Figure 6.5. This

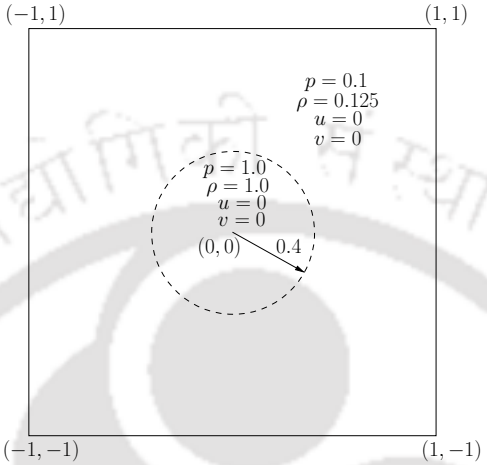

Figure 6.5. 2D blast wave problem setup

is like a 2D counterpart of the 1D shock tube problem of Sod. A circular shock, contact and expansion fan results. The calculation is stopped at a time of 0.25 before the shock reaches the boundary. The flow is symmetric about the z-axis, so plots of flow variables with respect to radial direction is the same in all directions. Here pressure and density plots are shown. For a reference solution for comparison, high resolution KFVS scheme [38] is used to solve an equivalent one dimensional inhomogeneous system [5] on a fine 1D grid with 3001 grid points. This is taken as the reference solution.

FLKS scheme with Van Leer limiter is used with $b = 0.35$ and a CFL of 0.9 on a triangular unstructured mesh with 89954 triangular cells and 45378 vertices. Fifty equidistant data points along radial direction from 0 to 1 are used for plotting. The Figure 6.6 clearly shows that the contact, shock and expansion fan are accurately captured.

6.4 Conclusions

An approach to implement FLKS scheme on triangular unstructured grids is suggested in this chapter. The rotational invariance property of the Euler equations has been utilized to construct the conservative numerical flux at a cell face. This flux calculation methodology works well on

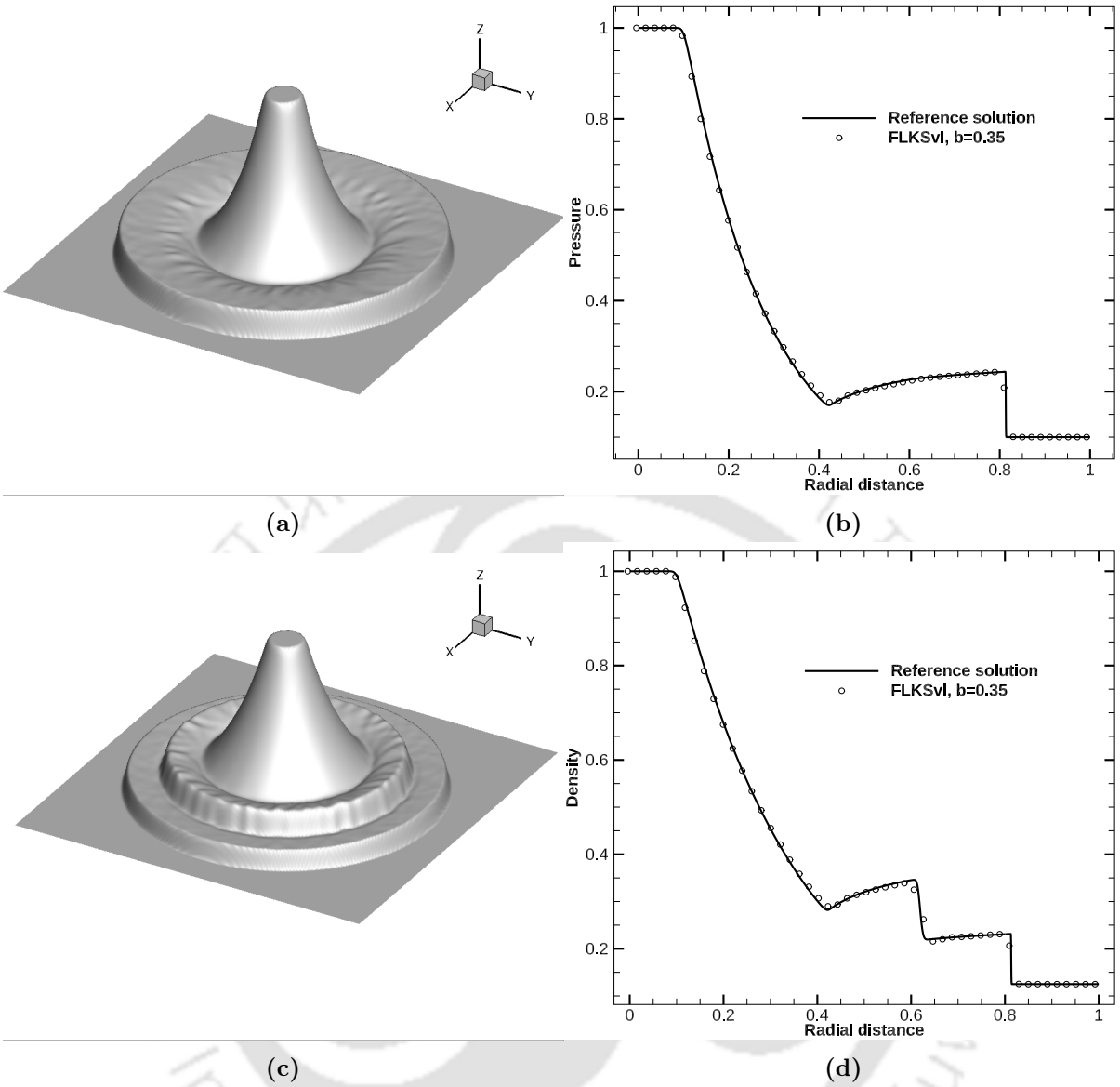

Figure 6.6. Results for 2D blast wave problem are shown. (a) Plot of pressure as vertical height. (b) Plot of pressure vs radial distance. Plots of (c) density as vertical height and (d) density vs radial distance.

grids that are not too skewed. The numerical tests suggest that the accuracy and the order-of-accuracy trends are similar to that observed for Cartesian grid case. The next chapter develops an entirely new methodology which does not require flux splitting and hence the computation cost is significantly lower than the FLKS scheme.

Chapter 7

A New Kinetic Flux-Corrected Scheme for the Euler Equations

In the earlier chapters, the FLKS scheme, its extensions and modifications have been discussed. This scheme is very robust, however, the computational cost is comparable to or even higher than already existing limiter-based schemes [52, 53] in the literature. In an attempt to reduce the computational cost, a new flux-corrected methodology based kinetic scheme is proposed in this chapter. This new scheme does not require any flux splitting or calculation of error functions like that in the KFVS and FLKS schemes. Also, the numerical flux has closed form formula which improves the efficiency substantially.

7.1 A New Flux-Corrected Kinetic Scheme for 1D Euler Equations

The KFVS and FLKS schemes involve flux splitting, and these split fluxes contain error functions, and these functions and the splitting increase the cost of computation. In an attempt to avoid the error functions and hence to reduce the cost for KFVS, a scheme namely, PVU [45] was proposed in the literature. This formulation does not require calculation of error functions, but the numerical dissipation increases when compared to KFVS scheme [46].

The splitting in the KFVS and FLKS schemes is a result of using CIR scheme at the Boltzmann level, which gives a non-smooth transition of the numerical flux between left and right moving waves for upwinding. To see this, we rewrite the linear advection equation (3.2.1),

$$\frac{\partial u}{\partial t} + \frac{\partial f(u)}{\partial x} = 0; \quad f(u) = au \quad (a\text{=constant}) \tag{3.2.1}$$

where u is a conserved variable which gets advected at wave speed a. A scheme in conservation form for this equation is

$$u_i^{n+1} = u_i^n - \lambda \left[\hat{f}^n_{i+\frac{1}{2}} - \hat{f}^n_{i-\frac{1}{2}} \right], \tag{7.1.1a}$$

where

$$\hat{f}^n_{i+\frac{1}{2}} = \frac{1}{2} a (u_i^n + u_{i+1}^n) - \frac{1}{2} \varepsilon^n_{i+\frac{1}{2}} (u_{i+1}^n - u_i^n) \tag{7.1.1b}$$

is the time averaged flux at the face $x_{i+\frac{1}{2}}$ at the i^{th} cell $\left[x_{i-\frac{1}{2}}, x_{i+\frac{1}{2}}\right]$. Here $\hat{f}^n_{i+\frac{1}{2}}$ has been written in "artificial viscosity" form [53] with coefficient of artificial viscosity $\varepsilon^n_{i+\frac{1}{2}}$. The Lax-Wendroff scheme for (3.2.1) has $\varepsilon^n_{i+\frac{1}{2}} = \lambda a^2$. Now following Laney [53], $\lambda\varepsilon$ vs λa plot for CIR, Lax-Wendroff, and first-order-accurate Boris-Book schemes are obtained as shown in Figure 7.1. This figure clearly shows that $\lambda\varepsilon$ for CIR scheme is not smooth at $\lambda a = 0$, where the slope

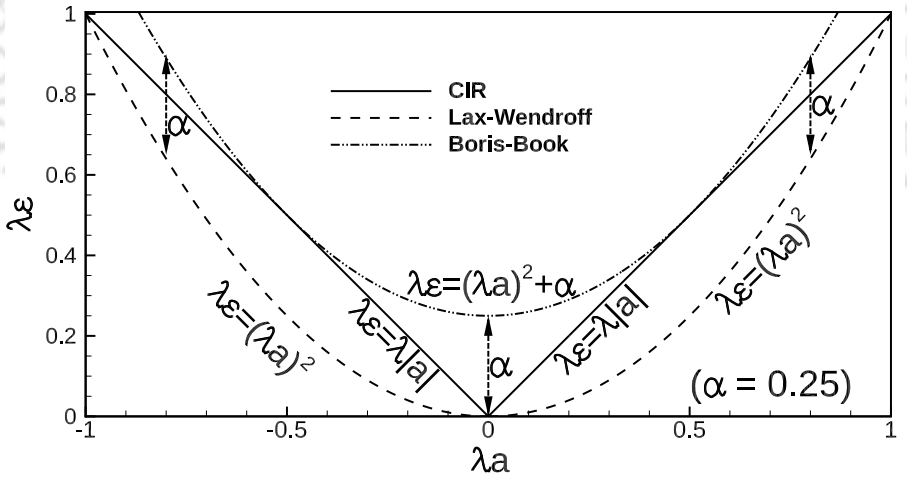

Figure 7.1. $\lambda\varepsilon$ vs λa plot for CIR, Lax-Wendroff, and first-order Boris-Book schemes.

of $\lambda\varepsilon$ suddenly changes from -1 to 1. Presence of this cusp at $\lambda a = 0$ in CIR scheme results in split fluxes and the error functions at the Euler level scheme. If in place of CIR scheme, a scheme with smooth $\lambda\varepsilon$ profile is used, then the splitting and error function can be avoided. The first-order-accurate Boris-Book method [76] for the linear advection equation (3.2.1) with $\lambda\varepsilon = (\lambda a)^2 + \alpha$, where $\alpha = 0.25$, as described in Laney [53], can be used. This first order method, as shown in Figure 7.1, is obtained by adding constant explicit artificial viscosity to the

Lax-Wendroff method. This Boris-Book method has $\lambda\varepsilon$ profile close to that of CIR and is more dissipative.

A limited combination of the first-order-accurate Boris-Book method and the Lax-Wendroff method can give a high-resolution scheme without involving any split fluxes or error functions. If we write the Boris-Book and Lax-Wendroff conservative fluxes as

$$\lambda\hat{f}^{B-B}_{i+\frac{1}{2}} = \frac{\lambda a}{2}(u^n_i + u^n_{i+1}) - \frac{1}{2}\{(\lambda a)^2 + \alpha\}(u^n_{i+1} - u^n_i), \tag{7.1.2}$$

$$\lambda\hat{f}^{L-W}_{i+\frac{1}{2}} = \frac{\lambda a}{2}(u^n_i + u^n_{i+1}) - \frac{1}{2}(\lambda a)^2(u^n_{i+1} - u^n_i), \tag{7.1.3}$$

respectively, then a high-resolution flux $\hat{f}^{HR}_{i+\frac{1}{2}}$ which is a limited combination of $\hat{f}^{B-B}_{i+\frac{1}{2}}$ and $\hat{f}^{L-W}_{i+\frac{1}{2}}$ is obtained by satisfying the following conditions suggested by Laney [53].

Condition 1: $\hat{f}^{HR}_{i+\frac{1}{2}}$ should lie between $\hat{f}^{B-B}_{i+\frac{1}{2}}$ and $\hat{f}^{L-W}_{i+\frac{1}{2}}$.

Condition 2: $\hat{f}^{HR}_{i+\frac{1}{2}}$ should be close to $\hat{f}^{B-B}_{i+\frac{1}{2}}$ near extrema, and close to $\hat{f}^{L-W}_{i+\frac{1}{2}}$ everywhere else.

Now, writing $\hat{f}^{HR}_{i+\frac{1}{2}}$ as a flux correction to $\hat{f}^{B-B}_{i+\frac{1}{2}}$, we get

$$\hat{f}^{HR}_{i+\frac{1}{2}} = \hat{f}^{B-B}_{i+\frac{1}{2}} + \hat{f}^{cor}_{i+\frac{1}{2}}, \tag{7.1.4}$$

where

$$\hat{f}^{cor}_{i+\frac{1}{2}} = \phi^n_{i+\frac{1}{2}}(\hat{f}^{L-W}_{i+\frac{1}{2}} - \hat{f}^{B-B}_{i+\frac{1}{2}}) \tag{7.1.5}$$

is the correction flux expressed in flux-limiting format with limiter $\phi^n_{i+\frac{1}{2}}$. The Condition 1 can now be written as

$$\min(\lambda\hat{f}^{B-B}_{i+\frac{1}{2}}, \lambda\hat{f}^{L-W}_{i+\frac{1}{2}}) \le \lambda\hat{f}^{HR}_{i+\frac{1}{2}} \le \max(\lambda\hat{f}^{B-B}_{i+\frac{1}{2}}, \lambda\hat{f}^{L-W}_{i+\frac{1}{2}}). \tag{7.1.6}$$

This implies

$$\min(0, \frac{\alpha}{2}(u^n_{i+1} - u^n_i)) \le \lambda\hat{f}^{cor}_{i+\frac{1}{2}} \le \max(0, \frac{\alpha}{2}(u^n_{i+1} - u^n_i)) \tag{7.1.7a}$$

or,

$$0 \le \phi^n_{i+\frac{1}{2}} \le 1. \tag{7.1.7b}$$

Similarly, Condition 2 implies

$$\lambda\hat{f}^{cor}_{i+\frac{1}{2}} \approx \begin{cases} 0, & \text{near extrema} \\ \frac{\alpha}{2}(u^n_{i+1} - u^n_i), & \text{otherwise} \end{cases} \tag{7.1.8a}$$

or,

$$\phi^n_{i+\frac{1}{2}} \approx \begin{cases} 0, & \text{near extrema} \\ 1, & \text{otherwise.} \end{cases} \tag{7.1.8b}$$

As described in Laney [53], these two conditions are satisfied by the following choice of flux-correction,

$$\hat{f}^{cor}_{i+\frac{1}{2}} = \frac{1}{\lambda}\text{minmod}((u^n_i - u^n_{i-1}), \frac{\alpha}{2}(u^n_{i+1} - u^n_i), (u^n_{i+2} - u^n_{i+1})) \tag{7.1.9a}$$

or,

$$\phi^n_{i+\frac{1}{2}} = \text{minmod}\left(\frac{2r^+_i}{\alpha}, 1, \frac{2}{\alpha r^+_{i+1}}\right), \tag{7.1.9b}$$

where

$$r^+_i = \frac{u^n_i - u^n_{i-1}}{u^n_{i+1} - u^n_i}. \tag{7.1.10}$$

With this expression for flux correction the new high-resolution flux for linear advection equation becomes

$$\lambda\hat{f}^{HR}_{i+\frac{1}{2}} = \frac{\lambda a}{2}(u^n_i + u^n_{i+1}) - \frac{(\lambda a)^2 + \alpha}{2}(u^n_{i+1} - u^n_i) + \text{minmod}((u^n_i - u^n_{i-1}), \frac{\alpha}{2}(u^n_{i+1} - u^n_i), (u^n_{i+2} - u^n_{i+1})). \tag{7.1.11}$$

Thus, the full discrete scheme for the linear advection equation is

$$\begin{aligned} u^{n+1}_i = u^n_i & \\ & - \frac{\lambda a}{2}(u^n_{i+1} - u^n_{i-1}) + \frac{1}{2}\left((\lambda a)^2 + \alpha\right)(u^n_{i+1} - 2u^n_i + u^n_{i-1}) \\ & - \text{minmod}\left((u^n_i - u^n_{i-1}), \frac{\alpha}{2}(u^n_{i+1} - u^n_i), (u^n_{i+2} - u^n_{i+1})\right) \\ & + \text{minmod}\left((u^n_{i-1} - u^n_{i-2}), \frac{\alpha}{2}(u^n_i - u^n_{i-1}), (u^n_{i+1} - u^n_i)\right) \end{aligned} \tag{7.1.12}$$

Now treating the 1D Boltzmann equation (2.2.1) as linear advection equation, the new flux-corrected scheme at the Boltzmann level using equation (7.1.12) becomes

$$\begin{aligned} F^{n+1}_i = F^n_i & \\ & - \frac{\lambda v_1}{2}(F^n_{i+1} - F^n_{i-1}) + \frac{1}{2}\left((\lambda v_1)^2 + \alpha\right)(F^n_{i+1} - 2F^n_i + F^n_{i-1}) \\ & - \text{minmod}\left((F^n_i - F^n_{i-1}), \frac{\alpha}{2}(F^n_{i+1} - F^n_i), (F^n_{i+2} - F^n_{i+1})\right) \\ & + \text{minmod}\left((F^n_{i-1} - F^n_{i-2}), \frac{\alpha}{2}(F^n_i - F^n_{i-1}), (F^n_{i+1} - F^n_i)\right). \end{aligned} \tag{7.1.13}$$

The $\boldsymbol{\Psi}$-moment of this scheme gives the Euler level scheme

$$\begin{aligned}\mathbf{U}_i^{n+1} &= \mathbf{U}_i^n \\ &- \frac{\lambda}{2}(\mathbf{FX}_{i+1}^n - \mathbf{FX}_{i-1}^n) + \frac{\lambda^2}{2}(\mathbf{GX}_{i+1}^n - 2\mathbf{GX}_i^n + \mathbf{GX}_{i-1}^n) \\ &+ \frac{\alpha}{2}(\mathbf{U}_{i+1}^n - 2\mathbf{U}_i^n + \mathbf{U}_{i-1}^n) \\ &- \text{minmod}\left((\mathbf{U}_i^n - \mathbf{U}_{i-1}^n), \frac{\alpha}{2}(\mathbf{U}_{i+1}^n - \mathbf{U}_i^n), (\mathbf{U}_{i+2}^n - \mathbf{U}_{i+1}^n)\right) \\ &+ \text{minmod}\left((\mathbf{U}_{i-1}^n - \mathbf{U}_{i-2}^n), \frac{\alpha}{2}(\mathbf{U}_i^n - \mathbf{U}_{i-1}^n), (\mathbf{U}_{i+1}^n - \mathbf{U}_i^n)\right),\end{aligned} \tag{7.1.14}$$

which we call "Kinetic Flux Corrected (KFC)" scheme. Here $\mathbf{U}$ and $\mathbf{FX}$ are conservative variable vector and flux vector, respectively, of the 1D Euler equations, and

$$\begin{aligned}\mathbf{GX} &= <\boldsymbol{\Psi}, v_1^2 F> \\ &= \begin{bmatrix} p + \rho u^2 \\ (3p + \rho u^2)u \\ \frac{\gamma}{\gamma-1}\frac{p^2}{\rho} + \frac{5\gamma-3}{2(\gamma-1)}pu^2 + \frac{\rho u^4}{2} \end{bmatrix}.\end{aligned} \tag{7.1.15}$$

One important thing to mention here is, that the equation (7.1.9) for flux correction is a convenient choice and there can be a better choice based on more sophisticated and detailed stability analysis. It comes out that for strong shock cases, and the cases where low pressure and density are involved, the KFC scheme may produce significant spurious wiggles. To tackle these situations we can add small amount of explicit second-order artificial viscosity with a coefficient of viscosity μ. This modification gives the final form of the KFC scheme as

$$\begin{aligned}\mathbf{U}_i^{n+1} &= \mathbf{U}_i^n \\ &- \frac{\lambda}{2}(\mathbf{FX}_{i+1}^n - \mathbf{FX}_{i-1}^n) + \frac{\lambda^2}{2}(\mathbf{GX}_{i+1}^n - 2\mathbf{GX}_i^n + \mathbf{GX}_{i-1}^n) \\ &+ \left(\frac{\alpha}{2} + \mu\right)(\mathbf{U}_{i+1}^n - 2\mathbf{U}_i^n + \mathbf{U}_{i-1}^n) \\ &- \text{minmod}\left((\mathbf{U}_i^n - \mathbf{U}_{i-1}^n), \frac{\alpha}{2}(\mathbf{U}_{i+1}^n - \mathbf{U}_i^n), (\mathbf{U}_{i+2}^n - \mathbf{U}_{i+1}^n)\right) \\ &+ \text{minmod}\left((\mathbf{U}_{i-1}^n - \mathbf{U}_{i-2}^n), \frac{\alpha}{2}(\mathbf{U}_i^n - \mathbf{U}_{i-1}^n), (\mathbf{U}_{i+1}^n - \mathbf{U}_i^n)\right).\end{aligned} \tag{7.1.16}$$

Finally, the scheme (7.1.16) is put in the conservation form

$$\mathbf{U}_i^{n+1} = \mathbf{U}_i^n - \lambda\left[\hat{\mathbf{f}}_{i+\frac{1}{2}}^n - \hat{\mathbf{f}}_{i-\frac{1}{2}}^n\right], \tag{7.1.17a}$$

where

$$\hat{\mathbf{f}}^n_{i+\frac{1}{2}} = \frac{1}{2}(\mathbf{F}\mathbf{X}^n_i + \mathbf{F}\mathbf{X}^n_{i+1}) - \frac{\lambda}{2}(\mathbf{G}\mathbf{X}^n_{i+1} - \mathbf{G}\mathbf{X}^n_i) - \left(\frac{\alpha + 2\mu}{2\lambda}\right)(\mathbf{U}^n_{i+1} - \mathbf{U}^n_i) + \frac{1}{\lambda}\text{minmod}((\mathbf{U}^n_i - \mathbf{U}^n_{i-1}), \frac{\alpha}{2}(\mathbf{U}^n_{i+1} - \mathbf{U}^n_i), (\mathbf{U}^n_{i+2} - \mathbf{U}^n_{i+1})). \tag{7.1.17b}$$

The coefficient of explicit artificial viscosity μ is a user-adjustable parameter and it can be made local data dependent using some nonlinear stability analysis, however, this analysis has not been done. In our calculations $\mu = 0.01$ works for all the tests, and no significant spurious oscillations are visible.

7.2 Extension of KFC to 2D Cartesian Grids

The extension of the KFC scheme to 2D Cartesian grids can be done exactly the way it is done for the FLKS scheme, i.e., by using dimensional splitting. The x-sweep using KFC can be done by

$$\begin{aligned}\mathbf{U}^{n+1}_{i,j} = \mathbf{U}^n_{i,j} &- \frac{\lambda_1}{2}(\mathbf{F}\mathbf{X}^n_{i+1,j} - \mathbf{F}\mathbf{X}^n_{i-1,j}) + \frac{\lambda_1^2}{2}(\mathbf{G}\mathbf{X}^n_{i+1,j} - 2\mathbf{G}\mathbf{X}^n_{i,j} + \mathbf{G}\mathbf{X}^n_{i-1,j}) \\ &+ \left(\frac{\alpha}{2} + \mu\right)(\mathbf{U}^n_{i+1,j} - 2\mathbf{U}^n_{i,j} + \mathbf{U}^n_{i-1,j}) \\ &- \text{minmod}\left((\mathbf{U}^n_{i,j} - \mathbf{U}^n_{i-1,j}), \frac{\alpha}{2}(\mathbf{U}^n_{i+1,j} - \mathbf{U}^n_{i,j}), (\mathbf{U}^n_{i+2,j} - \mathbf{U}^n_{i+1,j})\right) \\ &+ \text{minmod}\left((\mathbf{U}^n_{i-1,j} - \mathbf{U}^n_{i-2,j}), \frac{\alpha}{2}(\mathbf{U}^n_{i,j} - \mathbf{U}^n_{i-1,j}), (\mathbf{U}^n_{i+1,j} - \mathbf{U}^n_{i,j})\right),\end{aligned} \tag{7.2.1a}$$

where

$$\begin{aligned}\mathbf{G}\mathbf{X} &= <\boldsymbol{\Psi}, v_1^2 F> \\ &= \begin{bmatrix} p + \rho u^2 \\ (3p + \rho u^2)u \\ (p + \rho u^2)v \\ \frac{\gamma}{\gamma-1}\frac{p^2}{\rho} + \frac{5\gamma-3}{2(\gamma-1)}pu^2 + \frac{1}{2}pv^2 + \frac{\rho u^2}{2}(u^2 + v^2) \end{bmatrix}\end{aligned} \tag{7.2.1b}$$

with $\boldsymbol{\Psi}$ definition given by equation (2.5.3). Similarly, the y-sweep is done by

$$\begin{aligned}\mathbf{U}_{i,j}^{n+1} &= \mathbf{U}_{i,j}^{n} \\ &- \frac{\lambda_2}{2}(\mathbf{FY}_{i,j+1}^{n} - \mathbf{FY}_{i,j-1}^{n}) + \frac{\lambda_2^2}{2}(\mathbf{GY}_{i,j+1}^{n} - 2\mathbf{GY}_{i,j}^{n} + \mathbf{GY}_{i,j-1}^{n}) \\ &+ \left(\frac{\alpha}{2} + \mu\right)(\mathbf{U}_{i,j+1}^{n} - 2\mathbf{U}_{i,j}^{n} + \mathbf{U}_{i,j-1}^{n}) \\ &- \text{minmod}\left((\mathbf{U}_{i,j}^{n} - \mathbf{U}_{i,j-1}^{n}), \frac{\alpha}{2}(\mathbf{U}_{i,j+1}^{n} - \mathbf{U}_{i,j}^{n}), (\mathbf{U}_{i,j+2}^{n} - \mathbf{U}_{i,j+1}^{n})\right) \\ &+ \text{minmod}\left((\mathbf{U}_{i,j-1}^{n} - \mathbf{U}_{i,j-2}^{n}), \frac{\alpha}{2}(\mathbf{U}_{i,j}^{n} - \mathbf{U}_{i,j-1}^{n}), (\mathbf{U}_{i,j+1}^{n} - \mathbf{U}_{i,j}^{n})\right),\end{aligned} \tag{7.2.2a}$$

where

$$\begin{aligned}\mathbf{GY} &= <\boldsymbol{\Psi}, v_2^2 F> \\ &= \begin{bmatrix} p + \rho v^2 \\ (p + \rho v^2)u \\ (3p + \rho v^2)v \\ \frac{\gamma}{\gamma-1}\frac{p^2}{\rho} + \frac{5\gamma-3}{2(\gamma-1)}pv^2 + \frac{1}{2}pu^2 + \frac{\rho v^2}{2}(u^2+v^2) \end{bmatrix}.\end{aligned} \tag{7.2.2b}$$

7.3 KFC on Unstructured Grids

The KFC scheme can be implemented on triangular unstructured grids by using the same methodology as is used for the FLKS scheme in Chapter 6. We start with the integral form of the 2D Euler equations (6.1.1),

$$\frac{d}{dt}\iiint_{CV} \mathbf{U} dV + \iint_{CS} \mathbb{F}.\mathbf{n} dA = 0. \tag{6.1.1}$$

A conservative and forward in time explicit discretization of equation (6.1.1) over a finite control volume gives

$$\mathbf{U}_i^{n+1} = \mathbf{U}_i^n - \frac{\Delta t}{V}\sum_{k=1}^{N} \mathbb{F}_k.\mathbf{n}_k A_k, \tag{7.3.1}$$

where N is the number of faces of the control volume or cell, V is the volume (area in 2D) of the cell, A_k is the area (length in 2D) of the k^{th} face and Δt is the time step. Also we adopt cell-centred finite volume methodology where the $\mathbf{U}$ values are stored at the cell centres of cells. A finite volume scheme gives a method to determine the value of the intercell flux $\mathbb{F}_k.\mathbf{n}_k$. Consider Figure 7.2 which shows two triangular cells ABC (denoted by L) and ABD (denoted by R) adjacent to each other which are a part of an unstructured grid. AB is the common face between cells L and R. For evaluating $\mathbb{F}.\mathbf{n}$ at the face AB for cell L, one can write

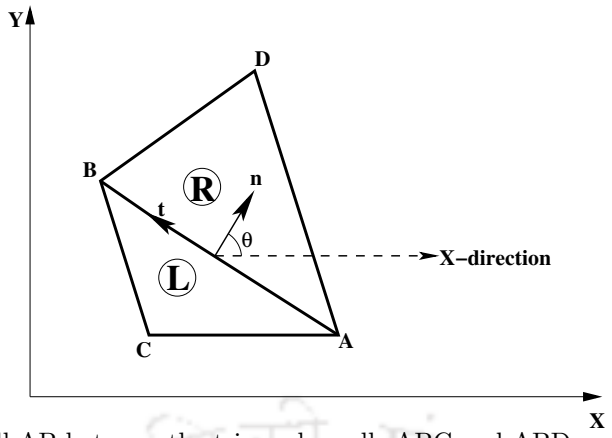

Figure 7.2. Intercell AB between the triangular cells ABC and ABD, and the rotated coordinate system $(\mathbf{n}, \mathbf{t})$.

$$\mathbb{F}.\mathbf{n} = \mathbf{FX}\cos\theta + \mathbf{FY}\sin\theta, \tag{7.3.2}$$

where $\mathbf{n} = (n_x, n_y) = (\cos\theta, \sin\theta)$. Also the Euler equations are rotationally invariant [5], i.e.,

$$\mathbf{FX}(\mathbf{U})\cos\theta + \mathbf{FY}(\mathbf{U})\sin\theta = \mathbf{T}^{-1}\mathbf{FX}(\mathbf{TU}), \tag{7.3.3}$$

where $\mathbf{T}$ and $\mathbf{T}^{-1}$ are the rotation matrix and its inverse, respectively, as given below.

$$\mathbf{T} = \begin{bmatrix} 1 & 0 & 0 & 0 \\ 0 & \cos\theta & \sin\theta & 0 \\ 0 & -\sin\theta & \cos\theta & 0 \\ 0 & 0 & 0 & 1 \end{bmatrix}, \quad \mathbf{T}^{-1} = \begin{bmatrix} 1 & 0 & 0 & 0 \\ 0 & \cos\theta & -\sin\theta & 0 \\ 0 & \sin\theta & \cos\theta & 0 \\ 0 & 0 & 0 & 1 \end{bmatrix}. \tag{7.3.4}$$

We now write

$$\widetilde{\mathbf{U}} = \mathbf{TU} = \begin{bmatrix} 1 & 0 & 0 & 0 \\ 0 & \cos\theta & \sin\theta & 0 \\ 0 & -\sin\theta & \cos\theta & 0 \\ 0 & 0 & 0 & 1 \end{bmatrix} \begin{bmatrix} \rho \\ \rho u \\ \rho v \\ \rho e \end{bmatrix} = \begin{bmatrix} \rho \\ \rho V_n \\ \rho V_t \\ \rho e \end{bmatrix} \tag{7.3.5}$$

and

$$\widetilde{\mathbf{FX}} = \mathbf{FX}(\widetilde{\mathbf{U}}) = \begin{bmatrix} \rho V_n \\ p + \rho V_n^2 \\ \rho V_n V_t \\ (p + \rho e)V_n \end{bmatrix}, \tag{7.3.6}$$

where $\widetilde{\mathbf{U}}$ is the vector of rotated conserved variables and

$$V_n = u\cos\theta + v\sin\theta \quad \text{and} \quad V_t = -u\sin\theta + v\cos\theta \tag{7.3.7}$$

are the fluid velocity components at the face AB in normal and tangential directions, respectively. The finite volume formula (7.3.1) using equations (7.3.2) and (7.3.3) then becomes

$$\mathbf{U}_i^{n+1} = \mathbf{U}_i^n - \frac{\Delta t}{V}\sum_{k=1}^{N} \mathbf{T}_k^{-1}\widetilde{\mathbf{FX}}_k A_k. \tag{7.3.8}$$

The Euler equations in the rotated frame $(\mathbf{n}, \mathbf{t})$ become the augmented one-dimensional equations [5] given by

$$\frac{\partial \widetilde{\mathbf{U}}}{\partial t} + \frac{\partial \widetilde{\mathbf{FX}}}{\partial \widetilde{x}} = 0, \tag{7.3.9}$$

where $\widetilde{x}$ is the new rotated x-direction which is along the unit normal vector $\mathbf{n}$ to the face AB (the new rotated y-direction is along the unit vector $\mathbf{t}$, tangential to AB). The numerical flux $\widetilde{\mathbf{FX}}_k$ using the KFC scheme can be constructed for this augmented equation (7.3.9) which in turn can be used in equation (7.3.8).

The KFC scheme for the augmented 1D Euler equations (7.3.9) in $\mathbf{n}$-direction can be obtained by first discretizing a 1D collisionless Boltzmann equation in direction $\mathbf{n}$ and then taking $\boldsymbol{\Psi}$-moment. The 1D collisionless Boltzmann equation in $\mathbf{n}$ direction can be written as

$$\frac{\partial F}{\partial t} + v_n \frac{\partial F}{\partial \widetilde{x}} = 0, \tag{7.3.10}$$

where F is the Maxwellian distribution given by

$$F = \frac{\rho}{I_0}\left(\frac{\beta}{\pi}\right) \exp\left[-\beta\left\{(v_n - V_n)^2 + (v_t - V_t)^2\right\} - \frac{I}{I_0}\right], \tag{7.3.11}$$

and v_n and v_t are molecular velocities along $\mathbf{n}$ and $\mathbf{t}$ directions, respectively. Here $I_0 = \frac{2-\gamma}{\gamma-1}RT$, $\beta = \frac{1}{2RT}$, T is temperature, R is gas constant per unit mass and I is internal energy variable corresponding to non-translational degree of freedom. This equation (7.3.10) when discretized using the flux-corrected method gives the 1D flux-corrected scheme in conservation form as

$$F_i^{n+1} = F_i^n - \lambda(\hat{f}^n_{i+\frac{1}{2}} - \hat{f}^n_{i-\frac{1}{2}}), \tag{7.3.12}$$

where λ is time step size over grid spacing $\Delta\widetilde{x}$ and $\hat{f}^n_{i+\frac{1}{2}}$ is time integral averaged flux through the right face of a 1D cell volume i, respectively, and

$$\lambda\hat{f}^n_{i+\frac{1}{2}} = \lambda\hat{f}^{B-B}_{i+\frac{1}{2}} + \lambda\hat{f}^{cor}_{i+\frac{1}{2}}, \tag{7.3.13}$$

where

$$\lambda \hat{f}^{B-B}_{i+\frac{1}{2}} = \frac{\lambda v_n}{2}(F^n_{i+1} + F^n_i) - \frac{1}{2}\left((\lambda v_n)^2 + \alpha\right)(F^n_{i+1} - F^n_i) \tag{7.3.14}$$

and

$$\lambda \hat{f}^{cor}_{i+\frac{1}{2}} = \text{minmod}\left((F^n_i - F^n_{i-1}), \frac{\alpha}{2}(F^n_{i+1} - F^n_i), (F^n_{i+2} - F^n_{i+1})\right). \tag{7.3.15}$$

Now defining the $\boldsymbol{\Psi}$-moment of a distribution f as

$$\langle \boldsymbol{\Psi}, f \rangle = \int_0^\infty dI \int_{-\infty}^\infty dv_t \int_{-\infty}^\infty dv_n \boldsymbol{\Psi} f. \tag{7.3.16}$$

with

$$\boldsymbol{\Psi} = \begin{bmatrix} 1 \\ v_n \\ v_t \\ I + \frac{v_n^2 + v_t^2}{2} \end{bmatrix} \tag{7.3.17}$$

and then taking $\boldsymbol{\Psi}$-moment of equation (7.3.12) gives a flux-corrected scheme for the augmented 1D Euler equations (7.3.9) as

$$\widetilde{\mathbf{U}}^{n+1}_i = \widetilde{\mathbf{U}}^n_i - \lambda(\hat{\boldsymbol{f}}^n_{i+\frac{1}{2}} - \hat{\boldsymbol{f}}^n_{i-\frac{1}{2}}), \tag{7.3.18}$$

where

$$\begin{aligned} \hat{\boldsymbol{f}}^n_{i+\frac{1}{2}} &= \frac{1}{2}(\widetilde{\mathbf{FX}}^n_i + \widetilde{\mathbf{FX}}^n_{i+1}) \\ &- \left(\mu + \frac{\alpha}{2\lambda}\right)(\widetilde{\mathbf{U}}^n_{i+1} - \widetilde{\mathbf{U}}^n_i) - \frac{\lambda}{2}(\widetilde{\mathbf{G}}^n_{i+1} - \widetilde{\mathbf{G}}^n_i) \\ &+ \frac{1}{\lambda}\text{minmod}\left((\widetilde{\mathbf{U}}^n_i - \widetilde{\mathbf{U}}^n_{i-1}), \frac{\alpha}{2}(\widetilde{\mathbf{U}}^n_{i+1} - \widetilde{\mathbf{U}}^n_i), (\widetilde{\mathbf{U}}^n_{i+2} - \widetilde{\mathbf{U}}^n_{i+1})\right) \end{aligned} \tag{7.3.19}$$

with $\widetilde{\mathbf{G}}$ value obtained as

$$\begin{aligned} \widetilde{\mathbf{G}} &= < \boldsymbol{\Psi}, v_n^2 F > \\ &= \begin{bmatrix} p + \rho V_n^2 \\ (3p + \rho V_n^2) V_n \\ (p + \rho V_n^2) V_t \\ \frac{\gamma}{\gamma - 1}\frac{p^2}{\rho} + \frac{5\gamma - 3}{2(\gamma - 1)} p V_n^2 + \frac{1}{2} p V_t^2 + \frac{\rho V_n^2}{2}(V_n^2 + V_t^2) \end{bmatrix}. \end{aligned} \tag{7.3.20}$$

Here μ is the coefficient of explicit second-order artificial viscosity introduced in the formulation to reduce spurious oscillations, if any, when strong shock calculations are done. The formulation

(7.3.18) is valid along a 1D grid in **n** direction and the flux calculation (7.3.19) requires four equidistant cell data values at positions $i-1, i, i+1$ and $i+2$.

Now the numerical flux $\widetilde{\mathbf{FX}}_k$ for the k^{th} face, say AB of the cell L in Figure 7.2, can be obtained by using equation (7.3.19) where data at cell centres L and R are assigned at positions i and $i+1$, respectively, and $i-1$ position is assigned the surrounding cells volume averaged value at vertex C, and similarly value at vertex D is assigned to $i+2$ position. For getting $\Delta\widetilde{x}$ value for calculating $\lambda = \frac{\Delta t}{\Delta \widetilde{x}}$ we use the sum of normal distances of cell centres of L and R from the face AB. Thus, the flux (7.3.19) can be used for the face AB of cell L in Figure 7.2 by writing it as

$$\begin{aligned}\widetilde{\mathbf{FX}}^n_{AB} = &\frac{1}{2}(\widetilde{\mathbf{FX}}^n_L + \widetilde{\mathbf{FX}}^n_R) \\ &- \left(\mu + \frac{\alpha}{2\lambda}\right)(\widetilde{\mathbf{U}}^n_R - \widetilde{\mathbf{U}}^n_L) - \frac{\lambda}{2}(\widetilde{\mathbf{G}}^n_R - \widetilde{\mathbf{G}}^n_L) \\ &+ \frac{1}{\lambda}\text{minmod}\left((\widetilde{\mathbf{U}}^n_L - \widetilde{\mathbf{U}}^n_C), \frac{\alpha}{2}(\widetilde{\mathbf{U}}^n_R - \widetilde{\mathbf{U}}^n_L), (\widetilde{\mathbf{U}}^n_D - \widetilde{\mathbf{U}}^n_R)\right). \end{aligned} \tag{7.3.21}$$

When this flux is used in equation (7.3.8) for $\widetilde{\mathbf{FX}}_k$ for any general face k, we get a high-resolution flux-corrected scheme on an unstructured grid. The parameters μ and α in equation (7.3.21) can be made locally data dependent using some nonlinear stability analysis but here we have used fixed values for calculations. For several standard test problems involving weak and strong shock cases $\alpha = 0.01$ and $\mu = 0.1$ give results without any significant oscillations.

7.4 Results and Discussion

This section discusses several test problems already discussed in Chapters 3, 4, and 6 for 1D and 2D Euler flows. For time evolution a global time step Δt is determined first for time integration. This Δt depends on a CFL value chosen. The Δt calculation is done exactly the same way as in Chapters 3, 4, and 6.

7.4.1 Performance of 1D KFC Scheme

Accuracy test

An exact periodic solution for 1D Euler equations is used as given in the work of Arun et. al. [64]. The same setup as used in Chapter 3 has been used. The grid is refined successively and error norm for density is calculated. Table 7.1 shows the L_1- and L_∞-norm-based orders for CFL values of 0.25 and 0.01. It is clear that as the CFL number is reduced the order of accuracy

Table 7.1 Order of accuracy of KFC scheme for 1D case. L_1 and L_∞ error norms for density are used for order calculation.

Scheme	Number of cells	L_1 error	L_1 order	L_∞ error	L_∞ order
KFC, CFL= 0.25	20	0.0038572650		0.0133482898	
	40	0.0011225650	1.78	0.0056108660	1.25
	80	0.0003992066	1.49	0.0020451189	1.46
	160	0.0001836189	1.12	0.0007952973	1.36
	320	0.0000929337	0.98	0.0003305747	1.27
	640	0.0000447791	1.05	0.0001456719	1.18
	1280	0.0000231396	0.95	0.0000675012	1.11
KFC, CFL= 0.01	20	0.0200620499		0.0508565493	
	40	0.0042059338	2.25	0.0171232596	1.57
	80	0.0008337954	2.33	0.0046783080	1.87
	160	0.0001550346	2.43	0.0015303170	1.61
	320	0.0000294663	2.40	0.0004199064	1.87
	640	0.0000057050	2.37	0.0001173749	1.84
	1280	0.0000014688	1.96	0.0000323034	1.86

improves. For a CFL number of 0.01, close to second order convergence in L_1 error norm is achieved. L_∞ order is consistently below 2.0. This low value can probably be attributed to the low order of reduction of clipping errors due to limiting at extrema.

1D Riemann problems

Here, two Riemann problems, namely, the Sod's shock tube problem and its another version with strong shock and an expansive sonic point, as already discussed in Chapter 3 are solved.

For Sod's shock tube problem a CFL number of 0.25 has been used. Figures 7.3(a), 7.3(b), 7.3(c) and 7.3(d), respectively, show the plots of pressure, density, velocity and internal energy obtained using 301 grid points. The resolution obtained using KFC is close to that by HRKFVS scheme, and there are no significant spurious oscillations in pressure, density, and velocity plots. Only in the internal energy plot the oscillations around contact discontinuity for KFC is large compared to HRKFVS. In the following discussions it will be shown that KFC takes significantly

less computational time than HRKFVS, and it can be made less oscillatory by adding small amount of explicit second-order artificial viscosity.

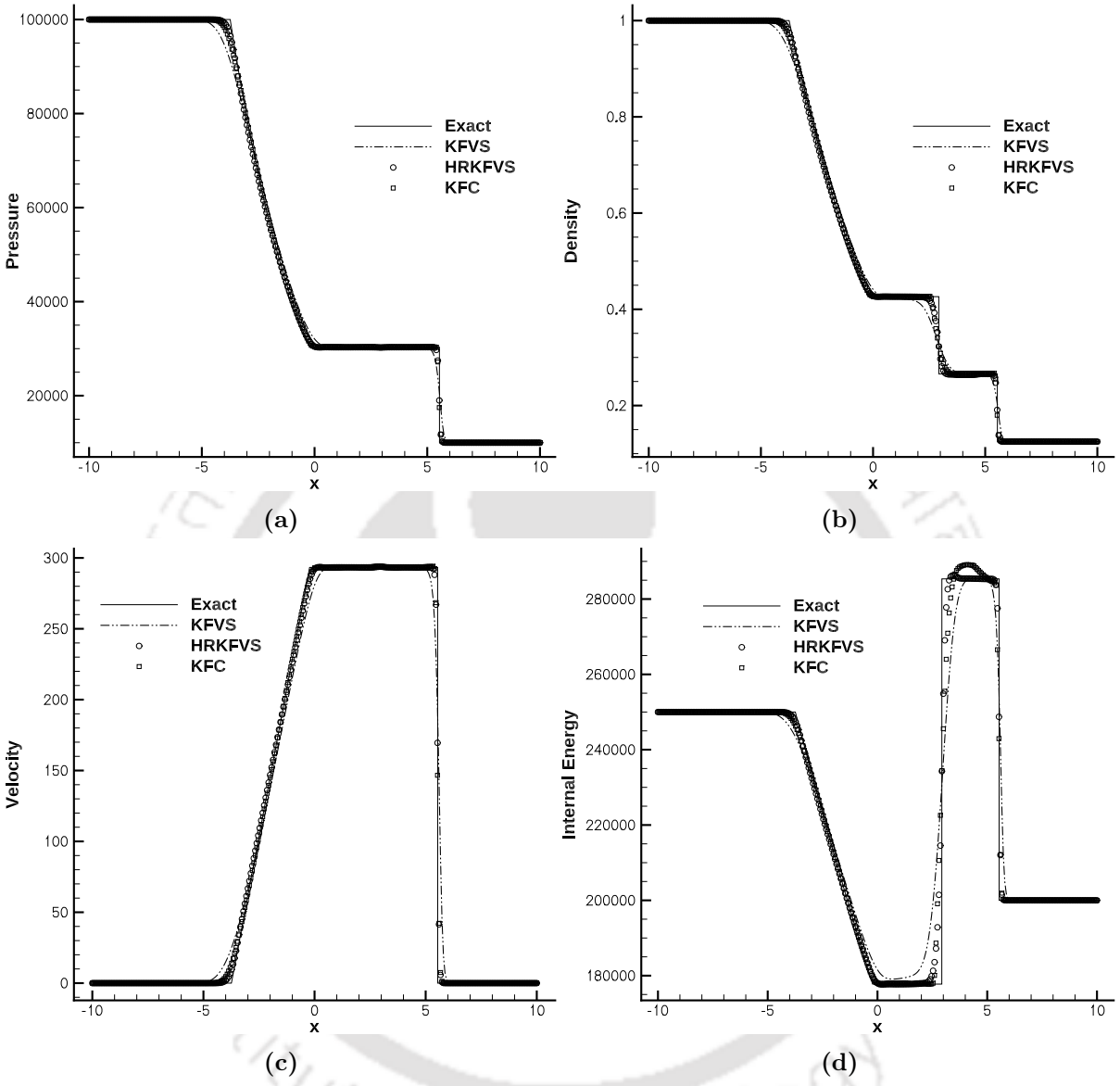

Figure 7.3. Sod's shock tube problem. Plots for (a) pressure, (b) density, (c) velocity and (d) internal energy with 301 grid points. The calculation stops at a time of 0.01.

For the second shock tube problem the initial condition results in an expansive sonic point at $x = 0$ in the expansion fan region. At such sonic points many schemes cause expansion shocks to appear which are nonphysical and an indication of the violation of second law of thermodynamics. Figure 7.4 clearly shows that KFC violates entropy condition and small amount of second-order artificial viscosity ($\mu = 0.01$) removes the expansion shock at the expansive sonic point $x = 0$. Once the need of explicit artificial viscosity is figured out, the KFC scheme is now compared with the HRKFVS scheme in Figure 7.5. Clearly, KFC still gives very good resolution and is

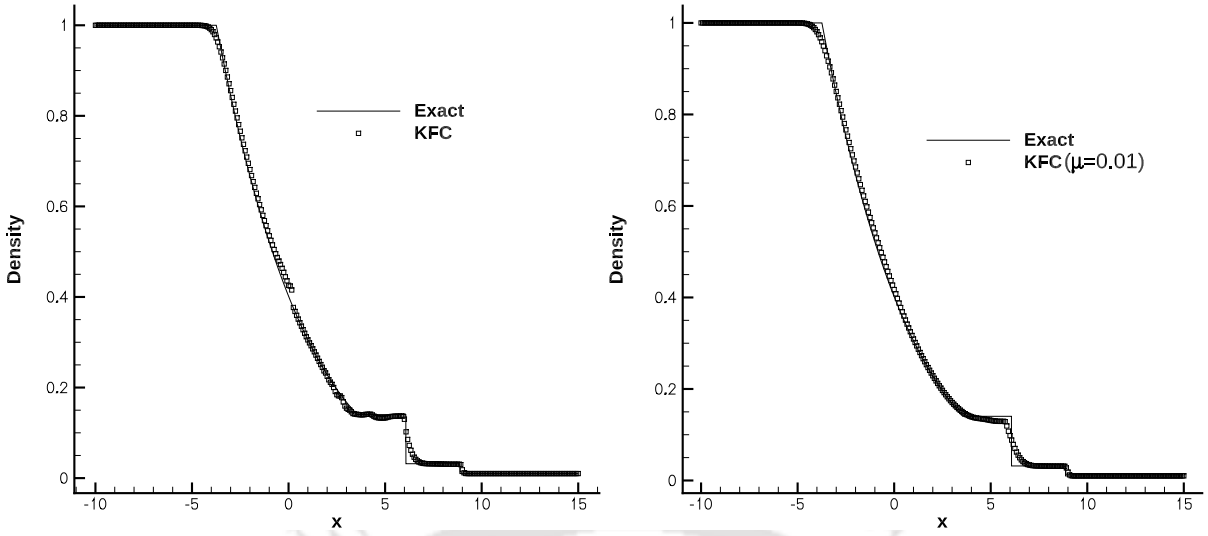

(a) (b)

Figure 7.4. Second shock tube problem. Plots for density (a) without explicit artificial viscosity and (b) with artificial viscosity ($\mu = 0.01$) using KFC scheme. The calculation stops at a time of 0.01.

less oscillatory than HRKFVS, as can be seen in the velocity and internal energy plots.

Blast wave problem

For this test we choose 1001 grid points, a CFL number of 0.25, and coefficient of second-order explicit artificial viscosity $\mu = 0.01$. Figure 7.6 shows that KFC gives very good resolution for this test also.

Shu-Osher shock-entropy wave interaction problem

Figure 7.7 shows density plot obtained for Shu-Osher problem using 501 grid points with CFL= 0.25. The extrema capturing ability of KFC is comparable to HRKFVS.

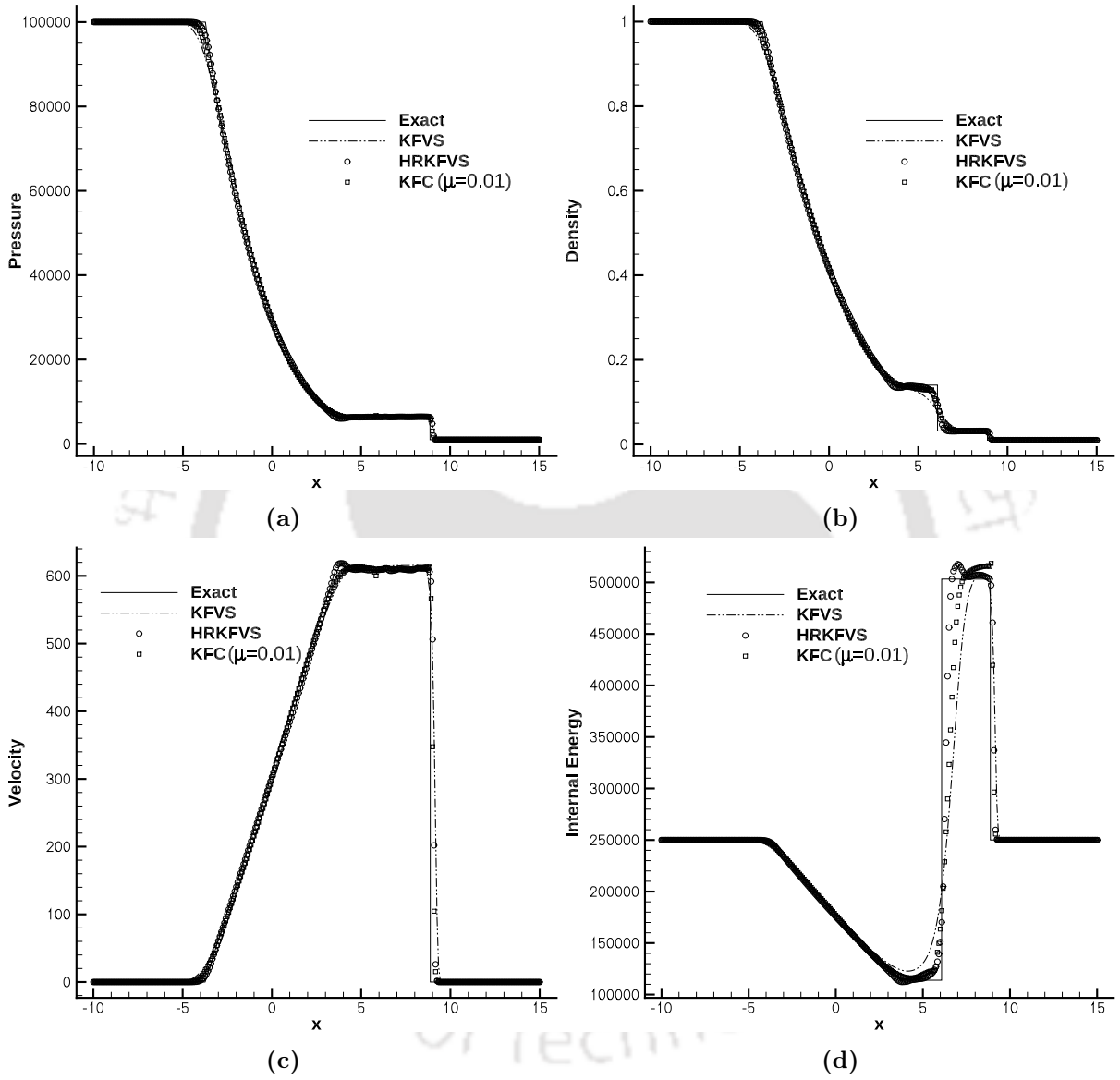

Figure 7.5. Second shock tube problem. Plots for (a) pressure, (b) density, (c) velocity and (d) internal energy with 301 grid points using KFC scheme with $\mu = 0.01$. The calculation stops at a time of 0.01.

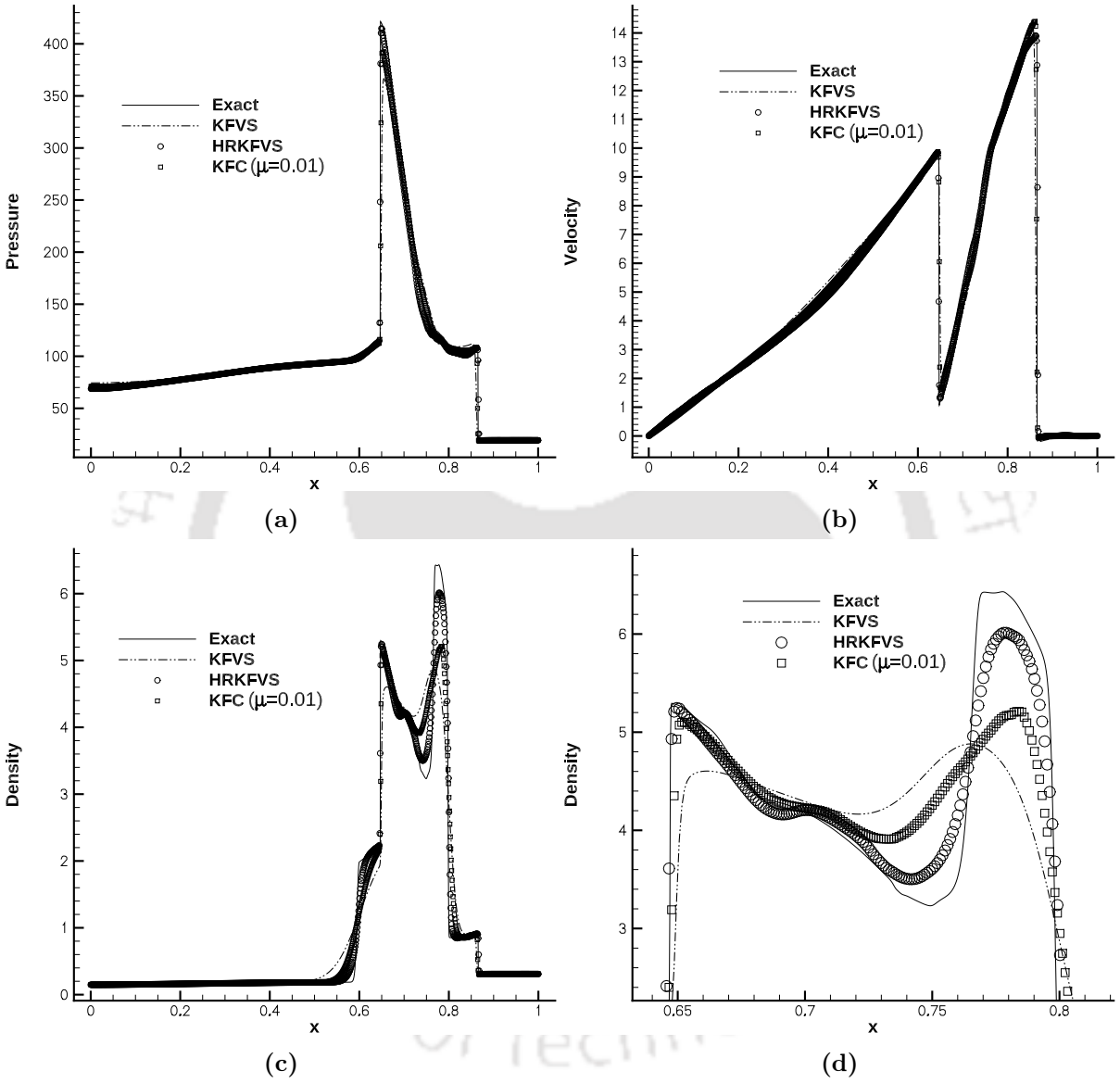

Figure 7.6. 1D Blast wave problem. (a) and (b) show the pressure and velocity plots, respectively. (c) and (d) show density plot and a zoomed portion of it, respectively. The calculation stops at a time of 0.038.

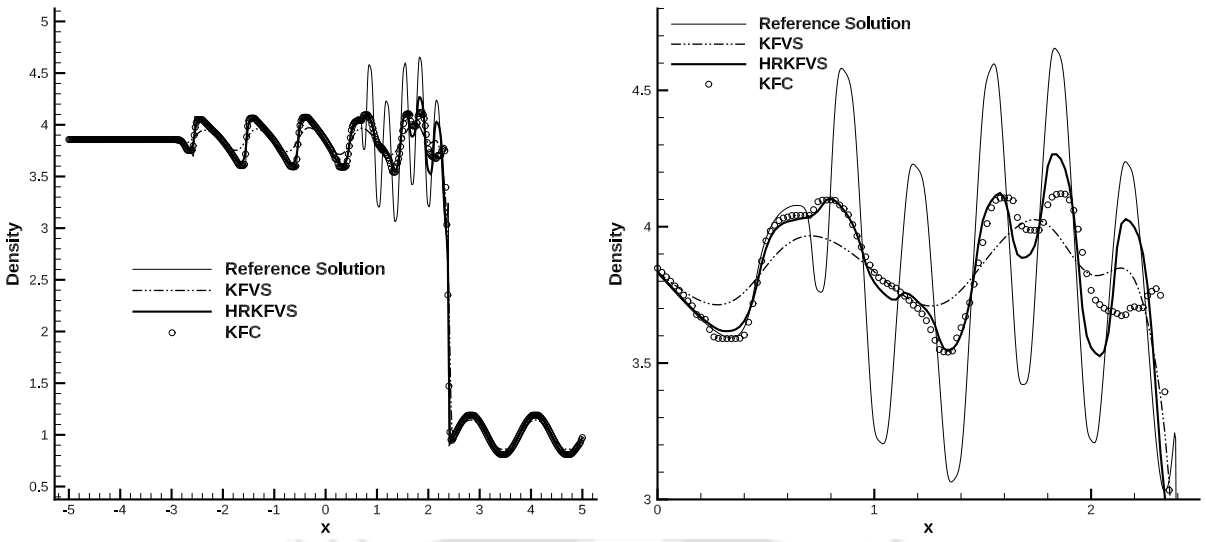

Figure 7.7. (a) Density plot obtained for Shu-Osher problem using 501 grid points with CFL= 0.25. (b) Zoomed view of extrema containing upper regions for clarity. The calculation stops at a time of 1.8.

Comparisons of computational time

Table 7.2 compares KFC scheme with HRKFVS for computational time in seconds for three tests, namely, Sod, blast wave and Shu-Osher. KFC is roughly four times faster than HRKFVS. This is the advantage that was targeted without losing resolution, and it has been achieved,

Table 7.2 Computational time comparison of KFC scheme with HRKFVS in seconds for Sod, blast wave, and Shu-Osher tests.

Scheme	Sod test	Blast wave test	Shu-Osher test
HRKFVS	0.82	46.66	6.41
KFC	0.25	10.73	1.54

although stability got compromised a bit.

7.4.2 Performance of 2D KFC Scheme on Cartesian Grids

Forward facing step problem

Figure 7.8 shows the density contours on a 240×80 Cartesian grid. A CFL number of 0.5 and $\mu = 0.01$ has been used, and the calculation stops at 4.0 time units. No special treatment for the

singular step corner point has been done. Figures 7.8(a), 7.8(b) and 7.8(c), respectively show the calculations by first order KFVS scheme, FLKS scheme with Van Leer limiter and KFC scheme. The figures clearly show that the resolution obtained by KFC is as good as that of FLKS scheme. Clearly the reflected shock, the curved shock ahead of the step and the Mach stem are captured well by KFC. The sonic line just above the corner of the step makes several schemes to give an expansion shock suggesting the violation of entropy condition. Figure 7.8(c) does show small expansion shock when KFC scheme is used with $\mu = 0.01$, which can be removed by increasing the value of μ by a small amount.

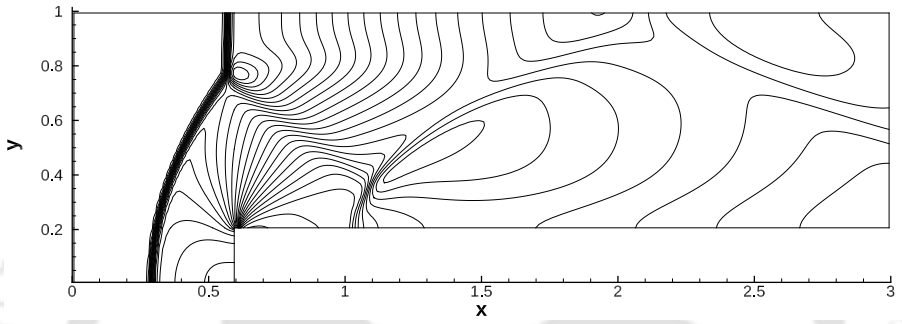

(a) First order KFVS scheme

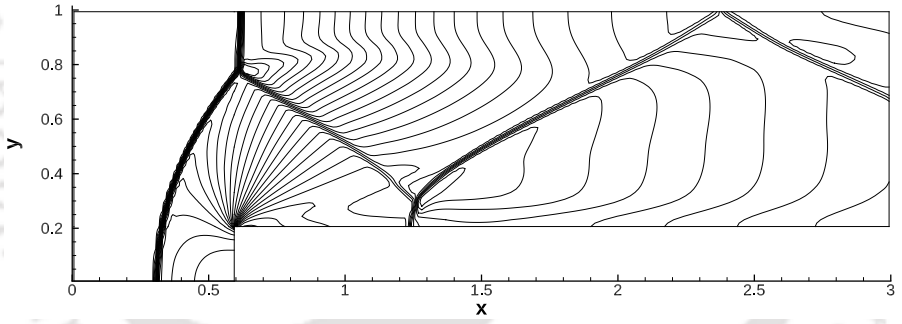

(b) FLKS scheme with Van Leer limiter

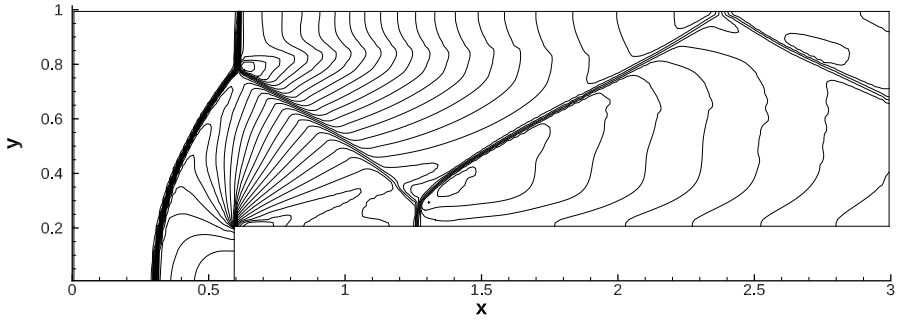

(c) KFC scheme

Figure 7.8. Density plot for forward facing step problem using 240×80 Cartesian grid, showing 25 contour levels from 0.392491 to 6.00827 at a time of 4.0.

Double Mach reflection problem

Figure 7.9 shows results on a 960×240 Cartesian grid with a CFL number of 0.5. KFC scheme works without difficulty. It is clearly seen that the resolution achieved by KFC scheme is comparable to that of the FLKS scheme.

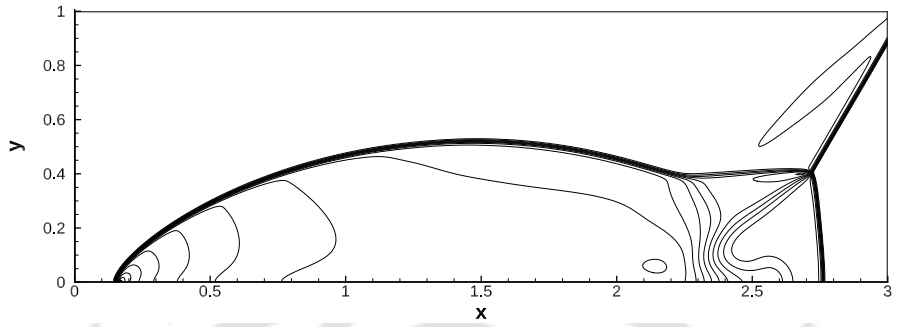

(a) First order KFVS scheme

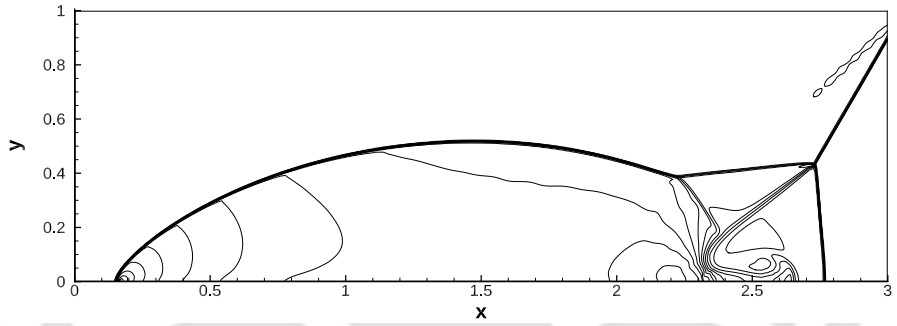

(b) FLKS scheme with Van Leer limiter

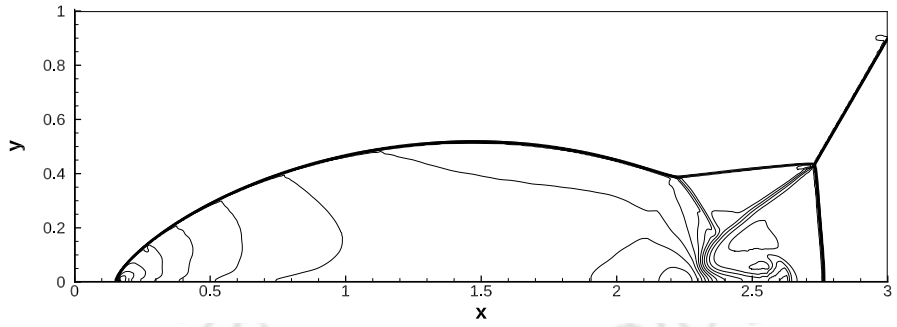

(c) KFC scheme

Figure 7.9. Density plot for double Mach reflection problem. Shows 25 contour levels from 2.21039 to 21.6598 using 960×240 Cartesian grid.

2D Riemann problems

The first 2D Riemann problem as described in Chapter 4 is solved on a 400×400 Cartesian grid with a CFL number of 0.5. The calculation stops at a time of 1.1. The problem starts with four shocks and results in a double Mach reflection. Figure 7.10 shows density contours

obtained at a time of 1.1. The high resolution obtained with the KFC scheme is obvious, and it is comparable to that obtained by FLKS scheme with Van Leer limiter. The shocks, slip lines and the mushroom cap get captured crisply.

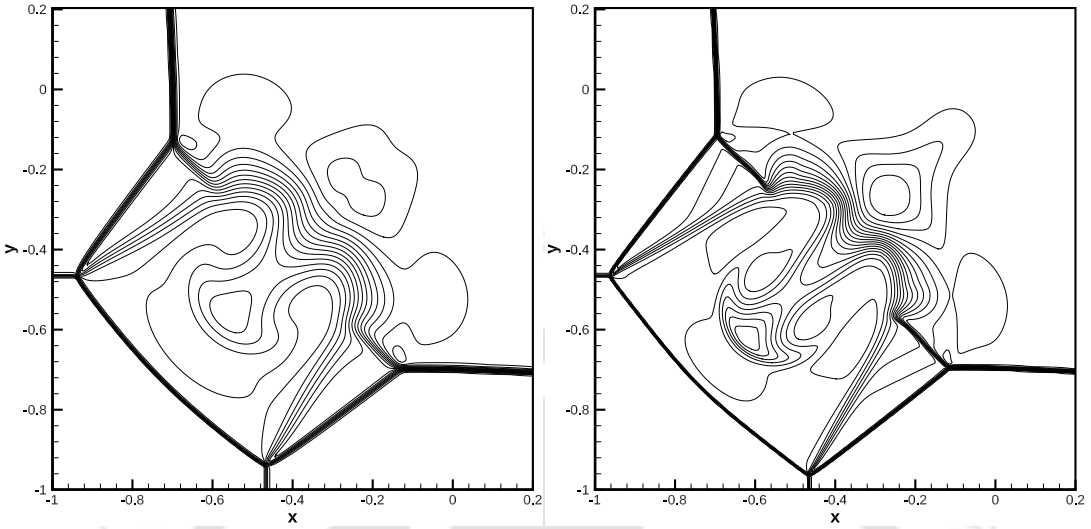

(a) First order KFVS scheme **(b)** FLKS scheme with Van Leer limiter

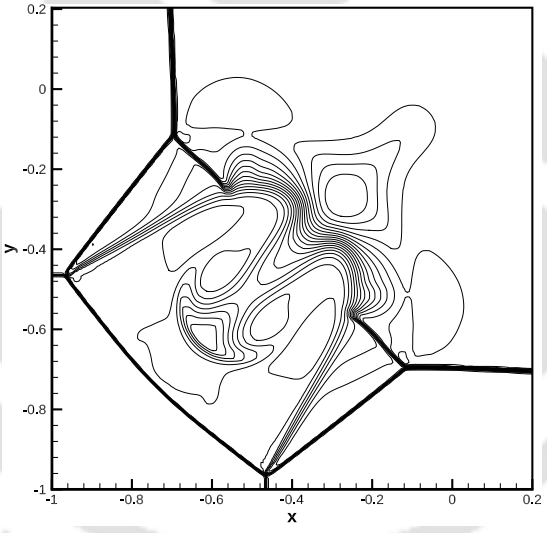

(c) KFC scheme

Figure 7.10. Density plot for first 2D Riemann problem using 400 × 400 Cartesian grid, showing 25 contour levels from 0.200076 to 1.69231 at a time of 1.1.

The second Riemann problem is solved on a 400 × 400 Cartesian grid with a CFL number of 0.5. The calculation stops at a time of 0.52. The solution evolves starting with two shocks and two slip lines. Figure 7.11 shows the density contours obtained by using KFVS, FLKS, and KFC schemes. It is clear that flux-correction in KFC makes the shocks and contacts resolve as good as that in the case of flux-limiting in FLKS.

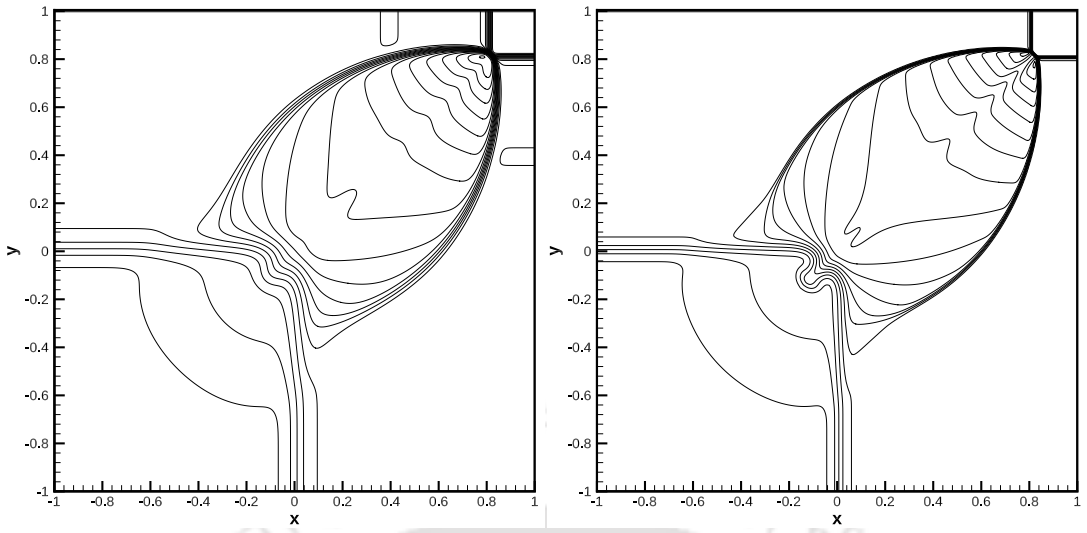

(a) First order KFVS scheme **(b)** FLKS scheme with Van Leer limiter

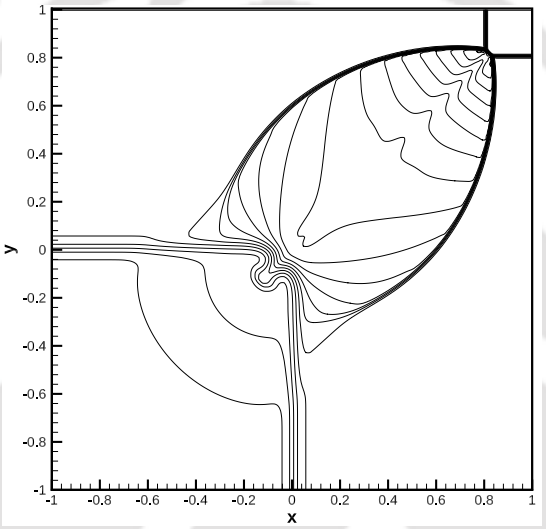

(c) KFC scheme

Figure 7.11. Density plot for second 2D Riemann problem using 400 × 400 Cartesian grid, showing 25 contour levels from 0.577799 to 1.69377 at a time of 0.52.

Comparisons of computational time

Table 7.3 compares KFC scheme with FLKS and KFVS schemes for computational time in seconds for four tests, namely, forward facing step, double Mach reflection, and 2D Riemann problems. KFC is roughly five to six times faster than FLKS. This is a huge advantage for KFC scheme over FLKS scheme while the resolutions obtained are comparable.

7.4.3 Performance of KFC Scheme on Triangular Unstructured Grids

Forward facing step problem

The tunnel dimensions and the grid used having 5102 cells are shown in the Figure 7.12.

Table 7.3 Computational time comparison of KFC scheme with FLKS and KFVS schemes in seconds for forward facing step, double Mach reflection, and 2D Riemann problems.

Scheme	Forward facing step	Double Mach reflection	First Riemann	Second Riemann
FLKS	2351.76	11264.77	6337.43	2376.56
KFC	456.30	2191.14	1054.26	442.02
KFVS	264.26	2021.17	778.31	326.42

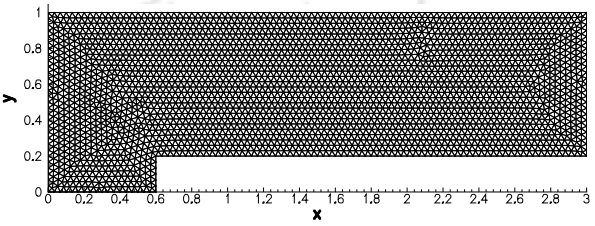

Figure 7.12. Grid used for forward facing step problem.

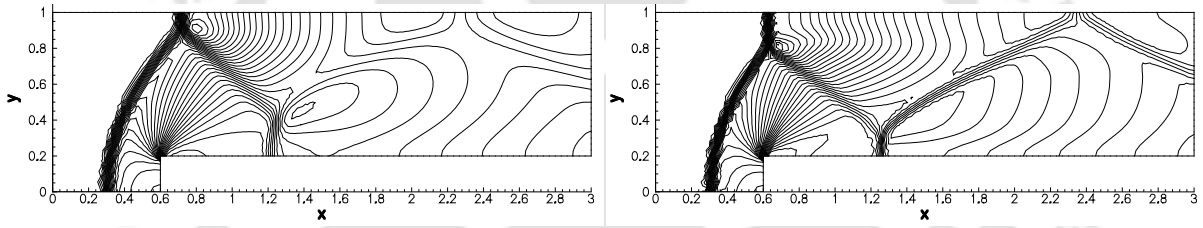

(a) **(b)**

Figure 7.13. Density contours obtained using 30 equidistant contour levels from 0.772242 to 6.17514 for (a) first-order KFVS scheme and (b) the KFC scheme.

Figure 7.13 shows the density contours obtained with a CFL of 0.8 at 4.0 time units. No special treatment for the singular step corner point has been done. The KFC scheme uses $\alpha = 0.01$ and $\mu = 0.15$. The figures clearly show the expected improvement in the results by using the KFC scheme when compared to the first-order KFVS scheme, as the sharpness of the reflected shock, the curved shock ahead of the step and the Mach stem improve. Particularly, the reflected shock which was not visible for the first-order scheme gets captured well with the new scheme.

2D blast wave problem

The 2D blast wave problem as already described in Chapter 6 has been used here. This is like a 2D counterpart of the 1D shock tube problem of Sod. A circular shock, contact and expansion fan results. The calculation is stopped at time of 0.25 before the shock reaches the boundary. The flow is symmetric about the z-axis, and therefore, the plots of flow variables with respect

to radial direction is the same in all directions. Here pressure and density plots are shown. For a reference solution for comparison, high resolution KFVS scheme [38] is used to solve an equivalent one dimensional inhomogeneous system on a fine 1D grid with 3001 grid points.

Figure 7.14 shows the solution obtained with a CFL of 0.8 on a triangular unstructured mesh with 89954 cells and 45378 vertices. Fifty equidistant data points along radial direction from 0 to 1 are used for plotting. We use $\alpha = 0.01$ and $\mu = 0.05$. Clearly the new scheme captures contact, shock and the corners of the expansion fan with very good resolution.

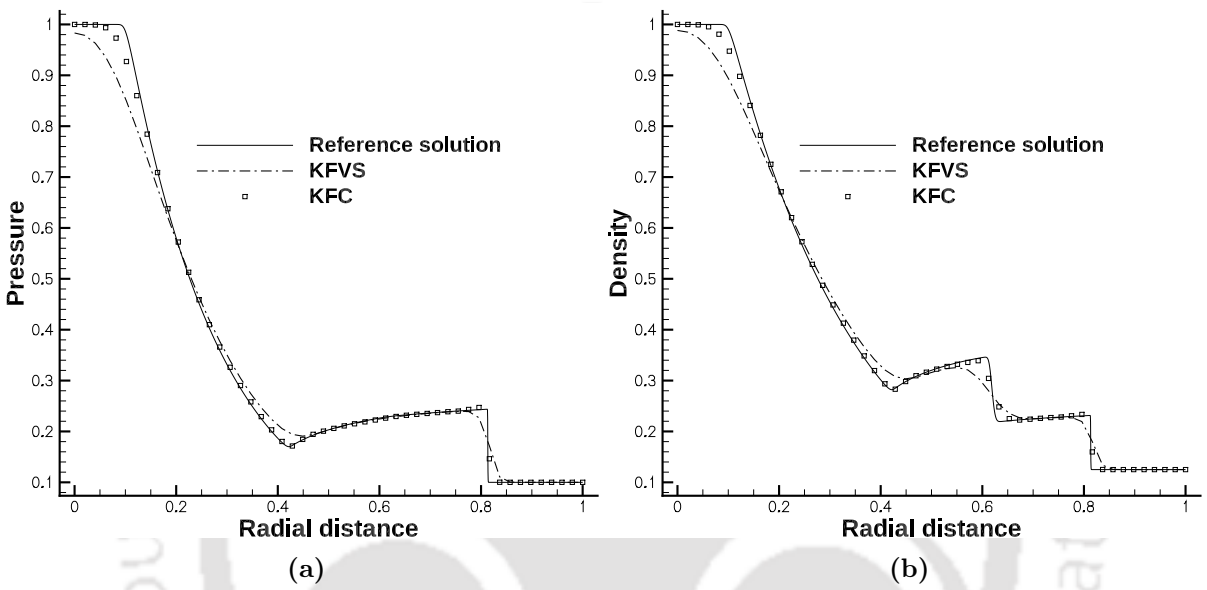

Figure 7.14. 2D blast wave problem. (a) Pressure and (b) density plots obtained using first-order KFVS scheme and the KFC scheme.

7.5 Conclusions

The kinetic flux-corrected scheme KFC proposed in this Chapter is a high-resolution scheme for the Euler equations. The use of flux-correction approach at the Boltzmann level results in an Euler level scheme having closed form numerical fluxes without any flux-splitting. The scheme works for CFL numbers upto 1. The flux-correction provides sufficient nonlinear stability to avoid any significant spurious oscillations. For strong shock cases a small amount of explicit second-order artificial viscosity is needed to suppress small spurious wiggles. The simplicity of the scheme makes it very cost effective when compared to HRKFVS and FLKS schemes. The test calculations using the scheme demonstrates its robustness and the ability to capture discontinuities very sharply.

Chapter 8

Conclusions and Future Recommendations

This chapter mainly describes the major achievements of the thesis besides mentioning what future work can be taken up afterwards. Wherever an observation is made or an inference drawn, to prepare the background the work done is also briefly described.

8.1 Conclusions

The thesis work is mainly concerned with the development of some numerical schemes and solution procedures for the computation of Euler and Navier-Stokes equations of gas dynamics. Since the schemes are new, for their validation several computer codes are developed on structured and unstructured grids. All the codes are written in the programming language C and they form a significant part of the total volume of work. Historically, there are a plethora of discretization schemes for the Euler and the Navier-Stokes equations. However, none of them are uniformly good for the entire range of Mach numbers starting from low-speed subsonic to high-speed flows. Consequently, the quest for a good scheme that is better than some existing schemes in one respect or another is still an ongoing process. The present work can be looked at in that context. Since kinetic theory-based schemes are generally known for their robustness which comes concomitantly with undesirably high dissipation, some attempts are made in this

thesis to develop kinetic-theory-based schemes that are sufficiently robust and contain relatively low dissipation.

In the first attempt in this direction a high resolution scheme, namely, Flux Limited Kinetic Solver (FLKS) is developed. The method uses Sweby's flux-limited method to discretize the collisionless Boltzmann equation. Subjecting this equation to a moment method strategy results in a high resolution scheme for the Euler equations. At first the scheme is developed for the 1D Euler equations and then it is extended to two dimensions on a rectangular grid through dimensional splitting. Also a rather simple but somewhat approximate way to use FLKS on a triangular unstructured grid is proposed. The following comments can be made about the scheme:

(a) Unlike the KFVS scheme, the FLKS scheme contains antidissipation terms that can be used to regulate dissipation. However, within TVD limits clipping of extrema occurs and resolution of discontinuities is not any better when compared to already existing high-resolution methods. Hence we experiment with relaxing the TVD criteria using a user-dependent parameter. However, this does not reduce the clipping error effectively as the numerical experiments show. As a remedy some extremum-preserving limiter seems to be needed. The specific limiter used fits into any scheme which uses conventional limiting procedure. When such a limiter is used alongside the FLKS scheme, good accuracy in capturing extrema is observed. First, accuracy analysis is performed to show the order of convergence of the scheme using a test problem which has smooth solution. It is observed that the order of accuracy falls between one and two which is expected for a second-order flux-limited scheme. The order of accuracy increases as the CFL number reduces. To validate 1D FLKS several Riemann problems are solved. Two of the Sod type Riemann problems when solved give accuracy characteristic of a high-resolution scheme. The scheme is then applied to a test case proposed by Einfeldt et. al., that produces a very low pressure and density region. Many schemes fail giving negative pressure and density in the region thus violating the so-called positivity property. FLKS does well in this test and preserves positivity. Blast wave problem is a strong shock test case where the present scheme resolves the discontinuities and their interaction zones with better resolution than the well-established second-order HRKFVS scheme. The Shu-Osher shock-entropy wave interaction problem demonstrates improvement in extrema capturing when 1D FLKS scheme is used in conjunction with extremum-preserving limiter. It is demonstrated that compared with the second-order HRKFVS scheme, FLKS gives better resolution at shocks, contacts, corners of expansion fans and other high-gradient

regions. Thus we conclude that 1D FLKS is a robust and accurate scheme in that it does not fail in difficult situations and offers fine resolution in high-gradient regions.

(b) After having validated the 1D FLKS it is then extended to two dimensions through dimensional splitting. It is shown that, like the 1D scheme, here too the TVD criterion may be relaxed when desired using a user-dependent parameter. Robustness of the 2D scheme is demonstrated by computing problems like Woodward and Colella's forward facing step problem and double Mach reflection problem. Again compared with the well-known kinetic scheme KFVS, the present scheme performs better. As expected the crispness of the discontinuities increases when more compressive limiters are used. The sonic line just above the corner of the step (in the forward facing step problem) is a critical area where several schemes give nonphysical expansion shocks; however, FLKS does not display any such nonphysical behaviour. The compatibility of 2D FLKS with the extremum-preserving limiter is demonstrated through the double Mach reflection problem, as use of this limiter seems to capture with better resolution the corner of the curling up configuration of the primary slip lines when hit by secondary reflected shock. The 2D FLKS scheme is then employed to compute some 2D Riemann problems that are frequently used to verify the ability of schemes to capture multi-dimensional flow features. Here too, the present scheme demonstrates its ability to compute these difficult problems with reasonable accuracy. The adaptability of the 2D FLKS scheme for unstructured grid is then explored by proposing a new approximate strategy that can be used on unstructured triangular grids. On a well-behaved grid where the triangles are not much skewed, the accuracy appears to be reasonably good. This is demonstrated through some difficult test cases.

FLKS scheme is then suitably modified to adapt it to solve the Navier-Stokes equations. A common strategy used in computational gas dynamics to compute viscous flows is to use a scheme for the Euler equations for the inviscid part of the equations and then discretize the viscous fluxes through "central differencing". When a similar strategy is used alongside FLKS, the scheme seemed to face a debilitating problem of having to use an extremely small time step for good accuracy. To redeem this problem we go back to the kinetic root of the scheme — the Boltzmann equation. Here, instead of the collisionless Boltzmann equation we use the Boltzmann equation with the collision term approximated by the Bhatnagar-Gross-Krook (BGK) collision model. A Chapman-Enskog procedure followed by a moment method strategy is used similar to the inviscid case to obtain a kinetic scheme for the Navier-Stokes equations. This scheme may be termed as Flux Limited Kinetic Viscous Scheme (FLKVS). Some viscous test cases are solved

and it is demonstrated how the Chapman-Enskog procedure-based scheme overcomes the time-step restriction imposed by the collisionless Boltzmann equation-based scheme. This scheme thus constitutes an effective solution method for computing viscous compressible flows.

One observation we have made during the course of this work is that, like other well-established kinetic schemes in the literature, the FLKS and FLKVS schemes are not highly time-efficient. An attempt to explore whether a flux-corrected method has some timewise advantage over FLKS (which is a flux-limited method) resulted in a new scheme, which we call the Kinetic Flux Corrected (KFC) scheme, which is a high resolution scheme for the Euler equations. Using the approximate strategy used earlier the scheme is extended to unstructured triangular grids. It is seen that the scheme gives far better timewise efficiency compared with FLKS, as the numerical flux expressions, which contain no error function terms, are considerably simpler than those for the FLKS. The flux-correction provides sufficient nonlinear stability to avoid any significant spurious oscillations. For strong shock cases a small amount of explicit second-order artificial viscosity seems to work well for suppressing spurious wiggles. The simplicity of the scheme makes it very cost effective compared with the FLKS and HRKFVS schemes.

The preceding description shows that we have largely achieved most of the objectives we set before us at the beginning. Thus we believe that the work has been brought to a logical conclusion.

8.2 Future Recommendations

Finally, in course of what follows we describe some possible scopes for future work as the present study opens up some interesting possibilities for further investigations.

1. The possibility of the FLKS scheme being made arbitrary-order accurate using ADER methodology [5] can be explored.

2. In this new ADER based FLKS, BGK approximation of the collision term can be incorporated to obtain a sophisticated Navier-Stokes solver.

3. The formulation of FLKS and KFC schemes on unstructured grids can be improved using some recent interpolation techniques in the literature.

4. The two user-adjustable parameters in the KFC scheme can be made flow data dependent using some nonlinear stability analysis to improve the robustness of the scheme.

5. Being Boltzmann equation based schemes, the applicability of these scheme can possibly be extended to rarefied gas flow regime as well.

6. The 2D schemes can further be extended to 3D flow situations.

Appendix A

Conserved Variable Vector and Flux Vector of the 1D Euler Equations as Moments of the Maxwellian Distribution

The equation (2.2.5a) for the conserved variable vector and equation (2.2.5b) for flux vector can be written as

$$\mathbf{U} = \begin{bmatrix} U^{(1)} \\ U^{(2)} \\ U^{(3)} \end{bmatrix} = \int_0^\infty dI \int_{-\infty}^\infty dv_1 \boldsymbol{\Psi} F \quad \text{and} \quad \mathbf{FX} = \begin{bmatrix} FX^{(1)} \\ FX^{(2)} \\ FX^{(3)} \end{bmatrix} = \int_0^\infty dI \int_{-\infty}^\infty dv_1 \boldsymbol{\Psi} v_1 F, \tag{A.1}$$

respectively, where

$$\boldsymbol{\Psi} = \begin{bmatrix} 1 \\ v_1 \\ I + \frac{v_1^2}{2} \end{bmatrix} \quad \text{and} \quad F = \frac{\rho}{I_0}\sqrt{\frac{\beta}{\pi}} \exp\left\{-\beta(v_1 - u)^2 - \frac{I}{I_0}\right\}. \tag{A.2}$$

Here the distribution function F is a function of space x, time t, molecular velocity v_1 and the internal energy variable I. The dependence of F on x and t comes via the presence of the flow variables ρ, I_0, β and u, which are functions of x and t. We use the following known integrals in

the evaluation of the integrals in equation (A.1).

$$\int_0^\infty \exp\left\{-\frac{I}{I_0}\right\} dI = I_0 \tag{A.3a}$$

$$\int_0^\infty I \exp\left\{-\frac{I}{I_0}\right\} dI = I_0^2 \tag{A.3b}$$

and

$$\int_{-\infty}^\infty \exp\left\{-\beta(v_1-u)^2\right\} dv_1 = \sqrt{\frac{\pi}{\beta}} \tag{A.4a}$$

$$\int_{-\infty}^\infty v_1 \exp\left\{-\beta(v_1-u)^2\right\} dv_1 = u\sqrt{\frac{\pi}{\beta}} \tag{A.4b}$$

$$\int_{-\infty}^\infty v_1^2 \exp\left\{-\beta(v_1-u)^2\right\} dv_1 = \left(u^2+\frac{1}{2\beta}\right)\sqrt{\frac{\pi}{\beta}} \tag{A.4c}$$

$$\int_{-\infty}^\infty v_1^3 \exp\left\{-\beta(v_1-u)^2\right\} dv_1 = \left(u^3+\frac{3u}{2\beta}\right)\sqrt{\frac{\pi}{\beta}} \tag{A.4d}$$

where

$$I_0 = \frac{3-\gamma}{2(\gamma-1)}RT \tag{A.5a}$$

$$\beta = \frac{1}{2RT} \tag{A.5b}$$

and we have the property relations

$$p = \rho RT \tag{A.6a}$$

$$e = \frac{p}{\rho(\gamma-1)} + \frac{u^2}{2}. \tag{A.6b}$$

Now $U^{(1)}$ in equation (A.1) is given by

$$\begin{aligned}
U^{(1)} &= \int_0^\infty dI \int_{-\infty}^\infty dv_1 F \\
&= \int_0^\infty dI \int_{-\infty}^\infty dv_1 \left[\frac{\rho}{I_0}\sqrt{\frac{\beta}{\pi}} \exp\left\{-\beta(v_1-u)^2 - \frac{I}{I_0}\right\}\right] \\
&= \frac{\rho}{I_0}\sqrt{\frac{\beta}{\pi}} \left[\int_0^\infty \exp\left(-\frac{I}{I_0}\right) dI\right] \left[\int_{-\infty}^\infty \exp\left\{-\beta(v_1-u)^2\right\} dv_1\right] \\
&= \frac{\rho}{I_0}\sqrt{\frac{\beta}{\pi}} I_0 \sqrt{\frac{\pi}{\beta}} \\
&= \rho.
\end{aligned}$$

$$
\begin{aligned}
U^{(2)} &= \int_0^\infty dI \int_{-\infty}^\infty dv_1 (v_1 F) \\
&= \int_0^\infty dI \int_{-\infty}^\infty dv_1 \left[v_1 \frac{\rho}{I_0} \sqrt{\frac{\beta}{\pi}} \exp\left\{ -\beta (v_1 - u)^2 - \frac{I}{I_0} \right\} \right] \\
&= \frac{\rho}{I_0} \sqrt{\frac{\beta}{\pi}} \left[\int_0^\infty \exp\left(-\frac{I}{I_0} \right) dI \right] \left[\int_{-\infty}^\infty v_1 \exp\left\{ -\beta (v_1 - u)^2 \right\} dv_1 \right] \\
&= \frac{\rho}{I_0} \sqrt{\frac{\beta}{\pi}} I_0 u \sqrt{\frac{\pi}{\beta}} \\
&= \rho u.
\end{aligned}
$$

$$
\begin{aligned}
U^{(3)} &= \int_0^\infty dI \int_{-\infty}^\infty dv_1 \left(I + \frac{v_1^2}{2} \right) F \\
&= \int_0^\infty dI \int_{-\infty}^\infty dv_1 \left[\left(I + \frac{v_1^2}{2} \right) \frac{\rho}{I_0} \sqrt{\frac{\beta}{\pi}} \exp\left\{ -\beta (v_1 - u)^2 - \frac{I}{I_0} \right\} \right] \\
&= \frac{\rho}{I_0} \sqrt{\frac{\beta}{\pi}} \left[\int_0^\infty I \exp\left(-\frac{I}{I_0} \right) dI \right] \left[\int_{-\infty}^\infty \exp\left\{ -\beta (v_1 - u)^2 \right\} dv_1 \right] \\
&+ \frac{\rho}{I_0} \sqrt{\frac{\beta}{\pi}} \left[\int_0^\infty \exp\left(-\frac{I}{I_0} \right) dI \right] \left[\int_{-\infty}^\infty \frac{v_1^2}{2} \exp\left\{ -\beta (v_1 - u)^2 \right\} dv_1 \right] \\
&= \frac{\rho}{I_0} \sqrt{\frac{\beta}{\pi}} \left[I_0^2 \sqrt{\frac{\pi}{\beta}} + I_0 \left(u^2 + \frac{1}{2\beta} \right) \frac{1}{2} \sqrt{\frac{\pi}{\beta}} \right] \\
&= \rho \left[I_0 + \frac{1}{2} \left(u^2 + \frac{1}{2\beta} \right) \right] \\
&= \rho e.
\end{aligned}
$$

Since the expression for the flux $FX^{(1)}$ in equation (A.1) is

$$
FX^{(1)} = \int_0^\infty dI \int_{-\infty}^\infty dv_1 (v_1 F)
$$

which is the same expression as that for $U^{(2)}$, we get

$$
FX^{(1)} = \rho u.
$$

Now $FX^{(2)}$ in equation (A.1) is

$$\begin{aligned}
FX^{(2)} &= \int_0^\infty dI \int_{-\infty}^\infty dv_1 (v_1^2 F) \\
&= \int_0^\infty dI \int_{-\infty}^\infty dv_1 \left[v_1^2 \frac{\rho}{I_0} \sqrt{\frac{\beta}{\pi}} \exp\left\{ -\beta(v_1 - u)^2 - \frac{I}{I_0} \right\} \right] \\
&= \frac{\rho}{I_0} \sqrt{\frac{\beta}{\pi}} \left[\int_0^\infty \exp\left(-\frac{I}{I_0} \right) dI \right] \left[\int_{-\infty}^\infty v_1^2 \exp\left\{ -\beta(v_1 - u)^2 \right\} dv_1 \right] \\
&= \frac{\rho}{I_0} \sqrt{\frac{\beta}{\pi}} I_0 \left(u^2 + \frac{1}{2\beta} \right) \sqrt{\frac{\pi}{\beta}} \\
&= \rho u^2 + \frac{\rho}{2\beta} \\
&= p + \rho u^2
\end{aligned}$$

and

$$\begin{aligned}
FX^{(3)} &= \int_0^\infty dI \int_{-\infty}^\infty dv_1 \left(I + \frac{v_1^2}{2} \right) v_1 F \\
&= \int_0^\infty dI \int_{-\infty}^\infty dv_1 \left[\left(I + \frac{v_1^2}{2} \right) v_1 \frac{\rho}{I_0} \sqrt{\frac{\beta}{\pi}} \exp\left\{ -\beta(v_1 - u)^2 - \frac{I}{I_0} \right\} \right] \\
&= \frac{\rho}{I_0} \sqrt{\frac{\beta}{\pi}} \left[\int_0^\infty I \exp\left(-\frac{I}{I_0} \right) dI \right] \left[\int_{-\infty}^\infty v_1 \exp\left\{ -\beta(v_1 - u)^2 \right\} dv_1 \right] \\
&+ \frac{\rho}{I_0} \sqrt{\frac{\beta}{\pi}} \left[\int_0^\infty \exp\left(-\frac{I}{I_0} \right) dI \right] \left[\int_{-\infty}^\infty \frac{v_1^3}{2} \exp\left\{ -\beta(v_1 - u)^2 \right\} dv_1 \right] \\
&= \frac{\rho}{I_0} \sqrt{\frac{\beta}{\pi}} \left[I_0^2 u \sqrt{\frac{\pi}{\beta}} + I_0 \frac{1}{2} \left(u^3 + \frac{3u}{2\beta} \right) \sqrt{\frac{\pi}{\beta}} \right] \\
&= \rho u \left[I_0 + \frac{u^2}{2} + \frac{3}{4\beta} \right] \\
&= (p + \rho e) u.
\end{aligned}$$

Appendix B

The Derivation of Split Viscous Fluxes

We use Chou and Baganoff [72] type splitting where the viscous fluxes are split according to the sign of molecular velocities. The expressions for viscous fluxes from equations (5.3.9a) and (5.3.9b) are repeated here.

$$\mathbf{FX}_v = \tau \int_0^\infty \int_{-\infty}^\infty \int_{-\infty}^\infty \boldsymbol{\Psi} v_1 (DF) dv_1 dv_2 dI \tag{B.1a}$$

$$\mathbf{FY}_v = \tau \int_0^\infty \int_{-\infty}^\infty \int_{-\infty}^\infty \boldsymbol{\Psi} v_2 (DF) dv_1 dv_2 dI \tag{B.1b}$$

Now we can write

$$\begin{aligned}\mathbf{FX}_v &= \mathbf{FX}_v^+ + \mathbf{FX}_v^- \\ &= \tau \int_0^\infty \int_{-\infty}^\infty \int_0^\infty \boldsymbol{\Psi} v_1 (DF) dv_1 dv_2 dI + \tau \int_0^\infty \int_{-\infty}^\infty \int_{-\infty}^0 \boldsymbol{\Psi} v_1 (DF) dv_1 dv_2 dI \end{aligned} \tag{B.2a}$$

$$\begin{aligned}\mathbf{FY}_v &= \mathbf{FY}_v^+ + \mathbf{FY}_v^- \\ &= \tau \int_0^\infty \int_0^\infty \int_{-\infty}^\infty \boldsymbol{\Psi} v_2 (DF) dv_1 dv_2 dI + \tau \int_0^\infty \int_{-\infty}^0 \int_{-\infty}^\infty \boldsymbol{\Psi} v_2 (DF) dv_1 dv_2 dI \end{aligned} \tag{B.2b}$$

These split fluxes are evaluated using MATHEMATICA to arrive at the following expressions:

$$\mathbf{FX}_v^{\pm} = \tau p \begin{bmatrix} 0 \\ (3-\gamma)\frac{\partial u}{\partial x} - (\gamma-1)\frac{\partial v}{\partial y} \\ \frac{\partial u}{\partial y} + \frac{\partial v}{\partial x} \\ \left\{(3-\gamma)\frac{\partial u}{\partial x} - (\gamma-1)\frac{\partial v}{\partial y}\right\} u + \left(\frac{\partial u}{\partial y} + \frac{\partial v}{\partial x}\right) v + \frac{\gamma R}{\gamma-1}\frac{\partial T}{\partial x} \end{bmatrix} X_1^{\pm}$$
$$\pm \tau p \begin{bmatrix} \beta\left\{(3-\gamma)\frac{\partial u}{\partial x} - (\gamma-1)\frac{\partial v}{\partial y} - \frac{u}{T}\frac{\partial T}{\partial x}\right\} \\ \frac{1}{T}\frac{\partial T}{\partial x} \\ \beta v\left\{(3-\gamma)\frac{\partial u}{\partial x} - (\gamma-1)\frac{\partial v}{\partial y} - \frac{u}{T}\frac{\partial T}{\partial x}\right\} + \frac{1}{2T}\frac{\partial T}{\partial y} \\ \left\{\frac{3\gamma-1}{4(\gamma-1)} + \frac{v^2\beta}{2}\right\}\left\{(3-\gamma)\frac{\partial u}{\partial x} - (\gamma-1)\frac{\partial v}{\partial y}\right\} - \left\{\frac{3-\gamma}{4(\gamma-1)} + \frac{v^2\beta}{2}\right\}\frac{u}{T}\frac{\partial T}{\partial x} + \frac{v}{2T}\frac{\partial T}{\partial y} \end{bmatrix} Y_1 \tag{B.3a}$$

$$\mathbf{FY}_v^{\pm} = \tau p \begin{bmatrix} 0 \\ \frac{\partial u}{\partial y} + \frac{\partial v}{\partial x} \\ (3-\gamma)\frac{\partial v}{\partial y} - (\gamma-1)\frac{\partial u}{\partial x} \\ \left\{(3-\gamma)\frac{\partial v}{\partial y} - (\gamma-1)\frac{\partial u}{\partial x}\right\} v + \left(\frac{\partial u}{\partial y} + \frac{\partial v}{\partial x}\right) u + \frac{\gamma R}{\gamma-1}\frac{\partial T}{\partial y} \end{bmatrix} X_2^{\pm}$$
$$\pm \tau p \begin{bmatrix} \beta\left\{(3-\gamma)\frac{\partial v}{\partial y} - (\gamma-1)\frac{\partial u}{\partial x} - \frac{v}{T}\frac{\partial T}{\partial y}\right\} \\ \beta u\left\{(3-\gamma)\frac{\partial v}{\partial y} - (\gamma-1)\frac{\partial u}{\partial x} - \frac{v}{T}\frac{\partial T}{\partial y}\right\} + \frac{1}{2T}\frac{\partial T}{\partial x} \\ \frac{1}{T}\frac{\partial T}{\partial y} \\ \left\{\frac{3\gamma-1}{4(\gamma-1)} + \frac{u^2\beta}{2}\right\}\left\{(3-\gamma)\frac{\partial v}{\partial y} - (\gamma-1)\frac{\partial u}{\partial x}\right\} - \left\{\frac{3-\gamma}{4(\gamma-1)} + \frac{u^2\beta}{2}\right\}\frac{v}{T}\frac{\partial T}{\partial y} + \frac{u}{2T}\frac{\partial T}{\partial x} \end{bmatrix} Y_2 \tag{B.3b}$$

where $X_1^{\pm}, X_2^{\pm}, Y_1$ and Y_2 are given by equation (4.1.5).

The derivatives appearing in (B.3) like $\frac{\partial u}{\partial x}, \frac{\partial v}{\partial y}$, etc., are evaluated by second order central differencing.

References

[1] A. Harten, P. D. Lax, B. van Leer, On upstream differencing and Godunov-type schemes for hyperbolic conservation laws, SIAM Review 25 (1) (1983) 35–61.

[2] W. G. Vincenti, C. H. Kruger, Introduction to physical gas dynamics, New York, Wiley, 1965.

[3] S. Chapman, T. G. Cowling, The mathematical theory of non-uniform gases: an account of the kinetic theory of viscosity, thermal conduction and diffusion in gases, Cambridge university press, 1970.

[4] P. L. Bhatnagar, E. P. Gross, M. Krook, A model for collision processes in gases. I. Small amplitude processes in charged and neutral one-component systems, Physical review 94 (3) (1954) 511.

[5] E. F. Toro, Riemann Solvers and Numerical Methods for Fluid Dynamics: A Practical Introduction, 3rd Edition, Springer, 2009.

[6] K. Xu, Gas-kinetic schemes for unsteady compressible flow simulations, Lecture series-von Karman Institute for fluid dynamics 3 (1998) C1–C202.

[7] K. H. Prendergast, K. Xu, Numerical hydrodynamics from gas-kinetic theory, Journal of Computational Physics 109 (1) (1993) 53–66.

[8] K. Xu, J.-C. Huang, A unified gas-kinetic scheme for continuum and rarefied flows, Journal of Computational Physics 229 (2010) 7747–7764.

[9] P. D. Lax, Weak solutions of nonlinear hyperbolic equations and their numerical computation, Communications on pure and applied mathematics 7 (1) (1954) 159–193.

[10] P. Lax, B. Wendroff, Systems of conservation laws, Communications on Pure and Applied mathematics 13 (2) (1960) 217–237.

[11] R. MacCormack, The effect of viscosity in hypervelocity impact cratering, AIAA Paper, 1969.

[12] S. K. Godunov, A difference scheme for numerical solution of discontinuous solution of hydrodynamic equations, Math. Sbornik 47 (1959) 271–306.

[13] A. Harten, G. Zwas, Self-adjusting hybrid schemes for shock computations, Journal of Computational Physics 9 (3) (1972) 568–583.

[14] B. Van Leer, Towards the ultimate conservative difference scheme. I. The quest of monotonicity, in: Proceedings of the Third International Conference on Numerical Methods in Fluid Mechanics, Springer, 1973, pp. 163–168.

[15] B. Van Leer, Towards the ultimate conservative difference scheme. II. Monotonicity and conservation combined in a second-order scheme, Journal of Computational Physics 14 (4) (1974) 361–370.

[16] J. E. Fromm, A method for reducing dispersion in convective difference schemes, Journal of Computational Physics 3 (2) (1968) 176–189.

[17] B. Van Leer, Towards the ultimate conservative difference scheme. III. Upstream-centered finite-difference schemes for ideal compressible flow, Journal of Computational Physics 23 (3) (1977) 263–275.

[18] B. Van Leer, Towards the ultimate conservative difference scheme. IV. A new approach to numerical convection, Journal of Computational Physics 23 (3) (1977) 276–299.

[19] B. Van Leer, Towards the ultimate conservative difference scheme. V. A second-order sequel to Godunov's method, Journal of Computational Physics 32 (1) (1979) 101–136.

[20] A. Harten, The artificial compression method for computation of shocks and contact discontinuities. III. Self-adjusting hybrid schemes, Mathematics of Computation 32 (142) (1978) 363–389.

[21] J. L. Steger, R. Warming, Flux vector splitting of the inviscid gasdynamic equations with application to finite-difference methods, Journal of Computational Physics 40 (2) (1981) 263–293.

[22] P. L. Roe, Approximate Riemann solvers, parameter vectors, and difference schemes, Journal of Computational Physics 43 (2) (1981) 357–372.

[23] B. van Leer, Flux-vector splitting for the Euler equations, in: Eighth International Conference on Numerical Methods in Fluid Dynamics, Springer, 1982, pp. 507–512.

[24] A. Harten, High resolution schemes for hyperbolic conservation laws, Journal of Computational Physics 49 (3) (1983) 357–393.

[25] S. Osher, S. Chakravarthy, High resolution schemes and the entropy condition, SIAM Journal on Numerical Analysis 21 (5) (1984) 955–984.

[26] P. K. Sweby, High resolution schemes using flux limiters for hyperbolic conservation laws, SIAM J. Numer. Anal. 21 (5) (1984) 995–1011.

[27] P. L. Roe, Some contributions to the modelling of discontinuous flows, Proceedings of the 1983 AMS-SIAM Summer Seminar on Large Scale Computing in Fluid Mech. 22 (1985) 163–193.

[28] P. Colella, A direct Eulerian MUSCL scheme for gas dynamics, SIAM Journal on Scientific and Statistical Computing 6 (1) (1985) 104–117.

[29] H. Nessyahu, E. Tadmor, Non-oscillatory central differencing for hyperbolic conservation laws, Journal of Computational Physics 87 (2) (1990) 408–463.

[30] M.-S. Liou, C. J. Steffen Jr, A new flux splitting scheme, Journal of Computational Physics 107 (1) (1993) 23–39.

[31] V. Venkatakrishnan, Convergence to steady state solutions of the Euler equations on unstructured grids with limiters, Journal of Computational Physics 118 (1) (1995) 120–130.

[32] G. Billet, O. Louedin, Adaptive limiters for improving the accuracy of the MUSCL approach for unsteady flows, Journal of Computational Physics 170 (1) (2001) 161–183.

[33] M. Darwish, F. Moukalled, TVD schemes for unstructured grids, International Journal of heat and mass transfer 46 (4) (2003) 599–611.

[34] B. Parent, Positivity-preserving high-resolution schemes for systems of conservation laws, Journal of Computational Physics 231 (1) (2012) 173–189.

[35] D. Pullin, Direct simulation methods for compressible inviscid ideal-gas flow, Journal of Computational Physics 34 (2) (1980) 231–244.

[36] R. D. Reitz, One-dimensional compressible gas dynamics calculations using the boltzmann equation, Journal of Computational Physics 42 (1) (1981) 108–123.

[37] S. M. Deshpande, Kinetic theory based new upwind methods for inviscid compressible flows, AIAA Paper 86-0275.

[38] J. C. Mandal, S. M. Deshpande, Kinetic flux vector splitting for Euler equations, Computers & Fluids 23 (2) (1994) 447–478.

[39] S. M. Deshpande, A second order accurate kinetic theory based method for inviscid compressible flows, NASA Technical Paper 2613, NASA Langley Research Centre, Hampton, Virginia, 1986.

[40] A. K. Ghosh, J. S. Mathur, S. M. Deshpande, q-KFVS scheme-a new higher order kinetic method for euler equations, In: Proceedings of 16th International Conference on Numerical Methods in Fluid Dynamics, Lecture Notes in physics 515, 1998.

[41] V. Ramesh, S. M. Deshpande, Unsteady flow computations for flow past multiple moving boundaries using LSKUM, Computers & Fluids 36 (10) (2007) 1592–1608.

[42] K. Xu, K. H. Prendergast, Numerical Navier-Stokes solutions from gas kinetic theory, Journal of Computational Physics 114 (1) (1994) 9–17.

[43] K. Xu, A gas-kinetic BGK scheme for the Navier–Stokes equations and its connection with artificial dissipation and Godunov method, Journal of Computational Physics 171 (1) (2001) 289–335.

[44] G. Ni, S. Jiang, K. Xu, Efficient kinetic schemes for steady and unsteady flow simulations on unstructured meshes, Journal of Computational Physics 227 (6) (2008) 3015–3031.

[45] S. M. Deshpande, N. Balakrishnan, S. V. R. Rao, PVU and wave-particle splitting schemes for Euler equations of gas dynamics, Sadhana 19 (6) (1994) 1027–1054.

[46] L. Tang, Progress in gas-kinetic upwind schemes for the solution of Euler/Navier–Stokes equations–I: Overview, Computers & Fluids 56 (2012) 39–48.

[47] N. Anil, N. K. S. Rajan, S. M. Deshpande, Modified kinetic flux vector splitting (m-KFVS) method for compressible flows, Computers & Fluids 48 (1) (2011) 137–149.

[48] C. Praveen, S. Deshpande, Kinetic meshless method for compressible flows, International Journal for Numerical Methods in Fluids 55 (11) (2007) 1059–1089.

[49] J. Mathur, N. Weatherill, The simulation of inviscid, compressible flows using an upwind kinetic method on unstructured grids, International Journal for Numerical Methods in Fluids 15 (1) (1992) 59–82.

[50] N. Weatherill, J. Mathur, M. Marchant, An upwind kinetic flux vector splitting method on general mesh topologies, International Journal for Numerical Methods in Engineering 37 (4) (1994) 623–643.

[51] B. Perthame, Second-order Boltzmann schemes for compressible Euler equations in one and two space dimensions, SIAM Journal on Numerical Analysis 29 (1) (1992) 1–19.

[52] P. L. Roe, Characteristic-based schemes for the Euler equations, Ann. Rev. Fluid Mech. 18 (1986) 337–365.

[53] C. B. Laney, Computational Gasdynamics, 1st Edition, Cambridge University Press, 1998.

[54] A. K. Ghosh, J. S. Mathur, S. M. Deshpande, Least squares kinetic upwind method for inviscid compressible flows, AIAA Paper, 1995.

[55] A. Jameson, Analysis and design of numerical schemes for gas dynamics 1, artificial diffusion, upwind biasing, limiters and their effect on multigrid convergence, Int. J. of Comp. Fluid Dyn. 4 (1995) 171–218.

[56] B. Einfeldt, C.-D. Munz, P. L. Roe, B. Sjögreen, On Godunov-type methods near low densities, Journal of Computational Physics 92 (2) (1991) 273–295.

[57] P. Woodward, P. Colella, The numerical simulation of two-dimensional fluid flow with strong shocks, Journal of Computational Physics 54 (1984) 115–173.

[58] A. Harten, S. Osher, Uniformly high-order accurate nonoscillatory schemes. I, SIAM J. Numer. Anal. 24 (2) (1987) 279–309.

[59] A. Harten, B. Engquist, S. Osher, S. R. Chakravarthy, Uniformly high-order accurate essentially non-oscillatory schemes. III, Journal of Computational Physics 131 (1997) 3–47.

[60] X.-D. Liu, S. Osher, T. Chan, Weighted essentially non-oscillatory schemes, Journal of Computational Physics 115 (1994) 200–212.

[61] M. Sekora, P. Colella, Extremum-preserving limiters for MUSCL and PPM, arXiv preprint, arXiv:0903.4200, 2009.

[62] P. Colella, M. D. Sekora, A limiter for PPM that preserves accuracy at smooth extrema, Journal of Computational Physics 227 (2008) 7069–7076.

[63] R. J. Leveque, Finite Volume Methods for Hyperbolic Problems, 1st Edition, Cambridge University Press, 2002.

[64] K. Arun, M. Lukáčová-Medvidová, P. Prasad, S. R. Rao, A second order accurate kinetic relaxation scheme for inviscid compressible flows, in: Recent Developments in the Numerics of Nonlinear Hyperbolic Conservation Laws, Springer, 2013, pp. 1–24.

[65] A. Suresh, H. Huynh, Accurate monotonicity-preserving schemes with Runge–Kutta time stepping, Journal of Computational Physics 136 (1) (1997) 83–99.

[66] D. S. Balsara, C.-W. Shu, Monotonicity preserving weighted essentially non-oscillatory schemes with increasingly high order of accuracy, Journal of Computational Physics 160 (2) (2000) 405–452.

[67] G. A. Sod, A survey of several finite difference methods for systems of nonlinear hyperbolic conservation laws, Journal of Computational Physics 27 (1978) 1–31.

[68] C.-W. Shu, S. Osher, Efficient implementation of essentially non-oscillatory shock-capturing schemes, II, Journal of Computational Physics 83 (1989) 32–78.

[69] D. S. Balsara, Multidimensional HLLE Riemann solver: Application to Euler and magnetohydrodynamic flows, Journal of Computational Physics 229 (2010) 1970–1993.

[70] J. C. Mandal, V. Sharma, A genuinely multidimensional convective pressure flux split Riemann solver for Euler equations, Journal of Computational Physics 297 (2015) 669–688.

[71] M. Brio, A. R. Zakharian, G. M. Webb, Two-dimensional Riemann solver for Euler equations of gas dynamics, Journal of Computational Physics 167 (2001) 177–195.

[72] S.-Y. Chou, D. Baganoff, Kinetic flux–vector splitting for the Navier–Stokes equations, Journal of Computational Physics 130 (2) (1997) 217–230.

[73] F. Denner, B. G. van Wachem, TVD differencing on three-dimensional unstructured meshes with monotonicity-preserving correction of mesh skewness, Journal of Computational Physics 298 (2015) 466–479.

[74] D. J. Mavriplis, A. Jameson, L. Martinelli, Multigrid solution of the Navier-Stokes equations on triangular meshes, 27th Aerospace Science Meeting, Reno, NV, Paper AIAA 89-0120, 1989.

[75] D. S. Balsara, M. Dumbser, R. Abgrall, Multidimensional HLLC Riemann solver for unstructured meshes with application to Euler and MHD flows, Journal of Computational Physics 261 (2014) 172–208.

[76] J. P. Boris, D. L. Book, Flux-corrected transport I. SHASTA, a fluid transport algorithm that works, Journal of Computational Physics 11 (1973) 38–69.

List of Publications

Papers (Published)

- Kumar R, Dass AK. A new flux-limiting approach–based kinetic scheme for the Euler equations of gas dynamics. Int J Numer Meth Fluids. 2019;1–35.

Papers (In Preparation)

- Raushan Kumar and Anoop K. Dass, A New Flux-Limiting Approach Based Kinetic Scheme for the Navier-Stokes Equations of Gas Dynamics
- Raushan Kumar and Anoop K. Dass, A Flux-Corrected Kinetic Scheme for the Euler Equations of Gas Dynamics

Conferences

- Raushan Kumar and Anoop K. Dass, A New Second Order Accurate Kinetic Theory Based Scheme for Euler Equations, 5^{th} International and 41^{st} National Conference on Fluid Mechanics and Fluid Power, IIT Kanpur, December 12-14, 2014.
- Raushan Kumar and Anoop K. Dass, A Kinetic-Theory-Based Boltzmann Level Flux-Limited Numerical Scheme for 1-D Euler Equations of Gas Dynamics, XXVII IUPAP Conference on Computational Physics, IIT Guwahati, December 2-5, 2015.
- Raushan Kumar and Anoop K. Dass, A New Kinetic-Theory-Based Flux-Limited Numerical Scheme for 1-D Euler Equations of Gas Dynamics, Conference on Computational PDE, TIFR Centre for Applicable Mathematics, Bangalore, December 21-23, 2015.
- Raushan Kumar and Anoop K. Dass, A Kinetic-Theory-Based Boltzmann Level Flux-Limited Numerical Scheme for 1-D Euler Equations of Gas Dynamics, Research Conclave, IIT Guwahati, March 17-20, 2016.
- Raushan Kumar and Anoop K. Dass, A New Kinetic Flux-Corrected Scheme for 1D Euler Equations of Gasdynamics, 6^{th} International and 43^{st} National Conference on Fluid

Mechanics and Fluid Power (FMFP), MNNITA, Allahabad, U.P., India, December 15-17, 2016.

- Raushan Kumar and Anoop K. Dass, A New Kinetic-Theory-Based Scheme for the 2D Euler and Navier-Stokes Equations of Gas Dynamics, Research Conclave, IIT Guwahati, March 08-11, 2018.

- Raushan Kumar and Anoop K. Dass, A New High-Resolution Kinetic Flux-Corrected Scheme on Unstructured Grids for 2D Euler Equations of Gas Dynamics, 7^{th} International and 45^{th} National Conference on Fluid Mechanics and Fluid Power (FMFP), IIT Bombay, Mumbai, India, December 10-12, 2018.